# Information Processing: Thermodynamics of Computations and Network Inference

**A DISSERTATION**
**SUBMITTED TO THE FACULTY OF THE GRADUATE SCHOOL**
**OF THE UNIVERSITY OF MINNESOTA**
**BY**

**Saurav Talukdar**

**IN PARTIAL FULFILLMENT OF THE REQUIREMENTS**
**FOR THE DEGREE OF**
**DOCTOR OF PHILOSOPHY**

**Prof. Murti V. Salapaka**

**December, 2018**

# Acknowledgements

I would like to thank my adviser Prof. Murti V. Salapaka for his support through this journey. His guidance and mentoring helped me fulfill my aspirations in graduate school. He made sure every resource that I needed to accomplish my research goals is always available to me. Apart from gaining technical skills, I learned the art of conducting scientific research from him. Through my interactions with him I learned to see every directionless moment as an opportunity to learn and explore.

My teachers at my alma mater IIT Bombay, particularly, Prof. Sachin C. Patwardhan and Prof. Salil S. Kulkarni were very inspirational advisers and supportive of my decision to pursue research beyond my undergraduate studies. These interactions helped me focus on control systems as my broader area of interest in graduate school.

I am highly indebted to Dr. Deepjyoti Deka, Scientist at the Los Alamos National Laboratory(LANL) for his time and efforts in shaping the structure learning aspect of this dissertation. I have known Deep as a neighbor (in India), as a high school senior and finally a researcher at LANL. I never imagined that two kids from the same neighborhood in India would end up having overlapping research interests. Through my interactions with Deep, I got opportunities to present my work at the winter schools organized by Dr. Misha Chertkov and his team at LANL. I am thankful to Dr. Chertkov for hosting me as a summer student at the Center for Nonlinear Science in LANL. The summer in the hilly town of Los Alamos was a memorable one and probably my most enjoyable summer in the US so far.

I am forever grateful to fellow students in graduate school who have made this journey a fun filled experience. Dr. Shreyas Bhaban and Dr. James Melbourne were kind to be always available to discuss and bear my excitement. I couldn't have asked for a better team. Through these interactions, I got the opportunity to contribute in disciplines like

bio-physics and information theory; domains where I do not possess technical expertise. I am thankful to my lab mates Harish Doddi and Blake Lundstrom for their efforts in helping me apply my structure learning methods to buildings and power networks respectively. I enjoyed the company of Sivaraman Rajaganapathy, Rachit Shrivastava and Sourav Patel on white board discussions as well as in several restaurants around campus. My friends outside my lab, Biswaranjan Mohanty, Santosh Kumar, Sampreeti Jena, Gaurav Nayak, Narendra Singh, Saurabh Agrawal (apologies to the names I missed) who made my stay in Minneapolis very enjoyable. Santosh, Biswa and Sampreeti made sure I am always well fed. Biswa introduced me to running and motivated me to run my first marathon.

Finally, I am forever indebted to my family for their belief and support. My parents were always happy about the fact that I would become the first doctorate in my family. My wife, Mousumi was very patient with me throughout this journey. I do think there were several sacrifices at her end to let me be immersed in research. I will try and make up for those lost moments in the upcoming future.

# Dedication

I dedicate this thesis to all my teachers

# Abstract

The present times is seeing a surge in computing due to several applications like smart grid, autonomous vehicles, social networks and many more directly touching our lives. A key enabler is the technological advancements in information storage and information processing technologies, for example, data centers, wireless communication, cloud computing, artificial intelligence to name a few. A present day iPhone is more powerful than the computer used by NASA in the Apollo mission as well as the 1997 IBM super computer which defeated Grand-master Gary Kasparov. The consequence is that data centers are now projected to consume about 20% of Earth's power by 2030. In the first part of this dissertation, fundamental computation mechanisms and their energy consumption are explored. Erasure or reset of information stored in a single bit memory is studied in detail. In particular, we experimentally demonstrate erasure using almost the minimum possible amount of energy required for the erasure of a bit of information, as dictated by the Landauer's principle. Optical traps are used to achieve this and a detailed modeling of the dynamics in optical traps is discussed first, which is used to develop a Monte Carlo simulation to study physics of information erasure. Finally, we analyze erasure of information using a Gaussian mixture approach and conclude with the trade-off between reliability of information erasure, minimum energy consumption in information erasure and size of the memory bit.

The second part of this dissertation is focused on information processing from diverse sources with the goal of enabling decision making for energy efficiency, safe operation, human comfort and minimize costs in complex physical systems. For example: the concept of smart home uses information about weather, energy state of the grid, usage pattern of the home owner etc to decide on control set points of thermostats or air conditioners or heaters. In such complex systems, it is often not clear which entities influence which other entities and is nearly impossible to develop a first principles model. Here, the focus is on developing algorithms with guarantees for inference of presence or absence of relationships among observed entities in a complex system. The framework of network representation of complex systems of linear dynamical systems with wide sense stationary forcing is used and algorithms which infer the relationships amongst the observed entities using only time series observations without any knowledge of system parameters is developed. The performance of the algorithms is shown on simulation examples from power grid, building thermal dynamics and experimental realization of a wireless network of agents. Finally, extensions of the algorithms in the case of unobserved states and non stationary processes is discussed.

# Contents

# List of Tables

# List of Figures

# Chapter 1

# Introduction

Present day innovations like a smart power grid [5], autonomous vehicles [6], smart buildings [7] and many others involve decision making based on collection and processing of information from several sources. These applications are made possible due to several technological breakthroughs viz., sensing [8], computation and communication [9] , high density storage in data centers [10], cloud/ edge computing [11, 12] to name a few. Seemingly independent activities in our lives are now getting connected together in this era of Internet of Things [13]. The ability to sense and store these type of diverse set of entities of interest at a sharp time resolution (in data centers) and ability to perform computations on the collected information in real time (using the internet and cloud/ edge computing frameworks) are a key enabler in the use of massive volume of information for designing sophisticated schemes for improving energy efficiency, increasing operational safety, lowering operation costs and enhancing human comfort. For example: our office buildings are now transitioning into smart buildings where zonal set points of temperature, humidity and other important variables are decided based on measurements of occupancy, weather, power demand in the grid, energy generation from roof top solar panels, stored energy in batteries to name a few [14]. Recently, Google used AI techniques to design control schemes which reduced the cooling bills of data centers by 40% [15]. Motivated from the technological advancements as discussed above, in this dissertation we explore two fundamental research themes:

- Physics of Computation: It is estimated that computing devices, including personal devices to data centers will consume about 20% of energy globally by 2030 [16]. We explore fundamental mechanisms of energy consumption in computations to understand energy budget of complex algorithms. Ability to store high density of information in a small volume and processing at high speeds for performing desired computations involves significant energy consumption and heat dissipation. Our laptops or phones often heat up and the battery drains faster while executing an intensive task. We explore fundamental computational mechanisms at a single bit level (physical length scale of few $nm$) which are responsible for heat generation and energy consumption in performing computations as well as approaches to minimize them. The problem that we address involves identifying a non trivial fundamental limit on the minimum heat dissipation associated with bit level operations, experimental demonstration of performing computations at the fundamental limit and possible ways of reducing the minimum heat dissipation associated with bit level operations.

- Structure Learning in Networks: Networks are a framework used for representation of complex systems like the power grid [17], buildings [18], brain [19], climate [20] and many others [21]. It helps to identify underlying dependencies, influence pathways or cause-effect mechanisms to explain observed phenomenon. The advent of smart sensors has resulted in high time resolution monitoring of essential variables in several complex systems, which has enabled decision making or inference of important events resulting in improved safety, better operation and comfort. As the underlying physics is sophisticated, in several applications it is difficult to develop network representation of complex systems from first principles. The fundamental problem we address in this regard is: How do we develop a network representation of a complex system using time series data collected by the various sensors monitoring the system?

## 1.1 Physics of Computation

The impact of the phenomenal increase in computational power acquired by human kind is evident from the rapid pace at which it has become indispensable in many aspects of

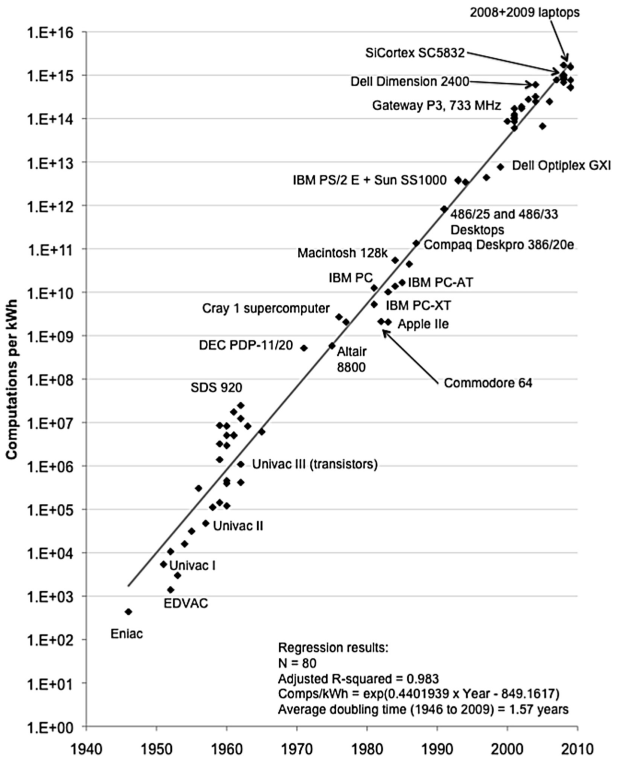

Figure 1.1: The plot descirbes the number of computations that can be performed per KwH over 6 decades; efficiency on an average had doubled every 1.57 years [1].

life. A key to the enormous success and the rapid rates of improvement, which is still continuing, is technology that has enabled doubling the complexity of integrated chips where the number of transistors on a chip has doubled every 1.8 years for the last two decades (known as the Moore's law [22, 23]). The accompanying and more impressive trend is the doubling of energy efficiency of computation (see Figure 1.1) every 1.5 years for the past few decades. The increased efficiency is at the heart of the now ubiquitous use of mobile computational platforms. There is plenty of room before practical devices reach fundamental limits that can stall the growth; in 1985, [24] estimated that a $10^{11}$ orders improvement is possible over then existing computers, only a factor of $40,000$ is harnessed since 1985, which motivates a study of the fundamental limits on the energetics of computation.

The AND and the NOT operations are sufficient to realize logical computations in computers. Apart from these fundamental operations, the erasure or reset operation is important as it is vital for memory management. The erasure operation sets the bit to zero irrespective of its original state. The NOT operation is logically reversible, as it is one-to-one, whereas, the erasure and AND operation is many to one, and is considered logically irreversible. Whether an operation is logically reversible or not has a significant bearing on its energetics. Here, many-to-one operations lead to the 'loss' of information, where, such a loss is accompanied by at least $k_bT \ln 2$ of energy dissipation per bit of information lost, irrespective of the nature of the computation. Groundbreaking work by [25], [26] and [27] established a connection between the seemingly disparate fields of Thermodynamics and Information Theory. Landauer's Principle states that erasing (or reset of) a single bit of information is accompanied by dissipation of at least $k_bT \ln 2$ amount of energy. Landauer argued that erasure of information lowers the entropy of the overall system and thus, is accompanied by an average heat dissipation of at least $k_bT \ln 2$ amount of energy per erased bit. In this dissertation, we will the study the thermodynamics of erasure of a single bit of information from an experimental as well as analytical perspective. It also needs to be remarked that the current computers use approximately $10^{-15}J$ per computation whereas, $k_bT \approx 10^{-21}J$. Thus, even though there is considerable ground to cover for commercial devices; proof of concept experiments have demonstrated only recently that computations with $k_bT$ energetics, approaching the thermodynamic limits on information erasure can be achieved.

The operations of erasure, NOT, AND, can be performed with or without feedback. Here too, measurements if available can render the realization of the operations easier; however, a comparison of the energetics with or without feedback is essential for understanding fundamental limitations. The connections of feedback, computations and measurement with the thermodynamic quantities of work, heat and entropy, have to be understood to analyze the energetics of computations involving feedback actions. This work will form the basis to enable fundamental studies on the thermodynamic aspects of fundamental computation mechanisms as well as bit level measurement and feedback action. The specific research contributions of this dissertation on the theme of physics of computations are summarized below:

- Creation and characterization of single bit memories with energetics at the $k_BT$ scale: Experimental methods for synthesizing single bit memories and ability to perform computations on the realized memory bit is developed. The synthesis aim is coupled with the development of a methodology for measuring energetics in the

$k_BT$ regime with errors quantified.

- Understanding and realizing erasure or reset of information at the fundamental energy limit: Energetics of information erasure will be studied. Erasure of information very close to the fundamental limit of $k_BT \ln 2$ as described by Landauer, is demonstrated experimentally as well as in Monte Carlo simulations.
- Interplay of speed, reliability in energetics of bit erasure: An analytical framework to analyze the interplay between (i) the time to complete erasure of a bit of information, (ii) the reliability of erasure operation and (iii) the energetics of bit erasure is developed.

In Chapter 2, we present an introduction to Optical tweezers and a characterization of a Brownian particle in a double well potential, which forms our basis for performing computations on information stored in a single bit memory. In Chapter 3, we present a description of single bit memory and its connections with a Brownian particle in a double well potential and demonstrate a mechanism for erasing the information stored in the memory bit using an Optical Tweezer. Moreover, the thermodynamic analysis of the erasure process is also discussed. In Chapter 4 we present analytical characterization of erasure of single bit of information.

### 1.1.1 Collaborators

The experimental aspect of the work was done jointly with Shreyas Bhaban, Becton Dickinson (ex University of Minnesota ECE PhD student) who primarily aided me in the experimental stage of research. James Melbourne, Post Doc, University of Minnesota was helpful in developing the analytical framework as well as broadening my viewpoint of the analytical results, particularly, its application in Information Theory.

## 1.2 Structure Learning in Networks

Networks are widely used to represent the functioning of complex physical systems like the power grid [28], brain [19] as well nonphysical systems like social relationships [29], financial systems [30] and many others. In some applications, there is a clear and evident physical network of agents. For example, consider a collection of agents which comprise of a wireless hub that receive and transmit signals according to a communication network topology [31]. In other applications, a physical network is not evident, for example, sensors measuring temperature at various zones in a building, do not admit easy identification of physical links that connect measurements. In either scenario, network models play important role for determining influences and identification of important clusters. The resulting influence pathways can suggest methods to steer the system toward a desired behavior. We note that for applications where an actual physical network of interactions is evident, the network of mutual influences can differ from its physical network, and often provides complimentary information. In many applications it is possible to manipulate the system to help identifying the network. An active approach for identifying the presence of influences between agents may entail removing agents from the network to evaluate their impact on other agents and then infer influence pathways [32]. Such approaches are invasive. In many applications it may not be possible to excite/perturb the system to decipher the influence of one variable on the rest. For instance, in the stock market, it is not possible to set the price of a particular stock to evaluate the impact on the other stocks. Thus, there is a clear need of non invasive approaches to infer the network representation of complex systems [33].

Non-invasive methods of learning the network structure is an active area of research in multiple disciplines including control theory, computer science and statistics to name a few. Here an initial focus utilized modeling activity of agents via random variables; the graphical models approach (see [34],[35], [36], [37]) employed the random variable based abstraction extensively. More recently, structure learning methods have utilized time series measurements of agents' activity modeled as stochastic processes [38], [39]. The approach of using stochastic processes to model time-series is well-suited for scenarios where agents interact dynamically; where the past or present state of an agent can affect the present state of another agent. Such interdependence is particularly apt for modeling high resolution time-series measurements, which is becoming more widespread due the increasing availability of smart sensors with high bandwidth (for example, Phase Measurement Units employed by the power grid [40]) in many domains including Internet of Things.

The focus of this dissertation is on the inference of the presence or absence of influence pathways or interconnections in linear dynamical systems with applications in power grid networks, thermal dynamics of buildings and multi-agent systems. We only utilize time series measurements of the output variables (assumed to be weakly stationary processes) from the complex physical system and do not use any information about system parameters or inputs. Algorithms with provable guarantees under a set of structural or system dynamic constraints are presented for inference of network structure from observations. The specific research contributions of this dissertation on the theme of structure learning in networks are listed below:

- Algorithm for exact network structure learning in a radial network of bi-directed linear dynamical systems using a mixture of ideas in signal processing and probabilistic graphical models is presented.
- Algorithm for exact network structure learning for linear dynamical systems in the presence of loops is discussed. Moreover, regularization methods are developed for improving performance of above algorithms in low number of observations regime.
- Network structure learning with partial network observability for radial bi-directed linear dynamical systems is presented.
- Generalization of the structure learning framework to periodic stochastic processes; a class of non stationary processes with linear dynamics is discussed.

In Chapter 5, we introduce the network topology learning problem in the context of linear bi-directed systems with radial network structure and present an effective algorithm for network inference with applications in power networks. It is then followed by an algorithm for network structure inference of linear dynamical systems with loops along with application in power networks, multi-agent systems undergoing consensus algorithms and building thermal dynamics in Chapter 6. Furthermore, a modification of the algorithms for improving robustness in low number of samples regime using regularizers is also discussed. In Chapter 7, we present a framework for sensor placement and an algorithm for exact network structure inference in radial bi-directed linear dynamical systems with certain nodes being unobserved. Chapters 5, 6 and 7 focus on wide sense stationary time series observations. In Chapter 8, we extend the framework to a class of non stationary time series observations, viz. cyclostationary or periodic stochastic processes. Chapter 9 concludes this dissertation and provides directions for future work.

### 1.2.1 Collaborators

Dr. Deepjyoti Deka from Los Alamos National Laboratory was instrumental in the structure learning aspect of this dissertation. I benefited a lot from my interactions with him and the discussions helped me frame the right problem, particularly in the context of power system applications. Harish Doddi, PhD student in Mechanical Engineering, University of Minnesota, Sandeep Attree, alumni ECE, University of Minnesota and Blake Lundstrom, National Renewable Energy Laboratory helped me in applying the algorithms developed in the context of buildings, wireless networks and power systems respectively. The work on regularization and latent nodes was developed during my stint as a summer student at the Los Alamos National Laboratory in Dr. Michael Chertkov's group.

# Chapter 2

# Physics of Computation: Dynamics of a Brownian Particle in an Optical Trap

## 2.1 INTRODUCTION

New abilities of measuring and manipulating matter at the nanoscale hold the promise of designing and fabricating material, by rational control of matter at the nano/micro scale, with unparalleled specificity. Unlike in macro scale processes, thermal fluctuations play a significant role in guiding and determining the results of processes (such as transport) and shapes the matter at the nano and smaller scales. With advances in nanotechnology, the effects of thermal noise can be measured and thus nano/microscale systems provide a means to unravel the fundamental mechanism at play at smaller scales ([41, 42]).

In this chapter, the focus is on modeling the dynamics of micron sized Brownian particles under the influence of optical traps. While in this thesis we will utilize optical traps for analyzing the physics of performing computations, they are also used extensively used for experimental investigation of intracellular transport [43], polymer characterization [44] and many others. A key step for these diverse set of applications is to obtain models that are realistic, which can be employed with quantitative precision to design desired manipulation strategies.

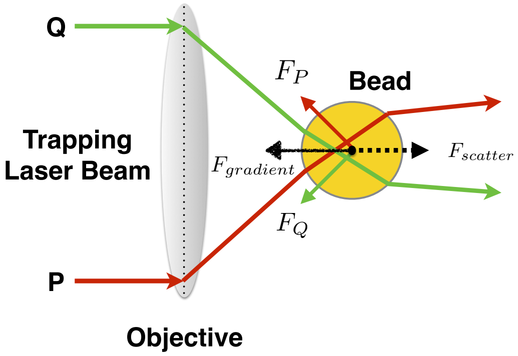

Figure 2.1: Bead in an optical trap

Arthur Ashkin [45] demonstrated that when a laser beam is passed through an objective with appropriately high numerical aperture, the momentum transfer from the reflected and refracted rays onto microscopic particles in the vicinity of the focus generates two kinds of forces on the particle. As is seen in Fig. 2.1, the gradient forces, that result from the Gaussian intensity profile of the laser, balance the destabilizing scattering force of the laser that push the particle away from the focus, creating an equilibruim point. Furthermore, if the particle is dislodged from the equilibruim point, it experiences a restoring force that pulls it back towards the focal point, indicating that it is a stable equilibruim point. This phenomenon of 'trapping' of optical beads is referred to optical trapping, for which Arthur Ashkin was awarded the 2018 Noble Prize in Physics.

A particle in such a stable trap experiences restoring forces that vary linearly with small displacements away from the focus, indicating a harmonic potential in the optical trap. However, the force felt by the particle has a complex relationship with the shape of the particle, the relative refractive index of the particle with respect to its surroundings and on the relative position of the focal spot of the laser beam with respect to the particle center of mass. The force field generated by the optical potentials has to be quantitatively understood over large excursions of the bead positions and thus linear approximation do not suffice. Although the qualitative understanding and underlying principles for such particle behavior are well understood, it is difficult to arrive at a realistic model of this system using first principles, emphasizing a need for experiments to inform models describing such systems. In Section II below, we present a brief description of the optical trapping setup, which is referred to as the optical tweezer.

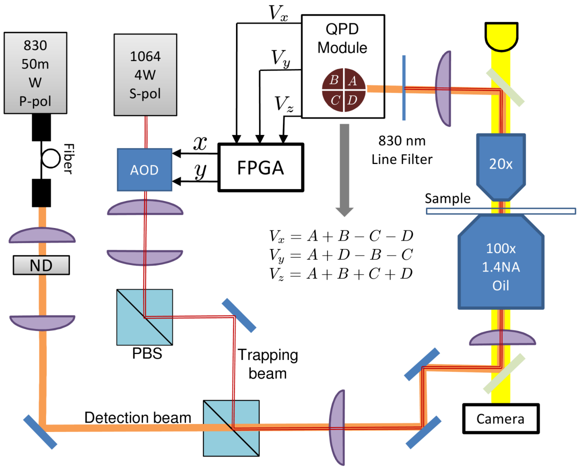

Figure 2.2: Schematic for our Optical Tweezer setup

## 2.2 Experimental Setup

For experiments we use a custom built optical tweezer setup (Fig.2.2) where a Nd:YAG trapping laser (CrystaLaser Inc., $\lambda = 1064nm$, $500mW$) [46, 47] is expanded using appropriate optics to fill the back aperture of high numerical aperture objective (Nikon 100x, 1.4 NA, oil immersion). The optical trap is formed at the focal point where spherical polystyrene beads are trapped. The trapping laser passes through 2-axis acousto-optic-detector (AOD, IntraAction Corp., $DTD - 274HA6$) that precisely steers the beam in x-y plane in response to appropriate commands. To detect the bead position, a second detection laser (Point Source Inc., $iFLEX$ 2000, 50 $mW$, $\lambda = 830nm$) is used to map the image of the bead onto a quadrant photodiode (QPD, Pacific Silicon Sensors, $QP50 - 6SD2$). The photodiode provides three signals $V_x$, $V_y$ and $V_z$ where $V_x$ and $V_y$ represent the light distribution on the photodiode along $x$ axis and $y$ axis respectively while $V_z$ corresponds to total light intensity. These signals are captured using FPGA based data acquisition system (National Instruments, $PCI7833R$) that generates appropriate commands for the AOD. Next, we characterize the dynamics of a bead in a laser trap.

## 2.3 Bead in a Single Well

### 2.3.1 Modeling

In this section we develop a realistic model of a bead in a viscous medium in an optical trap. The key objective is to obtain a model which is capable of providing a quantitative match with experimental data. The dynamics of a dielectric bead in a viscous fluid can be modeled as free Brownian motion [48], where the bead represents the system of interest and the viscous fluid around the bead acts like a heat bath. The effect of collision of fluid molecules with the dielectric bead, $f_d(t)$ is modeled as a linear superposition of a viscous drag force $-\gamma v(t)$, and a stochastic force, $\xi(t)$, as shown in (2.1),

$$f_d(t) = -\gamma v(t) + \xi(t), \tag{2.1}$$

where, $v$ is the velocity of the bead and $\gamma$ is the viscous friction coefficient. We assume that the bead is spherical, using Stoke's drag force model [49], $\gamma = 6\pi\eta r$ where, $\eta$ is the dynamic viscosity of the surrounding fluid and $r$ is the radius of the bead. The stochastic force in (2.1) is modeled as a white Gaussian process with ensemble averages $\langle \xi(t) \rangle = 0$ and $\langle \xi(t), \xi(t^{'}) \rangle = 2b\delta(t - t^{'})$, where it follows from the Fluctuation-Dissipation theorem [49] that,

$$b = \gamma k_B T \tag{2.2}$$

where, $k_B$ is the Boltzmann constant and $T$ is temperature of the heat bath with which the bead is interacting. The diffusion of the bead due to interaction with the heat bath is then described by

$$m\frac{dv}{dt} = -\gamma v + \xi(t) \tag{2.3}$$

where, $m$ is the mass of the bead. Note: We will be using the SDE representation given in [49], $\frac{dv}{dt}$ does not mean that $v(t)$ is smooth and is just a notation. The dynamics of a dielectric bead in a viscous fluid under the influence of a potential $U(x, a)$ can be modeled by the Langevin equation as shown below.

$$m\frac{dv}{dt} = -\frac{\partial U(x,a)}{\partial x} - \gamma v + \xi(t) \tag{2.4}$$

We propose a model for the potential due on an optical trap $U(x,a)$ which comprises of a reference energy $U_r$, harmonic potential region uptil a width $w$ and no force beyond this width:

$$U(x,a) = \begin{cases} \frac{1}{2}k(a)x^2 + U_r & \text{if } |x| \leq w \\ U(w,a) + U_r & \text{if } |x| > w. \end{cases} \tag{2.5}$$

Here, $k(a)$ denotes the trap stiffness which can be modulated by changing physical parameters $a$. For example: the parameter $a$ could be the intensity of the laser. Using (2.5) in (2.4), the Langevin equation reduces to

$$m\frac{dv}{dt} = -k(a)x - \gamma v + \xi(t), |x| \leq w. \tag{2.6}$$

The mass of the bead being very small ($\sim 10^{-16}$ kg) results in the inertia terms in (2.3) and (2.6) being insignificant. Neglecting the inertia term in (2.3) and (2.6) leads to (2.7) and (2.8) respectively. This is called the *overdamped dynamics approximation* of Brownian motion and Langevin equation respectively.

$$\frac{dx}{dt} = \frac{1}{\gamma}\xi(t), \text{ if } |x| > w \tag{2.7}$$

$$\frac{dx}{dt} = -\frac{k(a)}{\gamma}x + \frac{1}{\gamma}\xi(t), \text{ if } |x| \leq w \tag{2.8}$$

As long as the bead is under the influence of $U(x,a)$, its dynamics is modeled by (2.8). Outside the influence of the potential (that is, outside the width $w$) the bead undergoes free Brownian motion and its dynamics is modeled by (2.7). We will use (2.7) and (2.8) to simulate the dynamics of a bead in an optical trap using Monte Carlo methods and validate with experiments.

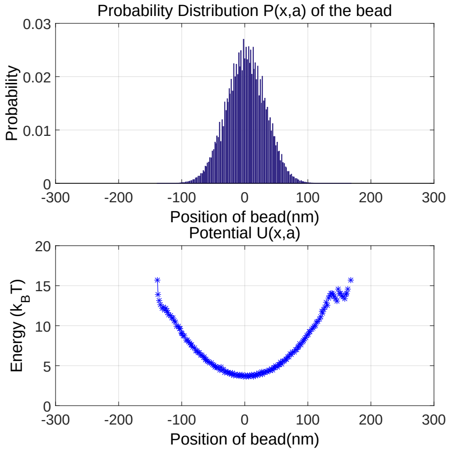

Figure 2.3: Probability distribution and potential for single well obtained from experiments

### 2.3.2 Experiments

Experimental data is obtained using a custom built optical tweezer that is used to trap a spherical polystyrene bead (1 $\mu m$ diameter). The bead position data is obtained using the quadrant photodiode (QPD). The nature of the potential $U(x, a)$ as seen by the bead is a function of laser intensity $a$ and can be determined from the position data of the bead in equilibrium by using the canonical distribution [50]. The spatial probability density of the bead in equilibruim is given by,

$$P(x, a) = Cexp(-\frac{U(x, a)}{k_B T})$$

where $C$ is a normalization constant. It follows that,

$$U(x, a) = -ln(\frac{P(x, a)}{C}) \tag{2.9}$$

Here, time scales of the experiment have to be long enough to allow the bead to attain thermal equilibrium. Note that the above equation computes potential energy in units of $k_B T$. The probability distribution and potential for a bead in a single potential well (Fig. 2.3) is obtained after tracking the bead position (in a single optical trap) for sufficiently long time (thus allowing it to equilibriate). It shows a parabolic nature uptil a finite distance $w \approx 150\ nm$ from the minima. To estimate nature of the potential beyond

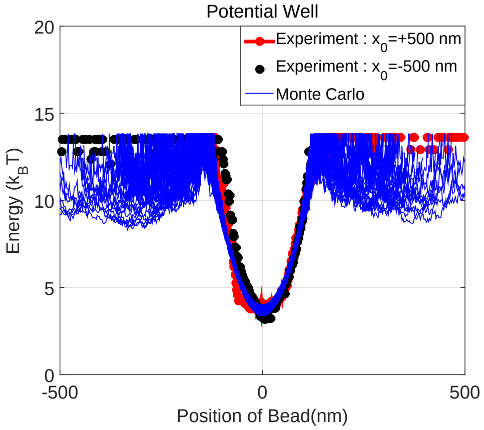

Figure 2.4: Estimating nature of single potential well beyond a distance $w \approx 150\ nm$ from the minima

$w$, the bead is released from an initial location of $\pm 500\ nm$ and its position is tracked from the moment of release till the bead attains equilibruim. The bead effectively sees a flat potential beyond $w$ (see Fig. 2.4), indicating that beyond a distance $w$ from the minima of $U(x, a)$, the bead dynamics are *primarily* dictated by thermal noise with no influence from the conservative forces due to the harmonic potential region of the optical trap. The bead is seen to spend little time in the non-harmonic region of the potential, justifying the flat potential approximation beyond the harmonic range. Thus the experimental data supports the model described by (2.5). The trap stiffness $k(a) = 0.0044\ pN/nm$ is obtained from the bead position data using Equipartition Theorem [50],

$$\frac{1}{2}k(a)\langle x^2 \rangle = \frac{1}{2}k_B T \tag{2.10}$$

and the dynamic viscosity of water at $300K$ is taken as $\eta = 8.9 \times 10^{-4} Pa.s$ [51] to obtain $\gamma = 8.3 \times 10^{-9} Ns/m$.

### 2.3.3 Monte Carlo Simulation

In this subsection we present a Monte-Carlo based simulation for a bead in an optical trap. The discretization of (2.7) and (2.8) using stochastic calculus [48] leads to (2.11) and (2.12) respectively [52].

$$x(t + \delta t) = x(t) + \sqrt{\frac{2k_B T}{\gamma} dt}\ \nu(t) \tag{2.11}$$

$$x(t + \delta t) = x(t) - \frac{k(a)}{\gamma} x(t)\delta t + \sqrt{\frac{2k_B T}{\gamma} \delta t}\ \nu(t) \tag{2.12}$$

where, $\nu(t) \in \mathcal{N}(0, 1)$. Here, $\mathcal{N}(0, 1)$ denotes the standard normal distribution. We choose the integration time step $\delta t = 10^{-5}s$ such that $\delta t << \frac{\gamma}{k(a)} \sim 10^{-3}s$. Note that $\frac{\gamma}{k(a)}$ represents the time constant of (2.8). The system parameters $k(a), \gamma$ and $w$ for simulations is obtained from experiments with temperature $T = 300$ K. The bead position obtained by iterating (2.11) and (2.12) is used to obtain $P(x, a)$, which is then used to obtain the effective potential experienced by the bead by using (2.9).

The simulation results of reconstructed potentials $U(x, a)$ as shown in Fig. 2.5 are obtained by simulating the trajectories of 100 particles whose initial conditions are chosen by sampling a number $u$ from the Uniform distribution in $[0, 1]$ as shown below.

```
if $u > 0.5$ then
    $x(0) = 10 \text{ nm} * \mathcal{N}(0, 1)$
else
    $x(0) = -10 \text{ nm} * \mathcal{N}(0, 1)$
end if
```

The simulaton duration is 20 seconds for each particle and is long enough for each particle to attain equilibrium. The position trajectory of each particle is used to obtain the overall effective potential experienced by the bead using (2.9) and is shown in Fig. 2.5. Comparing Fig. 2.5 and Fig. 2.3 it is seen that the potential reconstructed from the Monte Carlo simulations is in close agreement with the one obtained from experiments. The height of the well in both places is about 10 $k_B T$. In Fig. 2.4 we present a potential reconstructed from the trajectories of 100 particles collectively with $x(0) = 500\ nm$ if $u > 0.5$ otherwise $x(0) = -500\ nm$. It is evident from Fig. 2.4 that beyond the harmonic regime, both experiments and simulation exhibit a predominantly force zone. Note that the transition region for both experiments and Monte Carlo simulations is difficult to

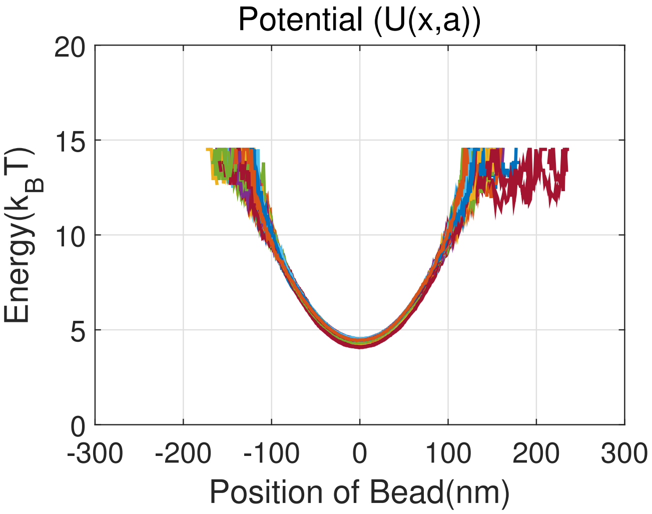

Figure 2.5: Potential wells obtained from Monte Carlo Simulations.

reconstruct from position data, as the bead spends very less time in that zone [53].

## 2.4 Summary

A first order model for a Brownian particle in an optical trap with experimentally derived parameters is able to explain the experimentally observed behavior accurately. The energy levels of the system of interest is in the $k_B T$ regime, making the system amenable for studies at very low energy levels. In the next chapter, we will use the Brownian particle in an optical trap system to physically create memory bits and study physics of computations, in particular, the Landauer's principle.

# Chapter 3

# Physics of Computation: Experimental demonstration of Information

## 3.1 Prologue

We wish to develop a model system which can be used to perform basic computational operations like OR, NOT, erasure (or rest) at the physical limits. Here, we will utilize the the Brownian particle in an optical trap setup described in the previous chapter to mimic a single bit memory. We will demonstrate erasing of information stored in the memory bit with energy expenditure very close to thermodynamic lower limit as given by the Landauer's principle. Although, the focus of this chapter is on the erasure operation; the framework can be extended to study other computational operations.

## 3.2 Introduction

Landauer's principle, pioneered by Rolf Landauer in 1961, provides a critical link between information theory and thermodynamics of physical systems [27]. It states that there is no process where the work done to erase one bit of information is less than $k_bT\ln 2$ (Landauer's bound), when the prior probability of the bit being in any of the two states is equal [54]. Here, $k_b$ is the Boltzmann constant and $T$ is the temperature of the heat bath.

Numerous analyses have corroborated Landauer's bound through different approaches [55, 56, 57, 58, 59]. The experimental study of Landauer's bound has only recently become viable, enabled by tools that provide access to processes with energetics in the scale of $k_bT$. A first such study in [60] examined Landauer's bound, by employing optical traps to realize a single bit memory. Bechhoefer et.al. [61, 62] used an anti-Brownian electrokinetic feedback trap and Hong et.al. [63] used nano magnetic memory bits to study Landauer's bound.

In this chapter, we study the energetics of transport realized by time multiplexing a harmonic potential of finite width, to realize a bi-stable potential. Here a single laser in an optical tweezer setup, is multiplexed between two locations with varying dwell times to create potentials (symmetric as well as asymmetric bi-stable potentials), that effectuate the erasure process. Furthermore, experimental variables to realize reversible erasure are identified and utilized for approaching the Landauer's bound. Langevin dynamics based simulations of a Brownian particle under the influence of a time multiplexed laser is developed and is shown to obey quantitative trends observed in experiments. We use our method of shaping the potential, by changing the dwell time of multiplexing of the laser, to erase one bit of information. The ease of implementation and the high-resolution accounting of energetics are advantages of the method reported. We resort to Sekimoto's stochastic energetics [64, 65, 66, 49] framework to quantify the work done on the system for the erasure process. The underlying principles developed are applicable toward the study of transport achieved by time multiplexing of a single potential, where realizations based on optical traps can be considered a particular instantiation of the general underpinnings of the framework presented.

## 3.3 Model for a One-Bit Memory

We use the abstraction of a Brownian particle in a symmetric double well potential (two valleys separated by a hill) to model a one-bit memory. The memory is designated the state 'zero' if the particle is in the left well, and the state 'one' if it is in the right well. This model has the properties as desired from a single bit memory. The Brownian particle has a large exit time across the barrier for a sufficiently high barrier, thus capable of retaining the stored information for a very long time. Being symmetric, both the states are of same energy level, hence there is no bias storing one state with lesser energy over another.

Experimentally, we realize a Brownian particle in a harmonic potential, albeit of finite width, by using a custom built optical tweezer setup to trap (near the focus of the objective lens) a polystyrene bead ($1\mu m$ in diameter) while suspended in deionized water. The bead represents the thermodynamic system of interest with the surrounding medium acting as a heat bath.

**Model of a Bead in a Laser Trap** A laser passing through a high numerical aperture objective lens and incident on a bead in a solution traps the bead. Here, the bead experiences a harmonic potential with the equilibrium point (trap center) located near the focus of the lens. For small displacements away from the centre of the trap, the bead experiences a restoring force directed towards the trap center [45, 43]; the trap behaves like a Hookean spring with the restoring force being $k\Delta x$, where $k$ is the stiffness of the trap and $\Delta x$ the distance between the bead center and the trap center. The position of the bead (denoted by $x$) is measured using a photo diode for a duration much larger than the time constant of the dynamics of the bead in the laser trap ($\sim 1ms$). The equilibrium probability distribution, $P(x)$, of the position of the bead, is then obtained by binning the measured position data. The potential energy landscape, $U(x)$, of the bead in thermal equilibrium with the trap is obtained using the relation, $U(x) = -\ln(\frac{P(x)}{C})$, where $C$ is the normalization constant. In Fig. 3.1, the potential energy landscape experienced by an optical bead in a laser trap is shown (red and black curves), which is constant outside a distance $w$ from the minimum of the potential and harmonic within the distance $w$ from the equilibrium point.

The potential energy $U(x)$ is modeled by,

$$U(x) = \begin{cases} \frac{1}{2}kx^2 + U_r, \text{ if } |x| \leq w \\ \frac{1}{2}kw^2 + U_r, \text{ if } |x| > w, \end{cases} \tag{3.1}$$

which is harmonic up till a distance $w$ (determined empirically from Fig. 3.1) from the stable equilibrium point. The stiffness $k$ of the optical trap is determined experimentally by applying the Equipartition Theorem, that yields $k = k_bT/\langle x^2 \rangle$ [67]. The dynamics

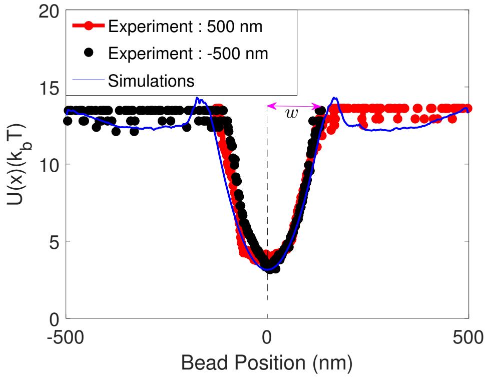

Figure 3.1: Potential energy landscape of a bead in a laser trap. The experiments are performed with the bead initially at 500 nm (red curve) and −500 nm (black curve). The position of the bead is measured for 50 seconds. The potential $U(x)$ is mostly flat after a certain distance $w$ from the stable equilibrium point. In the Monte Carlo simulations, the bead is initialized randomly between 500 nm and −500 nm. The position trajectory of the bead obtained from 100 Monte Carlo simulations is collected to determine $U(x)$ from simulations (blue curve).

of the bead in a trap is modeled by the over-damped Langevin equation [49],

$$-\gamma\frac{dx}{dt}+\xi(t)-\frac{\partial U(x)}{\partial x}=0, \tag{3.2}$$

where, $\gamma$ is the coefficient of viscosity (determined experimentally by step response method [43]), $U(x)$ is the potential realized by the trap and $\xi(t)$ is a zero mean uncorrelated Gaussian noise force. Here, $\langle\xi(t)\rangle = 0$, $\langle\xi(t),\xi(t^{'})\rangle = 2D\delta(t-t^{'})$ with the diffusion coefficient $D = \gamma k_b T$. The potential $U(x)$ described by (3.1) is used in conjunction with (3.2) to obtain 100 realizations (of 20 seconds each) of the bead trajectories. These realizations are, in turn, used to reconstruct the potential felt by the bead by binning the position trajectories. A close match with experimental results is seen, as shown in Fig. 3.1.

**Double Well Potential Model of Memory:** A double well potential with two locally stable equilibrium points located at $L$ and $-L$ is created by alternately focusing the trapping laser between the two locations by time-multiplexing using an Acousto Optical Deflector. The laser is multiplexed at least 100 times faster than the time constant of the dynamics of the bead. The trapping laser multiplexed at the two locations is the external agent coupled to the thermodynamic system of interest formed by the

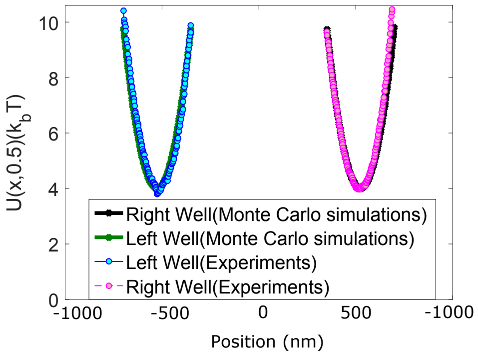

Figure 3.2: Double well potential for $L = 550\ nm$ obtained using Monte-Carlo simulations and experiments.

bead. We define duty-ratio $d$ as the fraction of the total time-period the laser spends at the location $-L$. The nature of the effective potential experienced by the Brownian particle can be manipulated by adjusting the duty-ratio. The potential energy landscape, $U(x, d)$, experienced by the bead for a duty-ratio $d$, is determined by the relationship $P_d(x) = Ce^{-U(x,d)/k_bT}$, where $P_d(x)$ is determined by binning the measured position of the bead. Maintaining a duty-ratio of 0.5 results in near identical parabolic potential wells at $L$ and $-L$ as shown in Fig. 3.2, while a duty-ratio greater than 0.5 leads to asymmetric double well potentials as shown in Fig. 3.3.

The bead dynamics under the influence of time multiplexed potential is modeled by the following Langevin equation,

$$-\gamma\frac{dx}{dt} + \xi(t) - \frac{\partial U(x,d)}{\partial x} = 0, \tag{3.3}$$

where, the model for the potential $U(x, d)$ used in (3.3) incorporates the experimental observation that, for the duration when the laser remains focused at the location $L$ or $-L$, the bead experiences a harmonic potential up till a distance $w$ from the trap focus. However, beyond the distance $w$ from the locally stable equilibrium points $L$ or $-L$, the bead undergoes a random walk [68]. Based on these observations, the potential $U(x, d)$ is modeled by,

$$U(x,d) = \begin{cases} \frac{1}{2}k(x-L)^2 + U_r, \text{ if } |x-L| \leq w, r(t)=1, \\ \frac{1}{2}k(x+L)^2 + U_r, \text{ if } |x+L| \leq w, r(t)=0, \\ \frac{1}{2}kw^2 + U_r, \text{ otherwise,} \end{cases} \tag{3.4}$$

where, $r(t)$ denotes the binary variable representing the presence/absence status of the laser at $L$. If the laser is focused at $L$, then $r(t) = 1$, otherwise $r(t) = 0$. The stiffness of the laser trap, $k$, and the width of the corresponding parabolic potential, $w$, are determined by characterization of the finite width harmonic potential obtained due to a single trap, as described earlier in (3.1). The laser is multiplexed between the two locations at a significantly faster rate ($\sim 10\mu s$) than the time constant of the bead dynamics ($\sim 1ms$), which supports the model in (3.4). Monte Carlo simulations performed using (3.3) and the subsequent potential $U(x,d)$ reconstructed from bead position data, (using the canonical distribution) yield potentials that match closely with experimental observations as seen in Fig. 3.2. We remark that in the Monte Carlo simulations as well as in experiments, the stiffness of each of the wells formed at $L$ and $-L$ when the duty-ratio is 0.5 is close to $\frac{k}{2}$, which is half the stiffness of the single trap. In summary, the model parameters ($k$ and $w$) determined for a single trap is used in the Monte Carlo simulations of the bead in a double well potential realized by time multiplexing of the trapping laser. A close match between simulation and experimental results is observed as shown in Fig. 3.2. Using the Brownian particle in a double well potential model of a single bit memory, we next present an erasure protocol based on multiplexing of potentials.

## 3.4 Erasure Process

Erasure is a logically irreversible operation [26], where irrespective of the initial state of the memory, the final state is zero (also known as 'reset-to-zero' operation). A bead in a double well potential is used to model a single bit memory. No prior information on the state of the memory is assumed initially; thus, it is equally likely that the memory assumes the state zero or one. However, at the end of erasure process the memory state

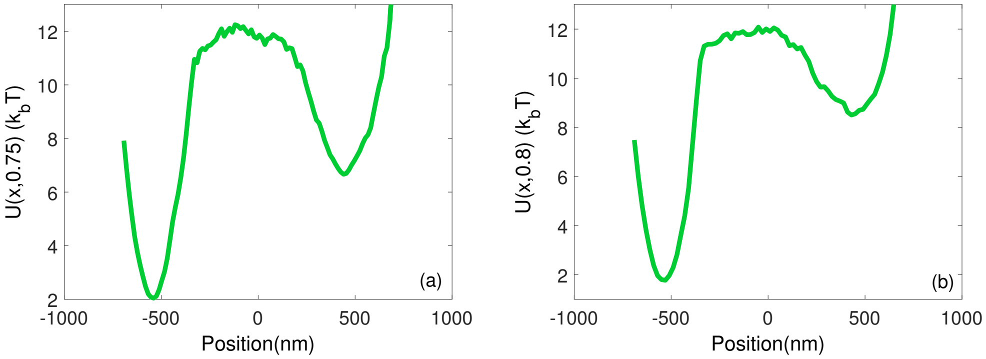

Figure 3.3: Effect of duty-ratio on the nature of double well potential. Increasing the duty-ratio at $-L$ from 0.75 to 0.8 increases the asymmetry of the potential.

is *zero* (the bead must be in the left well). Thus, there is no change in average energy of the bead in an erasure process (as the depth of both wells is the same) while the decrease in entropy associated with erasure is $k_b \ln 2$; thereby requiring at least $k_b T \ln 2$ amount of work to be done on the system [54]. We note that the Landauer's bound is applicable to the average work done on the system over many realizations of the bead trajectory, but, it is possible to obtain individual erasure realizations with the work done on the system less than $k_b T \ln 2$. Indeed we demonstrate later that for a fraction of trajectories, the work done on the bead is lower than $k_b T \ln 2$ (see Fig. 6).

The Landauer's bound of $k_b T \ln 2$ holds if the erasure process is always successful. It can be shown that for imperfect erasure schemes with the probability of successful erasure being $p$, at least $k_b T(\ln 2 + p \ln p + (1-p)\ln(1-p))$ amount of work is required to be done on the system [54]. It is important to note that the bound decays rapidly as $p$ decreases from 1; with the bound being $k_b T \ln 2$ for $p = 1$ and zero for $p = 0.5$. In our study, we ensure that $p > 0.95$ and assume that the erasure process is always successful.

The erasure protocol is described next where duty-ratio is the fraction of the time spent by the laser at the location, $-L$ (see Fig. 3.4(c)), as compared to $L$; higher the duty-ratio more is the time spent by the laser at $-L$. In the first phase of the protocol, the memory model of a Brownian particle in a symmetric double well potential is obtained by maintaining a duty ratio of 0.5 for a duration of 10 seconds. Next, in the second phase of the protocol, an asymmetric well is realized, with the well at $-L$ deeper than the well at $L$, which is obtained by maintaining the duty-ratio to be greater than 0.5 for a duration (dependent on the choice of $d$) of $\tau$ seconds. Finally, we revert

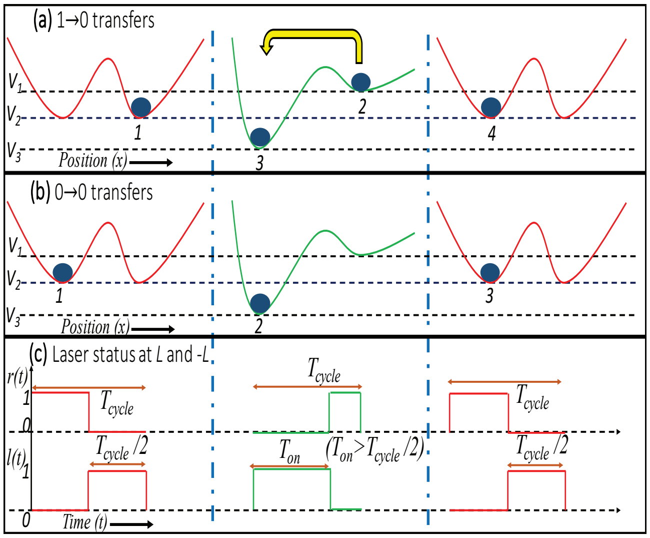

Figure 3.4: (a) Schematic showing erasure process, with bead initially in the right well. The initial bead position is 1 (right well), with potential energy $V_2$. The duty-ratio $d$ at left well is then increased, which lifts the bead and takes it to position 2 with energy $V_1$. Thermal fluctuations enables the bead to cross the barrier and reach position 3, with energy $V_3$. Decreasing the duty-ratio back to 0.5 lifts the bead to position 4, which has energy $V_2$. The process $1 \rightarrow 2 \rightarrow 3 \rightarrow 4$ is the erasure process. (b) Schematic showing erasure process, with bead initially in the left well. Here, the process $1 \rightarrow 2 \rightarrow 3$ is the erasure process. (c) The signals $r(t)$ and $l(t)$ denote the presence/ absence status of the laser at $L$ and $-L$ respectively. A value of 1 means present and 0 means absent. To ensure a duty-ratio greater than 0.5, we maintain $d = T_{on}/T_{\text{cycle}} > 0.5$.

the duty-ratio to a value of 0.5 to complete the 'reset to zero' process (for a duration of 10 seconds). The success of erasing the memory depends, on the magnitude of the deviation of the duty ratio from 0.5 and the time duration $\tau$ during the second phase.

In the second phase, over the time duration $\tau$, the laser spends more time focused at $-L$ than at $L$, enabling an asymmetric potential landscape as is observed in Fig. 3.3. Increasing the duty-ratio results in a lower barrier height for the right to left transition than for the left to right transition. It thus favors the transport of the bead from the right to the left well, if the bead is initially in the right well as shown in Fig. 3.4(a) and retains the bead in the left well if it was initially in the left well as shown in Fig. 3.4(b). The duration $\tau$ is chosen to be a few multiples of the average exit time of the bead from the right well but less than the average exit time of the bead from the left well, which ensures a high likelihood of the bead's final location to be in the left well. For example, we choose $\tau$ as 30 seconds for the duty ratio of 0.7, which is approximately three times the observed exit time of the bead from the right well.

The above mentioned erasure mechanism ensures high success proportion as reported in Fig. 3.5. It is seen that the duty-ratio of 0.65 yields success proportion significantly less than 0.95, while a duty-ratio $> 0.7$ shows a success proportion greater than 0.95. Similar trends are reflected from Monte Carlo simulations as well as experiments as seen in Fig. 3.5. Thus, to ensure a high success proportion in order to demonstrate erasures with energy expenditure close to the Landauer's bound, we operate our erasure protocol at a duty ratio of at least 0.7. In the next section, we quantify the work done on the bead in an erasure process for a given duty-ratio.

## 3.5 Erasure Thermodynamics

We now utilize the stochastic-energetics framework for Langevin systems [66, 49] and quantify the work done on the system, associated with erasure process realized by manipulation of duty-ratios. The external system does work on the bead by changing the duty-ratio, which results in modifying the potential felt by the bead. For an erasure process, the work done on the bead, $dW$, is given by,

$$dW = \sum_j [U(x(t_j), d(t_j^+)) - U(x(t_j), d(t_j^-)], \tag{3.5}$$

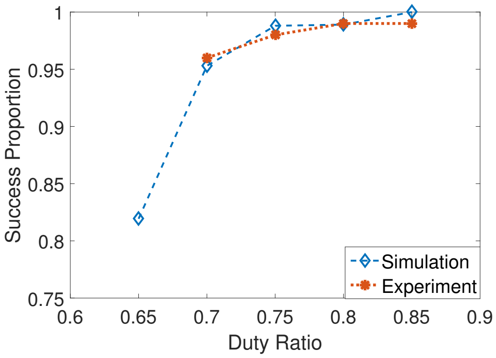

Figure 3.5: Effect of duty-ratio on success proportion $p$. Duty-ratio of 0.65 has a success proportion of 0.82, whereas, duty-ratio greater than 0.7 yields success proportion higher than 0.95.

where $d$ denotes the discontinuous parameter (here, the duty-ratio) changed by the external system, and $t_j$ denotes the time instances when the parameter was changed ($t_j^-$ and $t_j^+$ denote the instants just before and after changing the parameter respectively).

Landauer's bound can be reached when the erasure process is performed in a quasi static manner. For an erasure performed over a large but finite duration $\tau$, the average work done on the system is [65],

$$\langle dW \rangle = dW_{Landauer} + \frac{B}{\tau} \tag{3.6}$$

where, $dW_{Landauer} = k_b T \ln 2 = 0.693 k_b T$. The duration for which an asymmetric double well potential is realized, $\tau$, is chosen to be a multiple of the exit time, $\tau_e$, of the bead from the right well. It is known that $\tau_e \propto \frac{\exp(\delta U_r)}{\sqrt{k_r}}$, [48] where $\delta U_r$ is the barrier height of the right well, $k_r$ is the stiffness of the right well and exp(.) is the exponential function. Note that $d - 0.5$ is indicative of the asymmetric nature of the double well potential; higher the value, more the asymmetry. We determine the dependency of $\delta U_r$ and $k_r$ on $\frac{1}{d-0.5}$ empirically. The dependency of normalized $\delta U_r$ and $k_r$ on $\frac{1}{d-0.5}$ is shown in Fig. 3.6 and 3.7 respectively. It follows that $\tau \propto \tau_e \propto \frac{\exp(\frac{0.99}{d-0.5})}{\sqrt{\frac{1}{d-0.5}}}$. Substituting it in (3.6) for $\tau$ leads to,

$$\langle dW \rangle = dW_{Landauer} + B\frac{\exp(-\frac{0.99}{d-0.5})}{\sqrt{d-0.5}}. \tag{3.7}$$

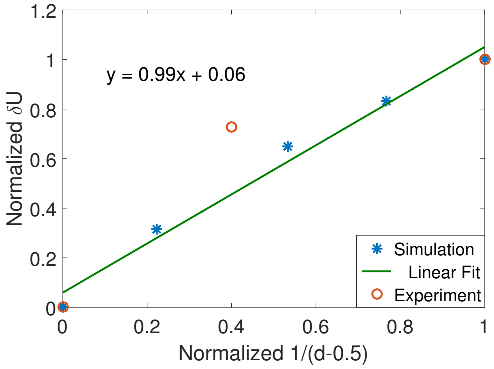

Figure 3.6: The blue and red points represent normalized barrier height of right well as a function of $\frac{1}{d-0.5}$ obtained using simulations and experiments respectively. The green line is the least squares fit to the simulation data points.

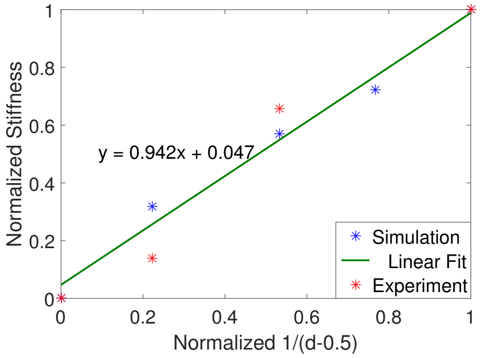

Figure 3.7: The blue and red points represent normalized stiffness of right well as a function of $\frac{1}{d-0.5}$ obtained using simulations and experiments respectively. The green line is the least squares fit to the simulation data points.

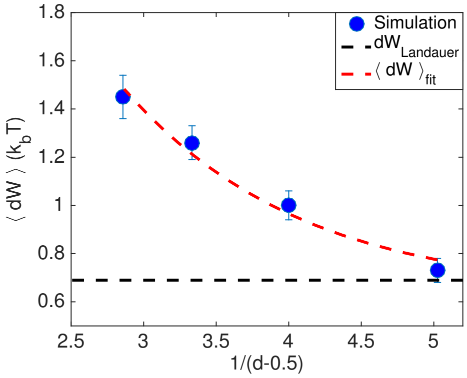

Figure 3.8: The blue circles represent the average work done on the bead obtained using 300 Monte Carlo realizations (150, $0 \to 0$ and 150, $1 \to 0$ transfers) for duty ratio of $0.7, 0.75, 0.8, 0.85$. The vertical lines represent the standard error in mean for each duty ratio. The black dotted line denotes the the Landauer bound of $k_bT \ln 2$. The red dotted line is the fit with the free parameters $A$ and $B$.

Reducing $d$, the time duration $\tau$ required for successful erasures increases, whereby the erasure process approaches a quasi-static process. Thus, the duty-ratio provides a handle to realize quasi-static erasure processes using time multiplexed potentials.

The average work done on the bead $\langle dW \rangle$, for duty-ratio $d > 0.7$ obtained using simulations and experiments is shown in Fig. 3.8 and Fig. 3.9 respectively. For a duty-ratio of 0.7, average work done on the system obtained from Monte Carlo simulations is $0.73 \pm 0.037 k_bT$, while experimentally for duty-ratio of 0.7, the average work done on the bead is obtained to be $0.9 \pm 0.106 k_bT$. The average work of $0.9 \pm 0.106 k_bT$ to erase a bit of information is the closest to the Landauer's bound of $k_bT \ln 2$ reported. As the duty-ratio is reduced ($1/(d - 0.5)$ increased), the average work done on the bead decreases, as observed in simulations as well as experiments.

We fit the model derived in (3.7), $\langle dW \rangle_{fit} = A + B\frac{\exp(-\frac{0.99}{d-0.5})}{\sqrt{d-0.5}}$ to the average work done on the bead obtained by simulations and experiments for various duty-ratio values, with $A$ and $B$ being free parameters (see Fig. 3.9). Using simulation data we obtain $A = 0.65 k_bT, B = 8.49 k_bT$, whereas for experimental data we have $A = 0.70 k_bT, B = 35.04 k_bT$. It is seen that $A$ (which represents the average work done on the system in the quasi-static case) has a value close to the Landauer bound of $k_bT \ln 2$ ($= 0.693 k_bT$), in both simulations as well as experiments.

The distribution of work done while erasing a bit at a duty-ratio of 0.7, obtained

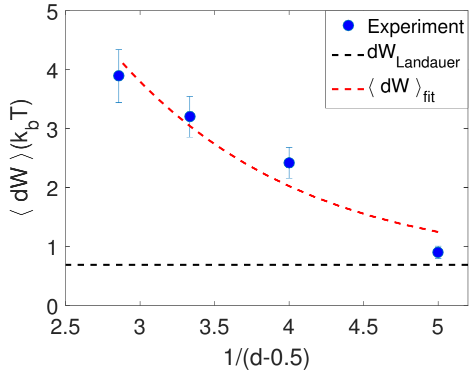

Figure 3.9: The blue circles represent the average work done on the bead obtained from 100 experiments (50, $0 \to 1$ and 50, $1 \to 1$ transfers) for duty-ratio of $0.7, 0.75, 0.8, 0.85$. The vertical lines represent the standard error in mean for each duty-ratio. The black dotted line denotes the the Landauer bound of $k_b T \ln 2$. The red dotted line is the fit with the free parameters $A$ and $B$.

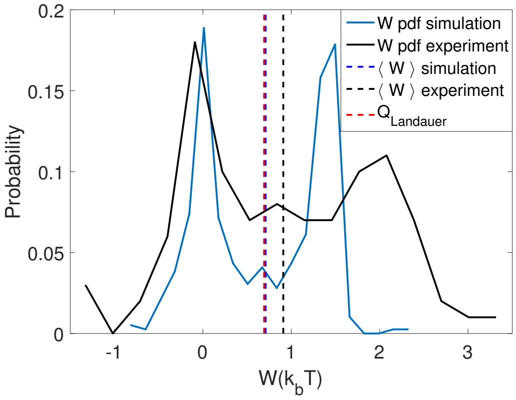

Figure 3.10: Distribution of work done on the bead obtained from simulations and experiments for a duty-ratio of 0.7. The nature of the distribution is bimodal.

from simulations and experiments is shown in Fig. 3.10. It is evident that for a fraction of trajectories, the work done on the bead is less than the Landauer's bound; indeed, for some trajectories it is negative. However, the mean of the distribution is close to the Landauer's bound. Moreover, a bimodal nature of the distribution is evident. The mode on the right in Fig. 3.10 corresponds to work done on the particle for transition from right to left well (or $1 \rightarrow 0$) and mode on the left corresponds to transition from left to left well (or $0 \rightarrow 0$). The characteristics of the simulation data are confirmed by experiments as shown in Fig. 3.10. On increasing the duty-ratio, the mode on the right shifts further to the right as work done on the bead is higher for higher duty-ratios. This results in an increase in the standard error in mean on increasing duty ratio as shown by the length of the blue bars in Fig. 3.8 and Fig. 3.9.

Thus we have demonstrated that a single bit memory and its associated erasure protocol can be realized by multiplexing a laser between two locations. The resulting energetics can be effectively accounted for in the framework developed by Sekimoto and the magnitude of the deviation of the the duty-ratio of multiplexing from 0.5 provides an effective means for driving the erasure process toward a quasistatic process.

**Error Quantification:** The primary sources of error in the average work done on the system computed from position measurements are introduced by the photodiode based measurements. The error statistics of the photo diode used in the experiments are quantified in [69] and is shown to have zero mean and a standard deviation of the order of a nanometer. Assuming that error in position measurement $e_x$ is independent of the actual bead position $x$, the average error in potential energy of the bead $e_U$ is given by,

$$\begin{aligned}\langle e_U \rangle &= \langle \frac{1}{2}k(x + e_x - L)^2 - \frac{1}{2}k(x - L)^2 \rangle \\ &= \frac{1}{2}k\langle e_x^2 \rangle \sim 10^{-3} k_b T.\end{aligned}$$

Thus, error in obtaining the work done on the bead in a realization of erasure is of the order of $10^{-3} k_b T$.

## 3.6 Summary

We presented the thermodynamics of a Brownian particle influenced by the time multiplexing of a single harmonic potential of finite width. A Monte Carlo simulation framework for a Brownian particle under the influence of a time multiplexed laser is also developed and shown to obey qualitative trends observed in experiments. We demonstrate that the duty-ratio provides a handle on the speed of the erasure process and its approach to reversibility. It is established through experiments and simulations that reducing duty ratio results in erasure process with average work done approaching $k_b T \ln 2$; which is the minimum average work required to erase one bit of information. Furthermore, the method is easy to implement on a standard optical tweezer setup. The insights obtained from this article can be potentially leveraged to realize practical devices that yield erasure mechanisms with energetics in the order of $k_b T \ln 2$.

Next, we will study the thermodynamic and kinetic aspects of erasure of a bit of information analytically.

# Chapter 4

# Physics of Computation: Analysis of Information Erasure

## 4.1 Prologue

In the previous chapter, we demonstrated erasure of information very close to the physical limits as dictated by the Landauer's principle using experiments as well as Monte Carlo simulations. In this chapter, we present a framework for analysis of information erasure using ideas from Information theory and Gaussian mixture distributions. In particular we analyze the effect of closeness of the two valleys in a single bit memory on the Landauer's limit as well as reliability of the erasure protocol. We show that a compromise on the accuracy of erasure lowers the minimum energy expenditure required for information erasure below the Landauer's limit. The analysis framework is also applicable to other computational processes like OR, NOT and others.

## 4.2 Introduction

A prevalent model of a single bit memory is a Brownian particle in a symmetric double well potential in a heat bath at constant temperature $T$, with the two identical wells separated by a barrier as shown in Fig. 4.1. The presence of the particle in either well denotes one of the possible two states of a single bit memory. Here, we designate the particle's presence in the left well and right well as state zero and one of the memory,

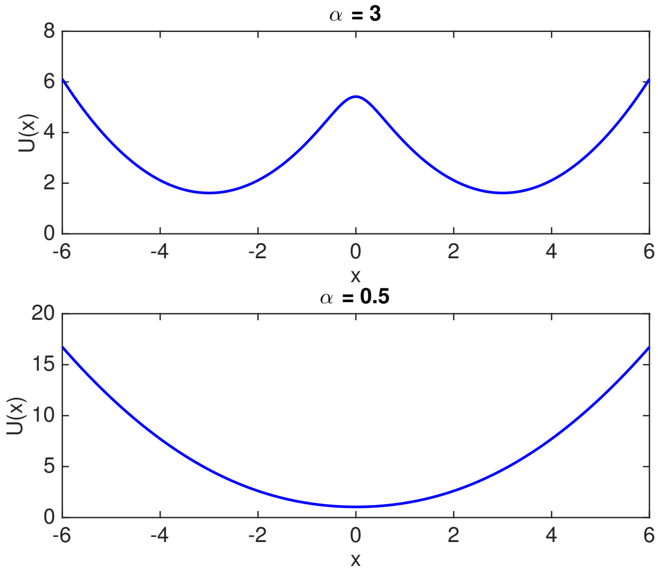

Figure 4.1: A symmetric double well potential, $U(x)$, where the location of the particle in the left and right well designate the state zero and one respectively of a single bit memory. Here, $E$ denotes the barrier height.

respectively. The presence of an energy barrier of sufficient height ($\gg k_BT$, $k_B$ is the Boltzmann constant), ensures that information is retained for a long duration, as is desired from a memory bit. A shorter barrier height($\approx k_BT$) will result in a higher probability of the particle moving from one well to another due to thermal fluctuations, which is undesirable as it renders the information contained in the memory bit unreliable. Erasure of a bit of information is a reset to zero operation, where we consider the erasure process successful if the particle is in the left well at the termination of the erasure process, irrespective of the initial state of the memory.

Landauer's principle [27], asserts that, erasure of a bit of information, provided both states of a single bit memory are identical, is accompanied by an average heat dissipation of at least $k_BT\ln 2$. Landauer argued that erasure of information lowers the entropy of the overall system and thus, is accompanied by heat dissipation to the surrounding. Bennett further utilized Landauer's argument to explain Maxwell's demon to avoid a paradox violating the second law of thermodynamics [26, 70]. Following the original work of Landauer, there are numerous analytical [55, 56] and experimental studies [60, 61, 63, 62, 71, 72, 73] focused on the minimal energy consumption related to information processing.

A recent research interest is on analyzing erasure mechanisms which result in heat dissipation lower than $k_B T \ln 2$ (which is the Landauer's bound). In this regard, researchers have studied the effect of uncertainty in the erasure process and have shown that partially successful erasures result in heat dissipation lower than the Landauer's bound [74, 75]. It is shown in [74, 75] that the lower bound on the heat dissipation is given by $k_B T(\ln 2 + p \ln p + (1-p)\ln(1-p))$, termed the *Generalized Landauer Bound (GLB)*, where $p$ is the probability of reliability of the erasure process. An interesting observation reached by analyzing GLB is that, a slight compromise on accuracy (by about 10%) of the erasure process holds the potential for lowering the associated minimum heat dissipation significantly (by about 50%). An important assumption made in arriving at the GLB in [55, 72, 73] is that, there is 'insignificant' overlap between the two physical states that realize the single bit memory, that is, the two states of a memory bit have sufficient 'physical separation'. Such an assumption is implicit in the experimental studies as well [60, 61, 63, 62, 71]. The effect of reduction in physical dimension on energetic and reliability aspects is not well established. Here, we analyze the effect of overlap of the two wells in a single bit memory with regards to heat dissipation in erasure of information as well as reliability of stored information. We study the relationship between the Generalized Landauer Bound (GLB) and the average time from either well to cross the barrier at the origin with regards to the physical separation between the two states of a one bit memory (that is, 'size' of the memory bit).

Our approach introduces an 'overlap parameter' and uses properties of mixture of Gaussian distributions to derive bounds on change in entropy associated with information erasure as well as average time of loss of stored information. The derived bounds on the entropy change converge to the GLB when the overlap between the two states become 'insignificant' and hence is consistent with existing results in the literature [74, 75, 55]. We quantify the relationship between the overlap and the reduction in entropy change and utilize it to arrive at GLB. Here, we derive sub-Gaussian upper bounds analytically as opposed to the numerical study of entropy approximations for bit erasure in [76]. Furthermore, we obtain complimentary lower bounds on the decrease in thermodynamic entropy, demonstrating that these bounds are reasonably sharp; and for bi-stable wells, physically separated by lengths close to their standard deviation, the error in entropy approximation incurred by the 'insignificant overlap' approximation is significant. These quantitative results are of immediate application as they allow a tight approximation of the change in entropy in erasure process, relevant to the precise estimation of the associated minimal heat dissipation. A quantitative analysis is also provided for the case when the two states of memory are non identical and the erasure process moves the state into the well with higher/ lower volume. Furthermore, we use mean first passage time [48] results to quantify the relationship between reliability of stored information in a memory bit and the overlap parameter. We quantify that a trade-off exists between lowering the minimum heat dissipation in information erasure and improving reliability of information stored in a single bit memory. Moreover, we determine a threshold on the overlap parameter, where a value higher than the threshold has minor benefits from the energetics as well as reliability standpoint. The threshold value can be used to determine memory densities that strike a good trade-off between reliability and thermodynamic cost of computations.

We provide analytical results that are very pertinent and timely to the current research focus of studying fundamentals of energetics of computations. The aim is to understand the effects of reducing size of fundamental building blocks of information storage devices on the thermodynamic and reliability aspects of computations. In our analysis, a smaller value of the overlap parameter implies a smaller size of the memory bit. The change in entropy bounds derived would also be applicable to enable analysis of other processes in the field of thermodynamics of information involving a mixture of Gaussian distributions; for example; in feedback processes where mutual information between system state and measurement is a key quantity of interest [77]. Moreover, the derived bounds on change in entropy have shown to be applicable in information theory [78], for analyzing capacity bounds of a channel transmitting discrete values corrupted by independent Gaussian noise. The analysis is also motivated by new paradigms of computation; for example, in stochastic computation [79] and neuromorphic memory architectures [80], where, uncertainty of the success of computation is allowed and modeled a-priori.

## 4.3 Single Bit Memory and Erasure with Uncertainty

### 4.3.1 Single Bit Memory

Following the original work of [27], we consider a Brownian particle in a double well potential as a model for a single bit memory. The location of the particle, $x$, in either well designates the state of the memory as 0 or 1. In this article, if the particle is located in the left well ($x < 0$), we denote the state of memory as 0 and if the particle is located in the right well ($x \geq 0$), we denote the state as 1. The particle in either well is in thermal equilibrium with the surrounding whose temperature is assumed to be a constant $T$. For most part of this article, we assume that both the wells are identical unless specified.

In recent experimental validations of Landauer's principle [60, 81, 61, 71], it is seen that the double well potential in the neighborhood of the two stable states can be approximated as a convex quadratic function; locally. It then follows from the canonical distribution expression that the equilibrium probability distribution is approximately a Gaussian distribution around the minimum of each of the well. Henceforth, we assume that the equilibrium probability distributions of the particle in the left and right well are $\mathcal{N}(-\mu, \sigma^2)$ and $\mathcal{N}(\mu, \sigma^2)$ respectively, where $\mathcal{N}(\mu, \sigma^2)$ denotes a Normal distribution with mean $\mu$ and variance $\sigma^2$. Thus, if the memory is in the state 0 the equilibrium probability distribution of the particle is $f_0(x) = Ce^{-(x+\mu)^2/2\sigma^2}$ and if the memory state is 1 the equilibrium probability distribution of the particle state is $f_1(x) = Ce^{-(x-\mu)^2/2\sigma^2}$, where $x$ denotes the position of the particle and $C$ is the normalization constant. This assumption is consistent with the notion of memory as described in [54], where a single bit memory is defined as a system with two stable states, such that, the system is locally in equilibrium in either state and stays in one of the stable states (information retention) for the duration the memory bit is valid (related to the exit time across a barrier).

Here, we study the effect of overlap between the two wells of the double well potential (that is, the effect of overlap between the two equilibrium probability distributions of the two states of a single bit memory) on the Landauer's bound. The two distributions intersect at $x = 0$, where, $f_0(0) = f_1(0) = Ce^{-\alpha^2/2}$ with $\alpha := \mu/\sigma$. Thus, the overlap between the two distributions is characterized by the parameter $\alpha$, which is referred to as the **overlap parameter**. Higher(lower) the value of $\alpha$, lower(greater) is the overlap between the two equilibrium distributions. Moreover, $\alpha$ is also indicative of the aspect ratio of the memory bit as well as physical extent of the memory bit for a known standard deviation of the equilibrium probability distributions.

Prior to erasure, it is equally likely for the state of the memory, $M$, to be zero or one, that is, $P(M = 0) = P(M = 1) = \frac{1}{2}$. The probability of finding the Brownian particle between $x$ and $x + dx$ is given by,

$$\begin{aligned} P(X \in (x, x + dx)) &= P(M = 0)P(X \in (x, x + dx)|M = 0) \\ &\quad + P(M = 1)P(X \in (x, x + dx)|M = 1) \\ &= \frac{1}{2}f_0(x)dx + \frac{1}{2}f_1(x)dx. \end{aligned} \tag{4.1}$$

Thus, the probability distribution function, $f(x)$, of the particle prior to undergoing an erasure process, is an equally weighted mixture of $f_0(x)$ and $f_1(x)$. In order to represent a valid single bit memory, this distribution must be a bi-modal distribution (due to a symmetric double well stable potential). In this regard, an interesting result is that: an equally weighted mixture of symmetric Gaussian distributions is uni-modal if and only if $\alpha \leq 1$; otherwise it is bi-modal [82]. Thus, in order to represent a symmetric single bit memory with two well defined states, $f(x)$ needs to be a bi-modal distribution with the two modes being alike. Hence, a single bit memory must have $\alpha > 1$ in order to be a valid memory bit. Fig. 4.2 and Fig. 4.3 show the probability distribution $f(x)$ and potential $U(x)$ respectively for $\alpha = 3$ and $\alpha = 0.5$. It is seen that the distribution is uni-modal (the corresponding potential is a single well potential) for $\alpha = 0.5$, and cannot be used to realize the two states of a single bit memory. However, $\alpha = 3$, results in a symmetric bi-modal distribution and a symmetric double well potential as seen in Fig. 4.3, which results in a well defined memory bit. It is important to note that the overlap parameter $\alpha$ depends on the physical design of the memory bit (the double well potential precisely). Recent studies on Landauer's bound [60, 81, 61, 71] used $\alpha \approx 20$.

Based on the above model of a single bit memory, there is a non zero probability to commit an error in judging the state of the memory, $M$, from the measured position of the Brownian particle $x$. This is because $P(M = 0|X \in (x, x + dx)) > 0$ for all $x \in \mathbb{R}$, which implies, there is a non zero probability for the memory $M$ to be in state 0 or 1, irrespective of any value of the position of the Brownian particle. Consider a threshold

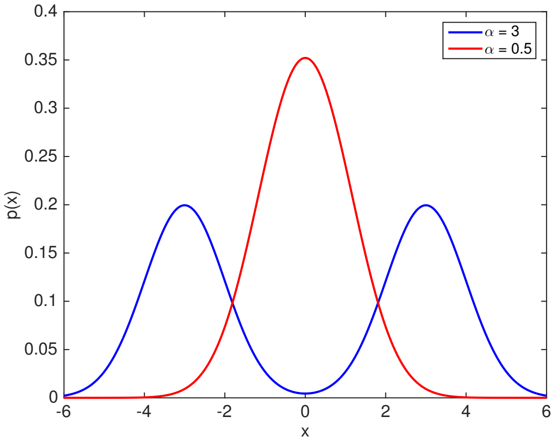

Figure 4.2: Probability distribution for $\alpha = 0.5$ and $\alpha = 3$.

$\mathcal{T}$ such that if $x < \mathcal{T}$, then we infer $M = 0$ otherwise $M = 1$. The mis-classification error probability, $P(E)$, is given as,

$$P(E) = \frac{1}{2}\int_{x<\mathcal{T}} e^{-(x-\mu)^2/2\sigma^2}dx + \frac{1}{2}\int_{x>\mathcal{T}} e^{-(x+\mu)^2/2\sigma^2}dx. \tag{4.2}$$

It is shown in [83] that $P(E)$ is minimum if $\mathcal{T} = 0$. In the rest of the manuscript we choose $\mathcal{T} = 0$, which is an optimal choice and is also used in recent experimental studies on the Laundauer's principle [60, 61, 71]. $P(E)$ is a quantifier of the loss of information which approaches zero if the overlap parameter $\alpha := \mu/\sigma$ approaches $\infty$. This means that, as the overlap between the two wells becomes insignificant, the loss of information vanishes and the state of the memory bit can be identified accurately from position of the Brownian particle.We now analyze the effect of the overlap parameter on energetics of erasure of one bit of information.

### 4.3.2 Erasure with Uncertainty

Erasure is a process where irrespective of the initial state of the memory bit, the final state is zero (also known as *reset to zero*). In a double well potential representation of a single bit memory erasure entails that the particle needs to be transferred to the left well; irrespective of the initial position of the particle. Erasure is achieved using a particle transfer protocol(also referred as erasure protocol), which reliably moves the Brownian particle to the left of the origin. We associate reliability parameter, $p$, with

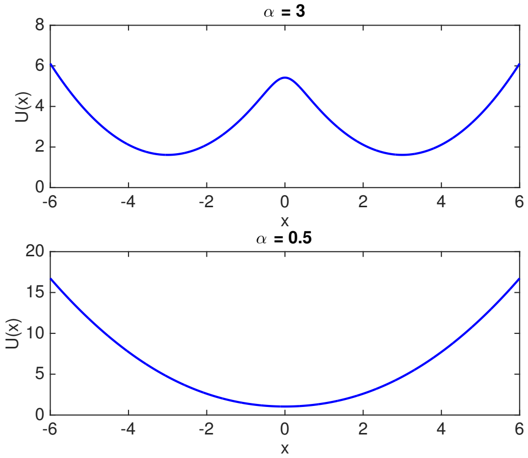

Figure 4.3: Potential $U(x)$ landscape for $\alpha = 0.5$ and $\alpha = 3$. The potential $U(x)$ is computed using the Canonical distribution relation, $p(x) = \frac{e^{-U(x)/k_BT}}{\mathcal{Z}}$, where, $\mathcal{Z}$ denotes the normalization constant.

the erasure protocol, where, $p := P(M = 0)$ after application of the erasure protocol. The Generalized Landauer Bound (GLB) from [74, 75, 60] states that, if the reliability parameter of the erasure process is $p$, then the associated average heat dissipation is at least $k_BT(\ln 2 + p \ln p + (1-p)\ln(1-p))$. The GLB evaluates to $k_BT \ln 2$ for $p = 1$; to 0 for $p = 0.5$ and is shown in Fig. 4.4 as a function of the reliability parameter $p$. Note that $p < 0.5$ is not considered here as it would imply a reset to one operation. It is important to point out that the reliability parameter, $p$, depends on the specific protocol used for accomplishing the erasure and will be referred to as the protocol reliability parameter. We would like to bring the attention of the reader to [60, 84, 71], where, the authors discuss the dependence of protocol reliability parameter on speed of the erasure process.

Under the assumption of $\alpha > 1$, we analyze the effect of overlap parameter $\alpha$ on the Generalized Landauer Bound. The probability distribution function of the particle before undergoing erasure, $f(x)$, is given by, $f(x) = \frac{1}{2}f_0(x) + \frac{1}{2}f_1(x)$ (see eq. (4.1)). After applying an erasure protocol to the memory bit with reliability parameter $p$, the probability of finding a particle between $x$ and $x + dx$ is given by,

$$P(X \in (x, x + dx)) = pf_0(x)dx + (1-p)f_1(x)dx. \tag{4.3}$$

Let, $g(x) := pf_0(x) + (1-p)f_1(x)$. The thermodynamic entropy of the system before erasure is, $S_f = -k_B \int_{-\infty}^{\infty} f(x)\ln(f(x))dx$, and after undergoing erasure process using a

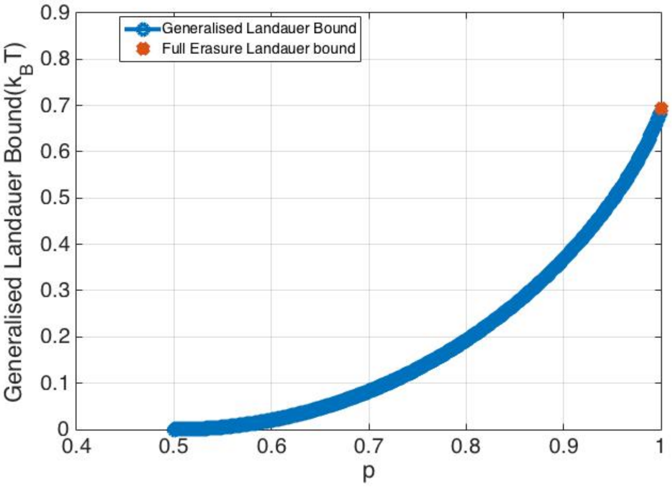

Figure 4.4: GLB as a function of protocol reliability parameter $p$.

protocol with reliability parameter $p$ is, $S_g = -k_B \int_{-\infty}^{\infty} g(x)\ln(g(x))dx$. It follows from the $2^{nd}$ Law of Thermodynamics that the average heat dissipation,

$$\langle Q_d \rangle \geq T(S_f - S_g) = k_B T(I_1 - I_2),$$

where, $I_1 = \alpha^2 - \frac{1}{\sqrt{2\pi}\alpha} e^{-\frac{\alpha^2}{2}} \int_{-\infty}^{\infty} e^{-\frac{x^2}{2\alpha^2}} \cosh(x)\ln(\cosh(x))dx$ and $I_2 = \alpha^2 - \frac{1}{\sqrt{2\pi}\alpha} e^{-\frac{\alpha^2}{2}} \int_{-\infty}^{\infty} e^{-\frac{x^2}{2\alpha^2}} (pe^{-x} + (1-p)e^{x})\ln(pe^{-x} + (1-p)e^{x})dx$. The dependence of $I_1 - I_2$ on the overlap parameter $\alpha$, is shown in Fig. 4.5. It is seen that $k_B T(I_1 - I_2)$ approaches the GLB for large values of the overlap parameter $\alpha$. Note that for $\alpha \leq 2.1$, the decrease in thermodynamic entropy, $k_B(I_1 - I_2)$ is less than $k_B(p\ln p + (1-p)\ln(1-p) + \ln 2)$ and is well approximated by $k_B(p\ln p + (1-p)\ln(1-p) + \ln 2)$, when $\alpha > 5$. As seen from Fig. 4.5, for a given protocol reliability parameter $p$ and $1 < \alpha < 5$, the associated minimum average heat dissipation due to erasure is lower than the GLB. Hence, allowing overlap (by reducing the physical separation) between the two states of the memory bit can enable energy dissipation lower than the GLB in an erasure process.

We remark that the protocol reliability parameter $p$ is dependent on the protocol used for performing erasure and the overlap parameter $\alpha$ of the memory bit. There is a subtle difference between the protocol reliability parameter $p$ and the probability of success of an erasure, $p_s$, and is discussed below.

Without loss of generality, it can be assumed that if the position of the particle is

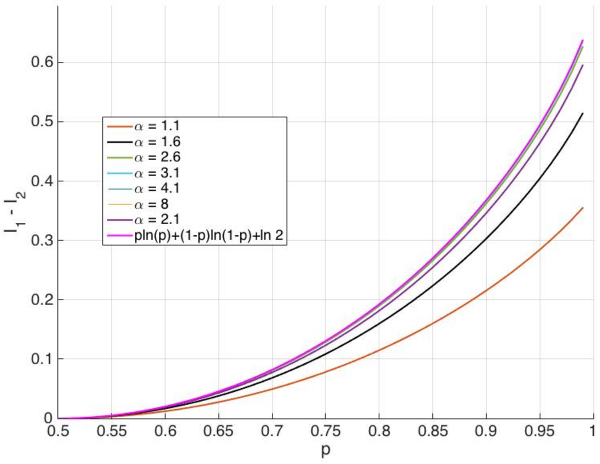

Figure 4.5: $I_1 - I_2$ as a function of $p$ for various values of $\alpha$. $I_1 - I_2$ approaches $p \ln p + (1-p)\ln(1-p) + \ln 2$ (pink curve) as $\alpha$ increases.

to the left of the origin, the state of the memory is deemed as 0; the erasure process is considered successful if after application of the erasure protocol the position of the particle, $x$, is observed to be less than zero. Thus the probability of success, $p_s$, of the erasure process is given by,

$$\begin{aligned} p_s = P(X<0) &= p\int_{-\infty}^{0} \frac{1}{\sqrt{2\pi\sigma^2}} e^{-\frac{(x+\mu)^2}{2\sigma^2}}dx + (1-p)\int_{-\infty}^{0} \frac{1}{\sqrt{2\pi\sigma^2}} e^{-\frac{(x-\mu)^2}{2\sigma^2}}dx \\ &= p\int_{-\infty}^{\alpha} \frac{1}{\sqrt{2\pi}} e^{-\frac{u^2}{2}}du + (1-p)\int_{-\infty}^{-\alpha} \frac{1}{\sqrt{2\pi}} e^{-\frac{v^2}{2}}dv, u := \frac{x}{\sigma}+\alpha, v := \frac{x}{\sigma}-\alpha, \\ &= \frac{1}{2}\operatorname{erfc}(\alpha/\sqrt{2}) + p \times \operatorname{erf}(\alpha/\sqrt{2}), \end{aligned} \tag{4.4}$$

where, erf and erfc denote the Gaussian error and complementary error function. Thus, in the limit $\alpha \to \infty, p_s \to p$. In Figure 4.6, we plot $p_s$ by varying $\alpha$ and $p$. It is seen that for $\alpha \geq 3$, $p_s$ is very close to $p$. Thus, $p_s$ can be considered as a good approximation of $p$ for $\alpha \geq 3$. Empirically, $p_s$ is determined by applying the specified protocol to several realizations of the memory bit and then observing what fraction of those resulted in the particle being located to the left of the origin after the completion of the protocol [60, 61, 71]. Once an estimate of $p_s$ is known, with the knowledge of $\alpha$, the protocol reliability parameter can be estimated.

In the next section, we derive upper and lower bounds to the change in entropy as a

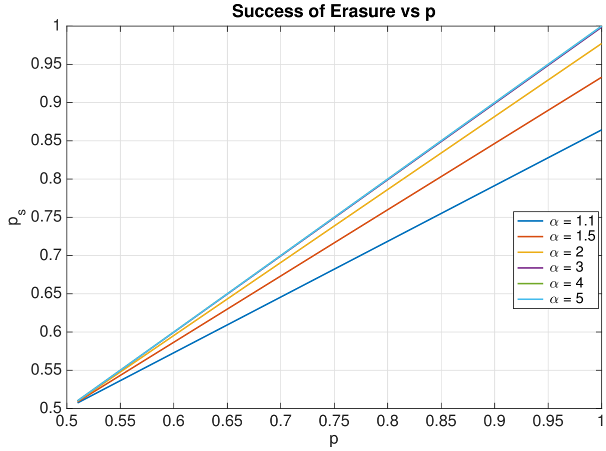

Figure 4.6: Variation of probability of success of erasure as a function of the overlap parameter and protocol reliability parameter $p$.

function of the protocol reliability parameter $p$ and overlap parameter $\alpha$.

## 4.4 Effect of Overlap parameter on Thermodynamic Cost of Erasure

### 4.4.1 Upper and lower bounds on the change in entropy during erasure

We will establish in this section that the following upper and and lower bounds on the decrease in entropy, $S_f - S_g$,

$$S_f - S_g \leq k_B(\ln 2 - H(p) - \ln{(1+e^{-2\alpha^2})} + C(2 - H(p) + 4\alpha^2)e^{-\alpha^2/2}), \text{ and,} \tag{4.5}$$

$$S_f - S_g \geq k_B(\ln 2 - H(p) - C(2+4\alpha^2+\ln 2)e^{-\alpha^2/2} + p\ln(1+\frac{1-p}{p}e^{-2\alpha^2}) + (1-p)\ln(1+\frac{p}{1-p}e^{-2\alpha^2})). \tag{4.6}$$

Here, $H(p) := -p\ln p - (1-p)\ln{(1-p)}$.Consider, a probability distribution function(pdf), $g(.) := p\mathcal{N}(-\mu,\sigma^2) + (1-p)\mathcal{N}(\mu,\sigma^2)$, and another pdf, $\overline{g}(.) := p\mathcal{N}(-\alpha,1) + (1-p)\mathcal{N}(\alpha,1)$, where $\alpha$ is the overlap parameter $\frac{\mu}{\sigma}$. Then, $S_g = S_{\overline{g}} + k_B\ln\sigma$ [85]. Similarly, for $p=\frac{1}{2}$, with $f(.) = \frac{1}{2}\mathcal{N}(-\mu,\sigma^2)+\frac{1}{2}\mathcal{N}(\mu,\sigma^2)$ and $\overline{f}(.) := \frac{1}{2}\mathcal{N}(-\alpha,1)+\frac{1}{2}\mathcal{N}(\alpha,1)$, we have $S_f = S_{\overline{f}} + k_B\ln\sigma$. Thus, $S_f - S_g = S_{\overline{f}} - S_{\overline{g}}$. In the derivations below we are interested in the change in entropy between an initial pdf described by $f$ and a final distribution described by $g$. It is evident from the relation above that we can limit our discussion to $g = pN(-\alpha, 1) + (1-p)N(\alpha, 1)$ and $f = \frac{1}{2}\mathcal{N}(-\alpha, 1) + \frac{1}{2}\mathcal{N}(\alpha, 1)$. We also use $f_0(x) = Ce^{-\frac{(x+\alpha^2)}{2}}$ and $f_1(x) = Ce^{-\frac{(x-\alpha^2)}{2}}$, where $C = \frac{1}{\sqrt{2\pi}}$.

For the derivation below it is assumed that $p \in [0.5, 1)$ and $\alpha > 1$.

It follows (see Appendix) that,

$$\begin{aligned}&\int_{-\infty}^{\infty} pf_0(x)\ln(pf_0(x) + (1-p)f_1(x))dx - \\ &\int_{-\infty}^{\infty} pf_0(x)\ln(pf_0(x))dx \\ &< C(2(1-p) + p\ln(\frac{e^{4\alpha^2}}{p}))e^{-\alpha^2/2}.\end{aligned} \tag{4.7}$$

Similarly, one can show that,

$$\begin{aligned}&\int_{-\infty}^{\infty} (1-p)f_1(x)\ln(pf_0(x) + (1-p)f_1(x))dx \\ &- \int_{-\infty}^{\infty} (1-p)f_1(x)\ln((1-p)f_1(x))dx \\ &< C(2p + (1-p)\ln(\frac{e^{4\alpha^2}}{1-p}))e^{-\alpha^2/2}.\end{aligned} \tag{4.8}$$

Let $K := \int_{-\infty}^{\infty} f_0(x)\ln(f_0(x))dx = \int_{-\infty}^{\infty} f_1(x)\ln(f_1(x))dx$. Using eq. (4.7) and eq. (4.8) with $p = \frac{1}{2}$ leads to the following lower bound on $S_f$,

$$S_f \geq k_B(-K + \ln 2 - C(2 + 4\alpha^2 + \ln 2)e^{-\alpha^2/2}). \tag{4.9}$$

From eq. (4.7) and (4.8), it also follows that,

$$\begin{aligned}-S_g \leq\ & k_B(p\ln p + (1-p)\ln(1-p) + K \\ &+ C(2 + p\ln p + (1-p)\ln(1-p) + 4\alpha^2)e^{-\alpha^2/2}).\end{aligned} \tag{4.10}$$

In the Appendix, we also derive the following lower bounds,

$$\int_{-\infty}^{\infty} pf_0(x)\ln(pf_0(x)+(1-p)f_1(x))dx - \int_{-\infty}^{\infty} pf_0(x)\ln(pf_0(x))dx \geq p\ln(1+\frac{1-p}{p}e^{-2\alpha^2}), \text{and}, \tag{4.11}$$

$$\int_{-\infty}^{\infty}(1-p)f_1(x)\ln(pf_0(x)+(1-p)f_1(x))dx - \int_{-\infty}^{\infty}(1-p)f_1(x)\ln((1-p)f_1(x))dx$$
$$\geq (1-p)\ln(1+\frac{p}{1-p}e^{-2\alpha^2}). \tag{4.12}$$

Using eq. (4.11) and (4.12) with $p = 1/2$, we obtain the following upper bound on $S_f$,

$$S_f \leq k_B(-K+\ln 2-\ln(1+e^{-2\alpha^2})). \tag{4.13}$$

Furthermore, from eq. (4.11) and (4.12), we obtain the following lower bound on $-S_g$,

$$-S_g \geq k_B(K+p\ln p+(1-p)\ln(1-p)+p\ln(1+\frac{1-p}{p}e^{-2\alpha^2})+(1-p)\ln(1+\frac{p}{1-p}e^{-2\alpha^2})). \tag{4.14}$$

It follows from eq. (4.9) and (4.13) that,

$$\begin{aligned} &k_B(-K+\ln 2-C(2+4\alpha^2+\ln 2)e^{-\alpha^2/2}) \\ &\leq S_f \leq k_B(-K+\ln 2-\ln(1+e^{-2\alpha^2})). \end{aligned} \tag{4.15}$$

Similarly, it follows from eq. (4.10) and (4.14) that,

$$\begin{aligned} &k_B(K-H(p)+p\ln(1+\frac{1-p}{p}e^{-2\alpha^2})+(1-p)\ln(1+\frac{p}{1-p}e^{-2\alpha^2})) \\ &\leq -S_g \leq k_B(K-H(p)+C(2-H(p)+4\alpha^2)e^{-\alpha^2/2}), \end{aligned} \tag{4.16}$$

where, $H(p) = -p\ln p-(1-p)\ln(1-p)$. Using eq. (4.15) and (4.16), it is concluded that the difference between the initial and final entropy, $S_f - S_g$, satisfies the bounds in eq. (4.5) and (4.6).

The case of $p = 1$ has to be considered separately. If $p = 1$, $g(x) = f_0(x)$ and

$-S_g = k_B K$. It then follows from eq. (4.9) and (4.13) that,

$$S_f - S_g \geq k_B(\ln 2 - C(2 + 4\alpha^2 + \ln 2)e^{-\alpha^2/2}),$$
$$S_f - S_g \leq k_B(\ln 2 - \ln(1 + e^{-2\alpha^2})).$$

In the case $p = 1$ as well, it follows that $\lim_{\alpha\to\infty} S_f - S_g = k_B \ln(2)$, which is the Landauer's bound.

### 4.4.2 Relationship to the Generalized Landauer Bound

Note from eq. (4.5) and (4.6), $\lim_{\alpha\to\infty} S_f - S_g = k_B[\ln(2) + p\ln(p) + (1-p)\ln(1-p)]$(GLB); where the upper and lower bounds on the change in entropy, both converge to the GLB. The convergence to the limit is with respect to the overlap parameter $\alpha$ is exponentially fast for both the upper and lower bound. Thus, in the limiting case of $\alpha \to \infty$, it follows from the $2^{nd}$ Law of Thermodynamics that, $\frac{\langle Q_d \rangle}{T} \geq k_B[\ln(2) + p\ln(p) + (1-p)\ln(1-p)]$, implying that for a quasi static erasure using a protocol with reliability parameter $p$, $\langle Q_d \rangle = k_B T[\ln(2) + p\ln(p) + (1-p)\ln(1-p)]$. In Figure 4.7, we present the derived lower and upper bounds on $(S_f - S_g)/k_B$ as a function of the overlap parameter for $p = 0.8$. The exponential convergence to the GLB value for $p = 0.8$ is evident. Table 4.1 lists the difference between the upper (eq. (4.5)) and lower (eq. (4.6)) bounds of $(S_f - S_g)/k_B$ for various values of the overlap parameter, $\alpha$, and protocol reliability parameter, $p$. It is seen that, the difference is significant for $\alpha < 5$ and is almost zero for $\alpha = 5$(insignificant overlap). Here, it is seen that with a threshold of 5 for the overlap parameter $\alpha$, increasing $\alpha$ beyond the threshold accrues only marginal gains energetically. The recent experimental studies on verification of the Landauer's bound [60, 71, 61] employed $\alpha \approx 20$, indicating that there is considerable scope to increase the density of the resulting memory.

### 4.4.3 Extensions to Asymmetric 1 bit Memory

An asymmetric one bit memory and the associated minimum heat dissipation for its erasure is discussed in [54, 62]. In particular, [62] presents an experimental study of the minimum heat dissipation for perfect erasures of a bit of asymmetric memory, with one well being wider than the other, and considers the two cases of resetting the bit into the

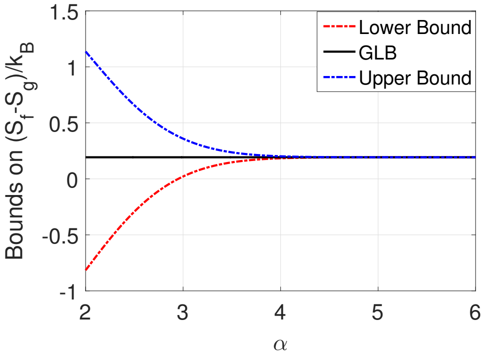

Figure 4.7: Lower and Upper bounds of $(S_f - S_g)/k_B$ and the GLB as a function of $\alpha$ for $p = 0.8$.

Table 4.1: Difference between the upper(eq. (4.5)) and lower(eq. (4.6)) bounds of $(S_f - S_g)/k_B$ as a function of $\alpha$ and $p$.

| $\alpha$ \ $p$ | 0.6 | 0.7 | 0.8 |
|---|---|---|---|
| 1.5 | 2.829 | 2.838 | 2.852 |
| 2.0 | 1.944 | 1.947 | 1.953 |
| 2.5 | 0.946 | 0.948 | 0.949 |
| 3.0 | 0.336 | 0.337 | 0.338 |
| 5.0 | $3.033e^{-4}$ | $3.034e^{-4}$ | $3.035e^{-4}$ |

wider and narrower well. Motivated from the discussion in [62], we extend the GLB to the case of non-identical wells, where, one well is wider than the other.

We assume that initially, the particle has equal probability to be in either well and the initial probability distribution of the particle is given by $f(x)$ as described earlier (see eq. (4.1)). Similarly, for erasures using a protocol with reliability parameter $p$, the final probability distribution of the particle is given as $g(x)$ (see eq. (4.3)).

**Erasing into low entropy well**

Consider $f_0(x) = Ce^{-\frac{(x+\mu)^2}{2\sigma^2}}$ and $f_1(x) = \frac{C}{\beta}e^{-\frac{(x-\mu)^2}{2(\beta\sigma)^2}}$ with $\beta > 1$. The particle has higher entropy in the state 1 as compared to state 0. In this case, for 'reset to zero' with protocol reliability parameter $p$, one can show that,

$$\begin{aligned}
&k_B\left(-\frac{C}{2}\left(2+\frac{9\alpha^2}{2}+\ln 2\right)e^{-\alpha^2/2} - \frac{C}{2}\left(2+\ln 2+\ln\beta+4\alpha^2\right)e^{-\alpha^2/2\beta^2}\right)\\
&\le S_f - S_g - k_B\left(\ln 2 + p\ln p + (1-p)\ln(1-p) + \left(\frac{1}{2}-(1-p)\right)\ln\beta\right) \le\\
&k_B\left(C\left(2p + p\ln\Big(\frac{e^{9\alpha^2/2}}{p}\Big)\right)e^{-\alpha^2/2} + C\left(2(1-p)+(1-p)\ln\Big(\frac{\beta e^{4\alpha^2}}{1-p}\Big)\right)\right)
\end{aligned} \tag{4.17}$$

Thus, $\lim_{\alpha\to\infty} S_f - S_g = k_B[p\ln p + (1-p)\ln(1-p) + (\frac{1}{2}-(1-p))\ln\beta + \ln 2]$. The rate of convergence is exponential with respect to the parameter $\alpha$ and depends inversely on the parameter $\beta$. Thus, in the limiting case of the two wells being sufficiently far apart and a quasi-static erasure process with protocol reliability parameter $p$, $\langle Q_d\rangle = k_BT[p\ln p + (1-p)\ln(1-p) + (\frac{1}{2}-(1-p))\ln\beta + \ln 2]$. Here, the bit was erased into the well with lower entropy, hence, the limiting value of the change in entropy is higher than the identical wells case. In Figure 4.8 the heat dissipation associated with erasing into the low entropy well is shown for various values of the asymmetry parameter $\beta$ and is compared with the Generalized Landauer Bound. It is seen that, as the asymmetry parameter is increased, the associated heat dissipation also increases for various protocol reliability parameters. The case of erasing into the high entropy well is more relevant and is presented next.

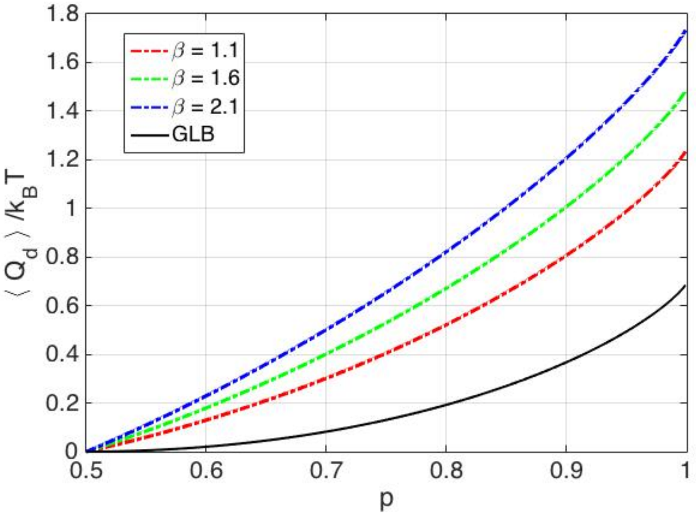

Figure 4.8: Minimum heat dissipation associated with erasing into low entropy well in a quasi static manner.

### Erasing into high entropy well

Consider erasing into the higher entropy well, that is, $f_1(x) = Ce^{-\frac{(x-\mu)^2}{2\sigma^2}}$ and $f_0(x) = \frac{C}{\beta}e^{-\frac{(x+\mu)^2}{2(\beta\sigma)^2}}$ with $\beta > 1$. Here, the particle has higher entropy in the state 0 as compared to state 1. In this case, for 'reset to zero' with protocol reliability parameter $p$, one can arrive at inequalities like the previous case by replacing $\beta$ with $1/\beta$ in eq. (4.17). It then follows that, $\lim_{\alpha\to\infty} S_f - S_g = k_B[p\ln p + (1-p)\ln(1-p) + ((1-p) - \frac{1}{2})\ln\beta + \ln 2]$. In the limiting case of the two wells being sufficiently far apart, for a quasi-static process, $\langle Q_d\rangle = k_BT[p\ln p + (1-p)\ln(1-p) - (\frac{1}{2} - (1-p))\ln\beta + \ln 2]$. Here, the bit was erased into the well with higher entropy, hence, the limiting value of the change in entropy is lower than the identical wells case. In Figure 4.9, the heat dissipation associated with erasing into the high entropy well is shown for various values of the asymmetry parameter $\beta$ and is compared with the Generalized Landauer Bound. It is seen that, as the asymmetry parameter is increased, the associated heat dissipation decreases for various protocol reliability parameters. In this case, it is seen that erasure can be achieved without any associated heat dissipation. Hence, asymmetry can be utilized toward realizing logically irreversible computations with zero dissipation.

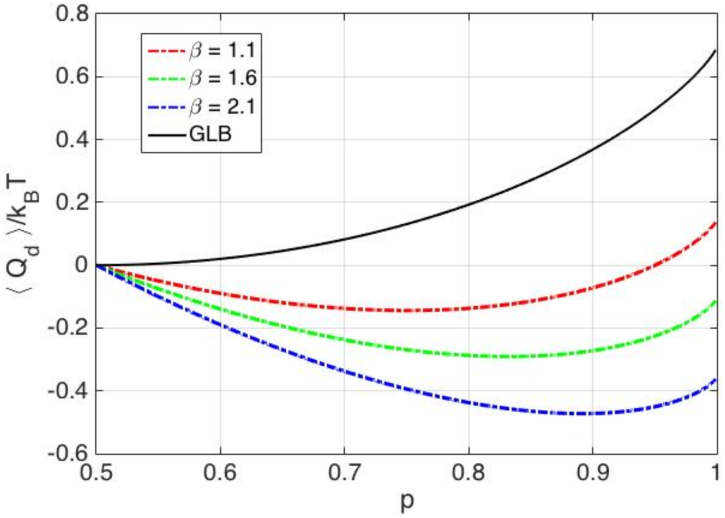

Figure 4.9: Minimum heat dissipation associated with erasing into high entropy well in a quasi static manner.

## 4.5 Effect of Overlap Parameter on the Reliability of a memory bit

In the previous sections, it is seen that a smaller value of the overlap parameter $\alpha$ results in lower minimum average heat dissipation for quasi static bit erasures. A smaller value of $\alpha$ implies a lower barrier height $(U(0) - U(\mu))$, thereby resulting in transitions of the Brownian particle between the two wells. If such a transition occurs frequently then the memory bit is considered unreliable. In this section, we quantify the degree of unreliability of a memory bit as a function of the overlap parameter $\alpha$. Although the discussions in the previous sections are for quasi static erasures, the exit time results of this section are more relevant for erasures achieved in finite time.

We will use the mean exit time from the mean of a well (right or left) to the barrier (at the origin) as a metric to quantify the reliability of the bit. A desirable mean exit time from either well to the barrier is several years to ensure reliability of stored information in the memory bit. The mean exit time across the barrier (at $x = 0$) from the mean of the right well (at $x = \mu$), denoted by $T(\mu \to 0)$, (under the assumption of stochastic dynamics of the Brownian particle being governed by the overdamped Langevin equation

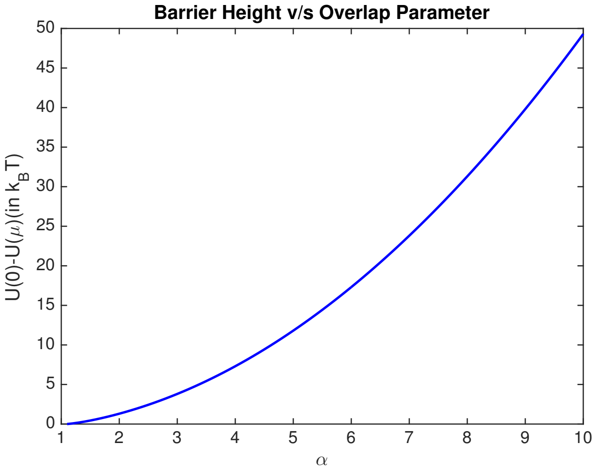

Figure 4.10: Barrier height in $k_BT$ as a function of the overlap parameter.

[49]) is given as [86],

$$T(\mu \to 0) = \pi \sqrt{\frac{|U''(0)|}{U''(\mu)}} e^{(U(0)-U(\mu))/k_BT}, \tag{4.18}$$

where, it follows from the canonical distribution that, $U(x)/k_BT = -\ln p(x)/\mathcal{Z}$. Here, $f(x)$ denotes the equilibrium probability density, which is given as, $f(x) = \frac{1}{2}\mathcal{N}(\mu, \sigma) + \frac{1}{2}\mathcal{N}(-\mu, \sigma)$ and $\mathcal{Z}$ is the normalization constant. The barrier height, $U(0) - U(\alpha)$ is given as,

$$\frac{U(0) - U(\mu)}{k_BT} = \ln \frac{f(\mu)}{f(0)} = \ln \frac{e^{\alpha^2/2}(1 + e^{-2\alpha^2})}{2} = \frac{\alpha^2}{2} + \ln\left(1 + e^{-2\alpha^2}\right) - \ln 2. \tag{4.19}$$

Thus, the barrier height, to a good approximation, is a quadratic function of the overlap parameter. In Fig. 4.10 the increase in barrier height on increasing the overlap parameter is shown. It is evident that as the overlap between the two wells decreases, the barrier height at the origin increases relative to the minima of the two wells and it is less likely to find the particle closer to the barrier. Using eq. (4.19) and substituting the expressions for $U^{''}(\mu), U^{''}(0)$ in eq. (4.18) leads to,

$$T(\mu \to 0) = \frac{\pi}{2} \sqrt{\frac{\alpha^2 - 1}{1 - \alpha^2 \operatorname{sech}^2(\alpha^2/\sigma)}} e^{\alpha^2/2}(1 + e^{-2\alpha^2}). \tag{4.20}$$

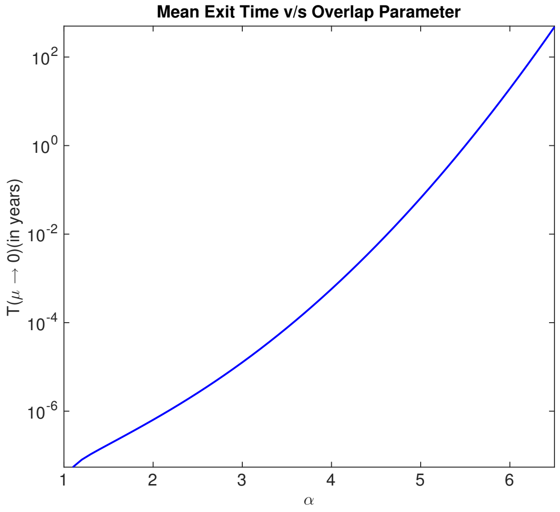

Figure 4.11: Mean exit time as a function of the overlap parameter for $\sigma = 1$.

In Figure 4.11, we show the the variation of mean exit time with respect to the overlap parameter $\alpha$. It is seen that the mean exit time from the mean of the right well (or the left well) increases exponentially as $\alpha$ increases. It is seen that $\alpha \approx 7$ has a mean exit of several hundred years. Based on our analysis, we conclude that reliability of the memory bit has exponential quadratic improvement while the minimum average heat dissipation has quadratic exponential decay to the GLB on increasing the overlap parameter $\alpha$. Thus, the trade-off between energy dissipation in erasing information and reliability of the memory can be decided by a judicious choice of the overlap parameter.

## 4.6 Summary

We quantified the dependence of the decrease in entropy associated with erasure of a bit of information on the amount of overlap between the equilibrium distributions of the two states of a one bit memory. It is seen that overlap can lead to considerably lower heat dissipation as compared to the GLB in a quasi static erasure process. This is primarily due to loss of information, primarily in the region between the two wells. We quantified the effect of loss of information on the change in entropy associated with partial information erasure by deriving tight upper and lower bounds, which exponentially converge to the GLB when the physical separation between the two states is large (loss of information is 0). A conclusion is reached that $\alpha \approx 5$ represents a threshold for energetics of computation associated with a single bit memory, where memory bit designs with $\alpha > 5$ have insignificant gains compared to $\alpha \approx 5$ case from an energetics perspective. Furthermore, the effect of asymmetry between the two wells of a single bit memory on the associated minimum heat dissipation for erasure processes is analyzed. Finally, we used mean exit time across a barrier relationships to demonstrate the effect of the overlap parameter on the reliability of the bit. It is seen that a higher value of the overlap parameter results in a higher mean exit time and hence, a more reliable memory. A slight change in the overlap parameter resulted in exponential improvement of the bit reliability. Thus, we arrive at a trade-off between minimizing heat dissipation and improving bit reliability by introducing overlap between the two wells of a memory bit. We showed that $\alpha \approx 7$ resulted in bit reliability of several hundred years; beyond 7 the gains in reliability could be inconsequential. Thus, $\alpha \approx 7$ can serve as a guide for designing memory with improved memory density, while retaining reliability as well as minimizing loss of information.

## 4.7 Detailed Steps

### 4.7.1 Upper Bounds

First, we derive an upper bound for the difference,

$$\int_{-\infty}^{\infty} pf_0(x)\ln(pf_0(x)+(1-p)f_1(x))dx - \int_{-\infty}^{\infty} pf_0(x)\ln(pf_0(x))dx,$$

which is simplified as,

$$\begin{aligned}
& p\int_{-\infty}^{\infty} f_0(x)\ln(1+\frac{(1-p)f_1(x)}{pf_0(x)})dx \\
&= Cp\int_{-\infty}^{\infty} e^{-t^2/2}\ln(1+\frac{(1-p)}{p}e^{2(t-\alpha)\alpha})dt, (t := x+\alpha), \\
&= Cp\int_{(-\infty,\alpha)\cup[3\alpha,\infty)} e^{-t^2/2}\ln(1+\frac{(1-p)}{p}e^{2(t-\alpha)\alpha})dt \\
&+ Cp\int_{\alpha}^{3\alpha} e^{-t^2/2}\ln(1+\frac{(1-p)}{p}e^{2(t-\alpha)\alpha})dt.
\end{aligned} \tag{4.21}$$

Using the logarithmic inequality $\ln(1+x) < x$ for $x > 0$, the first integral in eq. (4.21) satisfies,

$$\begin{aligned}
&Cp \int_{(-\infty,\alpha)\cup[3\alpha,\infty)} e^{-t^2/2} \ln(1 + \frac{(1-p)}{p} e^{2(t-\alpha)\alpha}) dt \\
&< C(1-p) \int_{(-\infty,\alpha)\cup[3\alpha,\infty)} e^{-(t-2\alpha)^2/2} dt, \\
&= 2C(1-p) \int_{\alpha}^{\infty} e^{-u^2/2} du, (u := t - 2\alpha), \\
&< 2C(1-p) \int_{\alpha}^{\infty} u e^{-u^2/2} du, \ (\because u \geq \alpha > 1), \\
&= 2C(1-p) e^{-\alpha^2/2}. \qquad (4.22)
\end{aligned}$$

Moreover, $0 \leq 2(t-\alpha)\alpha \leq 4\alpha^2$ for $t \in [\alpha, 3\alpha)$ and $e^{4\alpha^2} > 1$, using which the last integral in eq. (4.21) satisfies,

$$\begin{aligned}
&Cp \int_{\alpha}^{3\alpha} e^{-t^2/2} \ln(1 + \frac{(1-p)}{p} e^{2(t-\alpha)\alpha}) dt, \\
&\leq Cp \int_{\alpha}^{3\alpha} e^{-t^2/2} \ln(\frac{e^{4\alpha^2}}{p}) dt, \\
&\leq Cp \ln(\frac{e^{4\alpha^2}}{p}) \int_{\alpha}^{\infty} e^{-t^2/2} dt, \\
&\leq Cp \ln(\frac{e^{4\alpha^2}}{p}) e^{-\alpha^2/2}. \qquad (4.23)
\end{aligned}$$

The inequality in eq. (4.7) then follows by combining eq. (4.22) and (4.23) with (4.21).

### 4.7.2 Lower Bounds

We now derive a lower bound for the difference,

$$\begin{aligned}
&\int_{-\infty}^{\infty} p f_0(x) \ln(p f_0(x) + (1-p) f_1(x)) dx - \int_{-\infty}^{\infty} p f_0(x) \ln(p f_0(x)) dx \\
&= \int_{-\infty}^{\infty} p \frac{e^{-x^2/2}}{\sqrt{2\pi}} \ln(1 + \frac{(1-p)}{p} e^{2(x-\alpha)\alpha}) dx.
\end{aligned}$$

Notice that by direct computation of second derivatives, it follows that the function $\varphi(t) = p\ln(1 + \frac{1-p}{p}e^{2(t-\alpha)\alpha})$ is a convex function. Thus, we can express,

$$\int_{-\infty}^{\infty} \frac{e^{-x^2/2}}{\sqrt{2\pi}} p\ln(1 + \frac{(1-p)}{p}e^{2(x-\alpha)\alpha})dx = \mathbb{E}(\varphi(Z)),$$

where, $Z$ is a standard Gaussian random variable. Applying Jensen's inequality [85], we have,

$$\begin{aligned} \mathbb{E}(\varphi(Z)) &\geq \varphi(\mathbb{E}(Z)), \\ &= p\ln(1 + \frac{1-p}{p}e^{-2\alpha^2}). \end{aligned} \tag{4.24}$$

Similarly, one can show that,

$$\begin{aligned} &\int_{-\infty}^{\infty}(1-p)f_1(x)\ln(pf_0(x) + (1-p)f_1(x))dx - \int_{-\infty}^{\infty}(1-p)f_1(x)\ln((1-p)f_1(x))dx \\ &= \int_{-\infty}^{\infty} \frac{e^{-x^2/2}}{\sqrt{2\pi}}(1-p)\ln(1 + \frac{p}{1-p}e^{-2(x+\alpha)\alpha})dx \\ &= \mathbb{E}(\Psi(Z)), \end{aligned}$$

where, $\Psi(t) = (1-p)\ln(1+\frac{p}{1-p}e^{-2(t+\alpha)\alpha})$ is a convex function. Using Jensen's inequality,

$$\begin{aligned} \mathbb{E}(\Psi(Z)) &\geq \Psi(\mathbb{E}(Z)) \\ &= (1-p)\ln(1 + \frac{p}{1-p}e^{-2\alpha^2}). \end{aligned} \tag{4.25}$$

# Chapter 5

# Structure Learning: Linear Systems with Tree Topology

## 5.1 Prologue

In the previous chapters we looked at physical aspects of information processing at a fundamental level. In the next few chapters, we will study the processing of information from diverse sources to unravel interdependencies. We will adopt a networks framework for inference of relationships between observed entities. A highlighting feature is development of algorithms with provable guarantees in the context of linear dynamical systems. Applications will be from power networks and multi agent systems.

In this chapter, we present a method to infer the presence or absence of influences in a collection of dynamically related stochastic processes, where the relationships are bi-directional and the underlying topology is a tree. Our approach combines classical ideas in signal processing and graphical models.

## 5.2 Introduction

Networks underpin a powerful framework for modeling and analysis of large scale dynamical systems. Applications include neuroscience [19], financial markets [87], protein dynamics [88], climate sciences [20] and the power grid [89]. Moreover, networks play an indispensable role in building foundational aspects of control theory [90], statistical inference [91] and optimization theory[92]. The compactness of representation and the capability of unveiling influences, cause-effect relationships and dependencies amongst many variables are some of the key attributes enabled by network based approaches [93, 35]. An essential aspect of many studies is to determine a graphical representation of how multiple sub-systems/agents interact from measured time series data. It is often the case that active manipulation of the system is prohibited or not possible; for example, in financial markets the prices of stocks are available as data but it is not possible (or not allowed) to manipulate the prices. In many cases, the influences between subsystems/ agents is mutual, thus separating source and destination or cause and effect in such cases is not meaningful.

In this chapter, we are concerned with the task of unveiling the network topology that relates multiple linear dynamical systems from temporal data, where it is not possible to excite the system externally. Here, we assume that the underlying network is bi-directed, that is, the influences between agents is mutual and describing cause-effect relationships is not obvious. We further restrict the study to systems where the interaction flow is well characterized by a tree structure.

Learning the structure of a network of static random variables is an active research area in many fields since almost half a century [35, 93, 94, 95, 96]. Recently, there has been growing interest on determining the structure of a network of dynamically related systems. Network reconstruction for a collection of wide sense stationary processes related by linear dynamical systems is approached using inverse of the power spectral density matrix in [38], Wiener filtering in [3, 97] and mutual information in [98]. Our work builds on [3], where it is shown that multivariate Wiener filtering recovers the Markov blanket of each node in the network which includes spurious edges in addition to the true edges in the underlying network. The main contribution of this chapter is a method that eliminates the spurious links to obtain an exact reconstruction of the underlying topology for dynamical systems that have bi-directional interactions with the interaction topology described by a tree. We instantiate the motivation and the results to a power grid. The theory and results are inspired by [2] where aspects of the power grid are modeled in a static framework.

The power grid is a large engineered infrastructural network that has facilitated uninterrupted availability of energy fueling huge technological advances. Power distribution

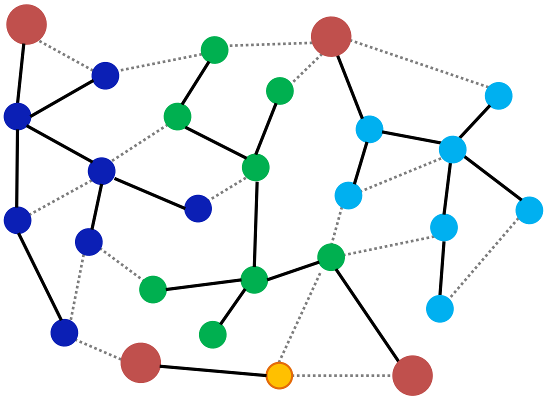

Figure 5.1: Distribution network with roots represented by large red nodes. The operational edges are formed by solid lines (black). Dotted grey lines represent open switches. Non-root nodes within each tree are marked with the same color [2].

systems, which consist of the medium and low-voltage lines that connect the distribution substations to the end-users are structurally characterized by interconnections that can be modeled via a radial topology [99]. The radial topology may be altered over time by changing the operational lines selected from a set of permissible lines, while maintaining the tree structure [100] (see Fig. 5.1). In recent years, the proliferation of smart controllable devices and household generators has led to greater focus on the estimation and control of the distribution system. A critical need, here, is the accurate estimation of the current radial topology that may change over time due to unreported maintenance or faults. The estimation problem is further exacerbated by the historical low-penetration of real-time line meters in the distribution grid. The challenge is being partly met by the use of advanced meters like PMUs (Phase Measurement Units) [101] and distribution micro-PMUs [102] that provide high fidelity measurements of the state of the buses. Prior research directions in this area include learning using inverse covariance matrices [103], trends in voltage variance [100, 104, 105], graphical model learning [2] and maximum likelihood schemes [106]. However, the above indicated studies assume the measured data to be independent samples from a static distribution. Such an assumption may not be accurate as fast sampled (sub-sec sampling) data in the grid arise from the evolution of states that are not static but dynamic. Here, we avoid the static assumption and consider the nodal measurements to arise from the swing dynamics in the power grid [89]. Under the dynamical framework, we apply our analytical development pertinent to bi-directed dynamically related processes, to provably learn the correct radial topology of the grid. We demonstrate the performance of our learning framework on IEEE test dynamic networks.

In the next section we introduce notions from graph theory, which are utilized later, following which we introduce the framework of Linear Dynamic Graphs in Section 5.4. In Section 5.5 the Wiener filtering based network topology reconstruction algorithm is discussed. Then we present results and algorithms to obtain an exact reconstruction for a tree topology in Section 5.6, after which we introduce the swing dynamics of a network of generators and loads in Section 5.7 to illustrate the algorithms presented with examples in Section 5.8. We end with a summary in Section 5.9.

## 5.3 Preliminaries

In this section, basic notions of graph theory that are useful for the subsequent development are recalled [107].

**Definition 1** (Directed and Undirected Graphs). *An undirected graph* $G$ *is a pair* $(V, A)$ *where* $V$ *is a set of vertices or nodes and* $A$ *is a set of edges or arcs, which are unordered subsets* $(i, j), i, j \in V$. *We refer to* $j$ *as the neighbor of* $i$ *and vice versa. If arcs in* $A$ *are ordered, it is called a directed (or oriented) graph.*

**Definition 2** (Topology of a graph). *Given an oriented graph* $G = (V, A)$, *its topology* $top(G)$ *is defined as the undirected graph* $G' = (V, A')$ *that is obtained by removing the orientation on all its edges, and avoiding repetition. For an undirected graph* $G$, $top(G) = G$. *An example of a directed graph is represented in Figure 5.2(a) with its topology in Figure 5.2(b).*

**Definition 3** (Two Hop Neighbor). *In the undirected graph* $top(G) = (V, A^{'})$, $k \in V$ *is a two hop neighbor of* $i \in V$, *if there is a* $j \in V$ *such that* $(i, j) \in A^{'}$ *and* $(j, k) \in A^{'}$.

**Definition 4** (Children, Parents and Kins). *In a directed graph* $G = (V, A)$, *for a node* $j \in V$, *the children of* $j$ *are defined as* $\mathcal{C}_G(j) := \{i | (i, j) \in A\}$ *and the parents of* $j$ *as* $\mathcal{P}_G(j) := \{i | (j, i) \in A\}$. *Kins of* $j \in V$ *are defined as,* $\mathcal{K}_G(j) := \{i | i \neq j$ *and* $i \in \mathcal{C}_G(j) \cup \qquad \cup \mathcal{P}_G(j) \cup \mathcal{P}_G(\mathcal{C}_G(j))\}$.

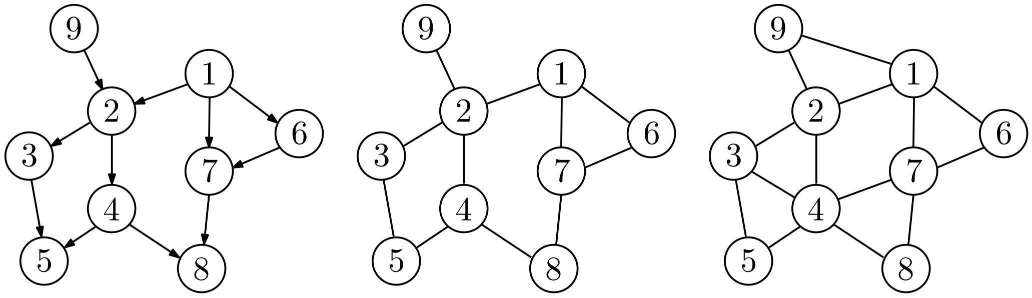

(a) (b) (c)

Figure 5.2: (a) A directed graph, (b) its topology (nodes 2 and 3 are neighbors, 2 and 5 are two hop neighbors) and (c) its kin graph.

Note that the kin relation is a symmetric relationship; $i \in \mathcal{K}_G(j)$ if and only if $j \in \mathcal{K}_G(i)$.

**Definition 5** (Kin-graph)**.** *Given an oriented graph* $G = (V, A)$*, its kin-graph is the undirected graph* $\tilde{G} = (V, \tilde{A})$*, where*

$$\tilde{A} := \{(i, j) | i \in \mathcal{K}_G(j), j \in V\},$$

*and is denoted as* $kin(G) := \tilde{G}$*.*

**Definition 6.** *(Path) A path is a non empty undirected graph* $P = (V, E)$ *with* $V = \{x_0, x_1, \cdots, x_k\}$ *and* $E = \{(x_0, x_1), (x_1, x_2), \cdots, (x_{k-1}, x_k)\}$*. We will denote a path by* $x_0 - x_1 - x_2 - \cdots - x_{k-1} - x_k$*.*

**Definition 7.** *(Cycle) A path* $P$ *of length at least* 2 *with the edge set* $\{(x_0, x_1), (x_1, x_2), \cdots, (x_{k-1}, x_k), (x_k, x$ *is a cycle.*

**Definition 8.** *(Connectedness) A non-empty undirected graph* $G := (V, A)$ *is connected if for any* $a, c \in V$ *there exists a path of the form* $a - b_1 - b_2 - \cdots - b_m - c$ *in* $G$*.*

**Definition 9.** *(Tree) A connected undirected graph without cycles is called a tree. There is a unique path between any two nodes in a tree.*

**Definition 10.** *(Leaf Node/ Non leaf Node of a Tree) In a tree* $\mathcal{T}$*, a node with degree* 1 *is called a leaf node. Nodes with degree greater than* 1 *are called non leaf nodes.*

## 5.4 Linear Dynamic Graphs

In this section we introduce a class of models for the description of a network of JWSS (Jointly Wide Sense Stationary) processes. The node dynamics of the $j-th$ node is given by:

$$x_j = e_j + \sum_{i=1, i\neq j}^{m} \mathcal{H}_{ji}(z)x_i, j = 1, 2, \cdots, m.$$

If an agent $i$ 'influences'another agent $j$, that is, $\mathcal{H}_{ji}(z) \neq 0$, a directed edge is drawn from $i$ to $j$ and a directed graph is obtained. The noise component at each node $e_j$ is assumed to be zero mean WSS and uncorrelated with $\{e_k\}_{k=1,k\neq j}^{m}$.

**Definition 11** (Linear Dynamic Graph [3])**.** *A Linear Dynamic Graph* $\mathcal{G}$ *is defined as a pair* $(\mathbb{H}(z), E)$ *where*

- $E = (e_1 \ ... \ e_m)'$ *is a vector of* $m$ *uncorrelated WSS processes* $\{e_j\}_{j=1}^{m}$*. Thus, the power spectral density matrix of* $E$*,* $\Phi_E(z)$ *is a diagonal matrix of size* $m \times m$*.*
- $\mathbb{H}(z)$ *is a* $m \times m$ *matrix of stable transfer functions in* $\mathcal{F}$ *such that diagonal entries* $\mathbb{H}(j,j)(z) = \boldsymbol{0}$*, for* $j = 1, ..., m$ *and* $\mathbb{H}(j,i)(z) = \mathcal{H}_{ji}(z), i \neq j$ *is the* $(j,i)$ *entry of* $\mathbb{H}(z)$*.*

*A compact expression for the output processes* $\{x_j\}_{j=1}^{m}$ *of the LDG is,*

$$X(k) = \mathbb{H}(z)X(k) + E(k), \tag{5.1}$$

*where* $X = [x_1, \cdots, x_m]'$*. Let* $V := \{x_1, ..., x_m\}$ *and let* $A := \{(x_j, x_i) | \mathcal{H}_{ji}(z) \neq 0\}$*. The pair* $G = (V, A)$ *is the associated directed graph of the LDG. Nodes and edges of a LDG refer to the nodes and edges of the graph* $G$*.*

A LDG $(\mathbb{H}(z), E)$ is well-posed if each entry of $(\mathbb{I}-\mathbb{H}(z))^{-1}$ is stable and topologically detectable if $\Phi_{e_j}(e^{\iota\omega}) > 0$ for any $\omega \in [-\pi, \pi]$ and $j = 1, ..., m$. Here, we focus on a restricted class of LDGs; bi-directed LDGs, which is defined below.

**Definition 12** (bi-directed LDG)**.** *A LDG* $(\mathbb{H}(z), E)$ *whose associated graph is bidirectional is called a bi-directed LDG. Note that in an bi-directed LDG* $\mathcal{H}_{ji}(z) \neq 0$ *almost*

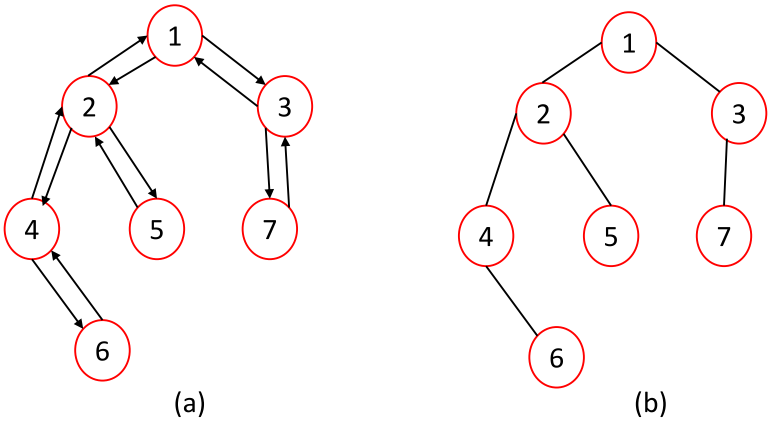

Figure 5.3: (a) A bi-directed LDG and (b) its associated undirected graph.

*surely implies that* $\mathcal{H}_{ij}(z) \neq 0$ *almost surely. The associated graph of a bi-directed LDG could be interpreted as an undirected graph (see Figure 5.3 (b)).*

## 5.5 Learning Kin Graph from data using Wiener Filtering

In this section we present Algorithm 1, which recovers the kin-graph of the underlying LDG from the observed data using multivariate Wiener filtering [3]. The multivariate Wiener filter of estimating $x_j$ from $x_{\bar{j}} := \{x_1, ..., x_{j-1}, x_{j+1}, ..., x_m\}$ is given by, $W_j(z) = [W_{j1}(z) \ ... \ W_{jj-1}(z) \ W_{jj+1}(z) \ \cdots W_{jm}(z)] = \Phi_{x_j x_{\bar{j}}}(z)\Phi^{-1}_{x_{\bar{j}} x_{\bar{j}}}(z)$.

**Algorithm 1** Topology Learning using Wiener Filtering

**Input:** Time series $x_i$ for nodes $i \in \{1, 2, ..., m\}$

**Output:** The kin graph of $\mathcal{T}$, $\mathcal{T}' = (V, \mathcal{E}_{\mathcal{T}'})$.

```
Edge set $\mathcal{E}_{\mathcal{T}'} \leftarrow \{\}$
for all $j \in \{1, 2, ..., m\}$ do
    Compute $W_j(z)$
    for all $i \in \{1, 2, ..., m\}, i \neq j$ do
        if $W_{ji}(z) \neq 0$ then
            $\mathcal{E}_{\mathcal{T}'} \leftarrow \mathcal{E}_{\mathcal{T}'} \cup \{(i, j)\}$
        end if
    end for
end for
```

**Remark 1.** *It is proven in [3] that if $W_{ji}(z) \neq 0$ then $i$ and $j$ are kins. The converse is also true except for pathological cases (see [3]). Thus, we assume our LDG transfer functions are not from the pathological set, thereby enabling Algorithm 1 to recover the kin graph of the LDG. The kin graph obtained after application of Algorithm 1 is an undirected graph, hence, direction of the link cannot be inferred from the output of Algorithm 1. Note that Algorithm 1 is driven by the power spectral density matrices, which can be computed solely from the measured data.*

Consider a bi-directed LDG $(\mathbb{H}(z), E)$ with the associated undirected graph $G = (V, A)$. Let the output of the LDG be given by $X = (x_1, ..., x_m)'$. The Wiener filtering based topology reconstruction leads to an undirected graph $G^{'} = (V, A')$ such that $A' = A \cup$ {edges between two hop neighbors in $G$}.

## 5.6 Network Reconstruction for bi-directed LDGs with Tree topology

In this section we restrict our to attention to bi-directed LDGs whose underlying topology is a tree $\mathcal{T}$. Applying Algorithm 1 described in the previous section to a bi-directed LDG with a tree topology $\mathcal{T} := (V, \mathcal{E}_{\mathcal{T}})$ results in the topology $\mathcal{T}'$ with edge set $\mathcal{E}_{\mathcal{T}'}$

$= \mathcal{E}_{\mathcal{T}} \cup \{(x_i, x_j)|x_i, x_j \in V$ are two hop neighbors in $\mathcal{T}\}$. Note that $\mathcal{E}_T \subset \mathcal{E}_{T'}$. We assume that there exist a path of length at least four in $\mathcal{T}$ and present analytical results leading to algorithms that eliminate the spurious two hop neighbor links in $\mathcal{T}'$. Thus, the generative tree topology $\mathcal{T}$ is exactly determined. For the subsequent developments we will need the notion of d-separation, which is defined below.

**Definition 13** (d-separation [35])**.** *In a directed graph* $(V, A)$*,* $I, J, Z$ *be three disjoint subsets of* $V$*. Then* $dsep(I, Z, J)$ *(to be read as* $Z$*, d-separates* $I$ *and* $J$*) if and only if every path* $p$ *from a node* $i$ *in* $I$ *to a node* $j$ *in* $J$ *satisfies the following conditions*

- *$p$ contains a chain of the form* $\pi_1 \rightarrow z \rightarrow \pi_2$ *or a fork of the form* $\pi_1 \leftarrow z \rightarrow \pi_2$ *such that* $z$ *belongs to the set* $Z$*,*
- *$p$ contains a collider of the form* $\pi_1 \rightarrow x_c \leftarrow \pi_2$ *such that* $x_c$ *or its descendants do not belong to the set* $Z$*,*

*where,* $\pi_1$ *and* $\pi_2$ *are nodes in* $V$*.*

**Theorem 5.6.1.** *Consider a directed graph* $(V, A)$ *such that* $I, J, Z$ *are disjoint and form a partition of* $V$*. Then* $dsep(I, Z, J)$ *if and only if there is no edge of the form*

1. $i \rightarrow j$,
2. $j \rightarrow i$,
3. $i \rightarrow z$ *and* $z \leftarrow j$,

*where,* $i$*,* $j$ *and* $z$ *are nodes in* $I, J$ *and* $Z$ *respectively.*

*Proof.* See [108] for the proof. □

**Theorem 5.6.2.** *In the bi-directed LDG* $(\mathbb{H}(z), E)$ *with a tree topology* $\mathcal{T}$ *and non leaf nodes* $a, b$*,* $a - b$ *is an edge in* $\mathcal{T}$ *if and only if there exist nodes* $c$ *and* $d$ *distinct from* $a$ *and* $b$ *such that* $dsep(c, \{a, b\}, d)$ *holds.*

*Proof.* ($\Rightarrow$) It is given that $a \rightleftharpoons b$ is a link between non leaf nodes $a$ and $b$ in the bi-directed LDG associated with the tree $\mathcal{T}$. As $a$ and $b$ are non leaf nodes, there exist nodes $c$ and $d$ on opposite sides of the edge $a \rightleftharpoons b$ such that $c \rightleftharpoons a \rightleftharpoons b \rightleftharpoons d$ , is a part of the LDG as shown in Figure 5.4 (a), where,

$$\begin{aligned} A := \{v \in V|\ & \text{there exists a path between } v \text{ and } a \\ & \text{that does not contain any element in } \{b, c, d\}\}, \\ B := \{v \in V|\ & \text{there exists a path between } v \text{ and } b \\ & \text{that does not contain any element in } \{a, c, d\}\}, \\ C := \{v \in V|\ & \text{there exists a path between } v \text{ and } c \\ & \text{that does not contain any element in } \{a, b, d\}\}, \text{and} \\ D := \{v \in V|\ & \text{there exists a path between } v \text{ and } a \\ & \text{that does not contain any element in } \{a, b, c\}\}. \end{aligned}$$

*We first establish that* $A \cup B \cup C \cup D \cup \{a, b, c, d\} = V$. Let $v \in V$ be a vertex such that $v \notin A \cup B \cup C \cup D \cup \{a, b, c, d\}$. As the underlying topology is a tree, there is a unique path from $v$ to each vertex in $\{a, b, c, d\}$. Further, as $v$ is outside sets A, B, C, D, it follows from their definition that *the path between* $v$ *to any vertex in* $\{a, b, c, d\}$ *contains at least one more vertex from* $\{a, b, c, d\}$.

Consider the path between $v$ and $a$. Suppose it contains additional vertex $c$ in $\{a, b, c, d\}$. Let the path be $v - \cdots - c - \cdots - a$. Then $v - \cdots - c - \cdots a - b - d$ is a part of $\mathcal{T}$. Clearly, $v - \cdots - c$ (path that connects $v$ and $c$ in $\mathcal{T}$) does not contain $a, b$ or $d$, otherwise $\mathcal{T}$ will have a cycle. Thus, $v \in C$ which is a contradiction. We can arrive at similar contradictions if we assume that the path between $v$ and $a$ contains $b$ or $d$. Hence, our assumption is false and $V = A \cup B \cup C \cup D \cup \{a, b, c, d\}$.

Now we show that there is no paths between any two sets amongst $A$, $B$, $C$ and $D$ in $\mathcal{T}$ that does not involve either nodes $a$ or $b$. Consider node $a'$ in $A$ and $b'$ in $B$. Let the paths from $a'$ to $a$ and $b$ to $b'$ be denoted by $a' - \cdots - a$ and $b - \cdots - b'$ respectively. Consider the path $a' - \cdots - a - b - \cdots - b'$ that includes $a$ and $b$. As $\mathcal{T}$ is a tree, this is the unique path from $a'$ to $b'$. Arguing similarly for any node $a' \in A$ and $b' \in B$, we conclude that no path exists between $A$ and $B$ that does not include nodes $a$ and $b$. Similarly, it can be established that there are no paths between any two sets $A, B, C$

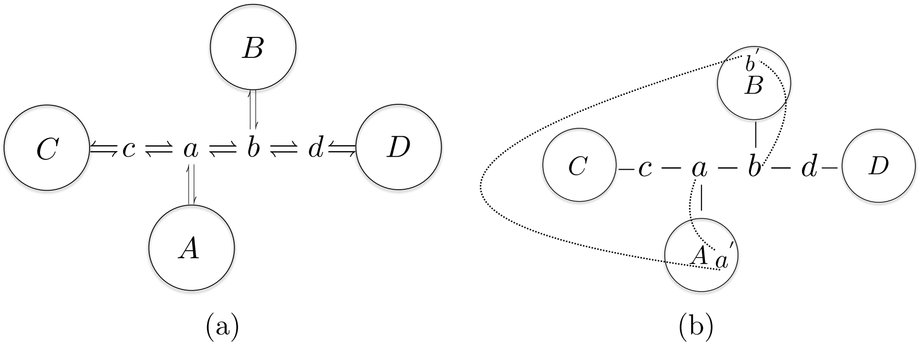

Figure 5.4: (a) The bi-directed LDG associated with $\mathcal{T}$ with the true link $a \rightleftharpoons b$ and nodes $c, d$, and, (b) its topology $\mathcal{T}$ with a hypothetical link between sets $A$ and $B$, as described in the proof below.

and $D$ that does not involve any element from $\{a, b\}$.

Consider $I := A \cup C \cup c$, $J := B \cup D \cup d$ and $Z := \{a, b\}$. Note that $I, J, Z$ form a partition of $V$. In the governing LDG associated with $\mathcal{T}$, it can be shown that there are no links of the form $i \to j$ or $i \leftarrow j$ for any $i$, $j$ in $I$ and $J$ respectively. The proof is similar to the proof mentioned in previous paragraph. Moreover, suppose that there is a link of the form $i \to a \leftarrow j$, for some $i$, $j$ in $I$, $J$ respectively. Then in the underlying topology $\mathcal{T}$ of the LDG, there is a cycle of the form $j - a - b - \pi_1 - \pi_2 - \cdots - \pi_m - j$ in $\mathcal{T}$, where $a, b$ are in $Z$, $b - \pi_1 - \pi_2 - \cdots - \pi_m - j$ is the path between nodes $b$ and $j$ in $\mathcal{T}$. This is not possible as $\mathcal{T}$ is a tree which proves that there is no link of the form $i \to a \leftarrow j$ with $i \in I$ and $j \in J$. Similarly, one can show that there is no link of the form $i \to b \leftarrow j$, for any $i, j$ in $I, J$ respectively.

Thus, applying Theorem 5.6.1 with the partition $I, J, Z$ of $V$ as defined above, we conclude that $dsep(I, Z, J)$, which implies, $dsep(c, \{a, b\}, d)$. This completes the proof in the forward direction.

($\Leftarrow$) Suppose $a - b$ is not an edge in $\mathcal{T}$. Let $p := c - \pi_1 - \pi_2 - s \cdots d$ be the unique path between any two elements $c$ and $d$ in $\mathcal{T}$ that are not from $\{a, b\}$. This path in the associated LDG is of the form $c \rightleftharpoons \pi_1 \rightleftharpoons \pi_2 \rightleftharpoons \cdots \pi_m \rightleftharpoons d$ and is d-separated by non leaf nodes $a$ and $b$.

If $a$ and $b$ do not belong to $\{\pi_1, \cdots, \pi_m\}$. Then $c \to \pi_1 \to \pi_2 \to \cdots \to \pi_m \to d$ is a chain in the LDG associated with $\mathcal{T}$ with no intermediate node between $c$ and $d$ being $a$ or $b$. Thus, $dsep(c, \{a, b\}, d)$ does not hold.

If $a$ belongs to $\{\pi_1, \cdots, \pi_m\}$ but not $b$. Then $c \to \pi_1 \to \pi_2 \to \cdots \to \pi_j \to a \leftarrow \pi_k \to \pi_l \cdots \to \pi_m \to d$ is a path in the LDG associated with $\mathcal{T}$ where $a$ is a collider. It follows from the definition of d-separation that $dsep(c, \{a, b\}, d)$ does not hold. Similarly, $b$ belongs to $\{\pi_1, \cdots, \pi_m\}$ but not $a$.

If both $a$ and $b$ belong to $\{\pi_1, \cdots, \pi_m\}$ then note that as $a - b$ is not in $\mathcal{T}$, the path $p$ corresponds to $c \to \pi_1 \to \pi_2 \to \pi_{i_1} \to a \leftarrow \pi_{i_2} \to \pi_j \to \cdots \to \pi_{k_1} \to b \leftarrow \pi_{k_2} \to \cdots \to \pi_m \to d$ is in the LDG associated with $\mathcal{T}$ where $a$ and $b$ are colliders. It follows from the definition of d-separation that $dsep(c, \{a, b\}, d)$ does not hold.

As all cases have been exhausted we conclude that $dsep(c, \{a, b\}, d)$ is not possible for any nodes $c$ and $d$. This proves the theorem. □

**Theorem 5.6.3.** *If $a - b$ is a edge in $\mathcal{T}$ such that $a$ is a leaf node, then there exist no nodes $c, d$ distinct from $a$ and $b$ such that $dsep(c, \{a, b\}, d)$ holds.*

*Proof.* Suppose there exist nodes $c$ and $d$ distinct from $a$ and $b$ such that $dsep(c, \{a, b\}, d)$. Let $a - b - \pi_{b_1} - \pi_{b_2} - \cdots - \pi_{b_m} - c$ and $c - \pi_{c_1} - \pi_{c_2} - \cdots - \pi_{c_n} - d$ be the unique paths from $a$ to $c$ and $c$ to $d$ in $\mathcal{T}$ respectively. Then, $a - b - \pi_{b_1} - \pi_{b_2} - \cdots - \pi_{b_m} - c - \pi_{c_1} - \pi_{c_2} - \cdots - \pi_{c_n} - d$ is a path between $a$ and $d$, which is unique because $\mathcal{T}$ is a tree.

In the LDG associated with $\mathcal{T}$, there is a chain of the form $c \to \pi_{c_1} \to \cdots \to \pi_{c_n} \to d$ and $dsep(c, \{a, b\}, d)$ implies that either $a$ or $b$ belongs to the set $C := \{\pi_{c_1}, \pi_{c_2}, \cdots, \pi_{c_n}\}$. This is not possible because:

- If $a$ is in $C$ as then $a$ is not a leaf node.
- If $b$ is in $C$, then $a - b - \pi_{c_i} - \cdots - \pi_{c_n} - d$ is another path between $a$ and $d$; distinct from $a - b - \pi_{b_1} - \cdots - \pi_{b_m} - c - \pi_{c_1} - \cdots - \pi_{c_n} - d$(note $c \notin C$), which is a contradiction.

This proves the theorem.

□

**Definition 14** (Moralized Graph)**.** *The graph obtained by connecting all parents having a common child in a directed graph with an undirected edge and then replacing all directed edges with undirected edges is its moralized graph.*

**Remark 2.** *The kin graph obtained using Wiener reconstruction(see Algorithm* 1 *and Remark* 1*) is the moralized graph of the directed graph associated with the LDG.*

**Definition 15** (Ancestors)**.** *In a directed graph $G = (V, A)$, node $j \in V$ is an ancestor of node $k \in V$ if there is a directed sub-graph of $G$ of the form $j \to \pi_1 \to \cdots \to \pi_l \to k$ from $j$ to $k$, where, $\{\pi_1, \cdots, \pi_l\} \in V$.*

**Definition 16** (Ancestral Set)**.** *In a directed graph $(V, A)$, the ancestral set of a node $j$ is the collection of ancestors of $j$ including $j$ itself and is denoted by $an(j)$. Given a collection of nodes $B$ subset of $V$, the ancestral set of $B$, $an(B) := \bigcup\limits_{j \in B} an(j)$.*

**Definition 17** (Ancestral Graph)**.** *Given a directed graph $G = (V, A)$,the ancestral graph of a set of nodes $B$ subset of $V$ is the graph $G_{an(B)} = (an(B), E(an(B)))$ obtained from $G$ by removing all nodes not in $an(B)$.*

**Theorem 5.6.4.** *Let $I, J, Z$ be three disjoint sets of nodes in a directed graph $G = (V, A)$ that can have directed cycles. Then $I, J$ are d-separated by $Z$ in $G$ if and only if they are separated by $Z$ in the moral ancestral graph of $I, J, Z$, that is, $dsep(I, Z, J)$ in $G$ if and only if $sep(I, Z, J)$ in the moralized graph of $G_{an(I \cup Z \cup J)}$, where, $sep(I, Z, J)$ means after removing the nodes $Z$ there is no path between any node in $I$ and any node in $J$.*

*Proof.* See [109, 110] for the proof.

□

**Corollary 5.6.1.** *Consider a bi-directed LDG $(\mathbb{H}(z), E)$ with a topology of a tree $\mathcal{T}$ whose vetrex set be $V$. If $I, J, Z$ are disjoint and form a partition of $V$, then $sep(I, Z, J)$ in the kin graph $\mathcal{T}'$ implies $dsep(I, Z, J)$ in the bi-directed LDG associated with $\mathcal{T}$.*

*Proof.* Since, $I, J, Z$ form a partition, the ancestral graph is same as the generative graph associated with the LDG, then the moralized ancestral graph is the kin graph $\mathcal{T}'$. Using theorem 5.6.4, $sep(I, Z, J)$ in $\mathcal{T}'$ implies $dsep(I, Z, J)$ in the bi-directed LDG. □

Based on Theorem 5.6.2 and Theorem 5.6.3, we present Algorithm 2 which identifies the set of non leaf nodes $V_{nl}$, the set of leaf nodes $V_l$ and eliminates the spurious edges between non leaf node pairs and leaf node pairs to obtain the graph $\overline{\mathcal{T}} := (V, \mathcal{E}_{\overline{\mathcal{T}}})$. Set $\mathcal{E}_{\overline{\mathcal{T}}}$

**Algorithm 2** Elimination of spurious edges involving non leaf nodes in kin graph $\mathcal{T}'$

**Input:** $\mathcal{T}' = (V, \mathcal{E}_{\mathcal{T}'})$
**Output:** $\overline{\mathcal{T}} = (V, \mathcal{E}_{\overline{\mathcal{T}}})$

```
Edge set $\mathcal{E}_{\overline{\mathcal{T}}} \leftarrow \{\}$
for all edge $a - b$ in $\mathcal{E}_{\mathcal{T}'}$ do
    if $Z := \{a, b\}$ there exist $I \neq \{\phi\}$ and $J \neq \{\phi\}$ such that $sep(I, Z, J)$ holds in $\mathcal{T}'$ then
        $V_{nl} \leftarrow V_{nl} \cup \{a, b\}$, $\mathcal{E}_{\overline{\mathcal{T}}} \leftarrow \mathcal{E}_{\overline{\mathcal{T}}} \cup \{(a, b)\}$
    end if
end for
$V_l \leftarrow V - V_{nl}$
for all $a \in V_l, b \in Vnl$ with $(a, b) \in \mathcal{E}_{\mathcal{T}'}$ do
    $\mathcal{E}_{\overline{\mathcal{T}}} \leftarrow \mathcal{E}_{\overline{\mathcal{T}}} \cup \{(a, b)\}$
end for
```

is the edge set obtained after removing each spurious edge between two non-leaf nodes or two leaf nodes from $\mathcal{E}_{\mathcal{T}'}$.

Since the underlying topology is a tree, so each leaf node is connected to only one non leaf node (and no other leaf node) in $\mathcal{T}$. Note that the only spurious edges that exist in $\overline{\mathcal{T}}$ connect a leaf node (set $V_l$) with a non-leaf nodes (in set $V_{nl}$). Next we focus our attention on elimination of such spurious edges between a leaf node and a non-leaf node. Consider leaf node $x_i \in V_l$.Note that the neighbors of $x_i$ in $\overline{\mathcal{T}}$ comprise of non-leaf nodes of its kin-set in $\mathcal{T}$. Wlog assume that the kin set of node $i$ in $\mathcal{T}$ excluding the other leaf nodes is denoted by, $K_{\mathcal{T}}(x_i) = \{x_{j_k}\}_{k=1, j_k \neq i}^{m}$, where each $x_{j_k} \in V_{nl}$.

**Theorem 5.6.5.** *Suppose* $x_i$ *is a leaf node in* $\mathcal{T}$ *such that* $card(K_{\mathcal{T}}(x_i)) = 2$*, that is,* $K_{\mathcal{T}}(x_i) = \{x_{j_1}, x_{j_2}\}$*. If* $x_i - x_{j_1}$ *is the edge in* $\mathcal{T}$ *then* $x_{j_2}$ *is the only non leaf two hop neighbor of* $x_i$ *in the graph* $\overline{\mathcal{T}}$ *with the* $x_i - x_{j_2}$ *edge removed.*

*Proof.* Suppose $x_{j_2}$ is not the only non leaf two hop neighbor of $x_i$ after removing the $x_i - x_{j_2}$ edge in $\overline{\mathcal{T}}$, that is, there exist non leaf node $x_l$ which is a two hop neighbor of $x_i$, implying $\{x_{j_1}, x_{j_2}, x_l\}$ is the kin set of $x_i$, which is a contradiction because $x_i$ has a kin set of cardinality 2. Hence, $x_{j_2}$ is the only non leaf two hop neighbor of $x_i$ in $\mathcal{T}$. □

**Theorem 5.6.6.** *Suppose* $card(K_{\mathcal{T}}(x_i)) \geq 3$*, then* $x_{j_k}$ *is the only common non leaf neighbor of each node in* $K_{\mathcal{T}}(x_i) \cup \{x_i\} \backslash \{x_{j_k}\}$ *in* $\overline{\mathcal{T}}$*, if and only if,* $x_i - x_{j_k}$ *is the edge* *in $\mathcal{T}$ and all other edges connecting $x_i$ to nodes in $K_{\mathcal{T}}(x_i)\backslash x_{j_k}$ are spurious(that is they are not in $\mathcal{T}$).*

*Proof.* ($\Rightarrow$) Suppose $x_i - x_{j_k}$ is not the true edge in $\mathcal{T}$, there exist non leaf node $x_{j_l} \in K_{\mathcal{T}}(x_i)\backslash x_{j_k}$ such that $x_i - x_{j_l}$ is the true edge in $\mathcal{T}$ and all other edges involving $x_i$ and a node from $K_{\mathcal{T}}(x_i)\backslash x_{j_l}$ are spurious links. Then, $x_{j_k}$ is a two hop neighbor of $x_i$ in $\mathcal{T}$ and there exist $x_{j_h}$ in $K_{\mathcal{T}}(x_i)$ distinct from $x_{j_k}$, $x_{j_l}$ such that $x_{j_h}$ is a neighbor of $x_{j_k}$ but not of $x_{j_l}$, otherwise $x_{j_l}$ would satisfy the common neighbor property of $x_{j_k}$. Then, $x_i - x_{j_l} - x_{j_k} - x_{j_h}$ is a path in $\mathcal{T}$, which indicates that $x_{j_h}$ is not a two hop neighbor of $x_i$ in $\mathcal{T}$, implying $x_{j_h}$ is not a kin, which is a contradiction.

($\Leftarrow$) Given $x_i$ is a leaf node with $x_i - x_{j_k}$ being an edge with non leaf node $x_{j_k}$ in $\mathcal{T}$. Let the set $K_{\mathcal{T}}(x_i) = \{x_{j_k}, b_1, b_2, \cdots, b_m\}$, $m \geq 2$. Suppose that $x_{j_k}$ is not the common non leaf neighbor of all nodes in the set $\{b_1, b_2, \cdots, b_m\}$ in $\mathcal{T}$, that is, there exist a $b_k$ such that it is not a neighbor of $x_{j_k}$ in $\mathcal{T}$. The path from $x_i$ to $b_k$ is of the form $x_i - x_j - C - b_k$, where $C$ is non empty path because $x_{j_k}$ is not a neighbor of $b_k$. This implies that $b_k$ is not a two hop neighbor of $x_i$ implying $b_k$ does not belong to the kin set of $x_i$, which is a contradiction. $\square$

Thus, by analyzing the adjacency matrix of the reconstructed topology $\overline{\mathcal{T}}$, spurious links associated with leaf nodes can be eliminated from the set $\overline{\mathcal{T}}$ to recover the edge set associated $\mathcal{T}^*$. In the case of persistently exciting time series data and infinite samples, $\mathcal{T}^* = \mathcal{T}$. The steps to obtain the estimate $\mathcal{T}^*$ of the true topology $\mathcal{T}$ is described in Algorithm 3.

In this section we presented two algorithms, to be applied in the order Algorithm 2 followed by Algorithm 3 which build on the kin graph obtained from Algorithm 1 to recover the exact topology of a bi-directed LDG whose associated graph is a tree. In the next section we present a brief description of the dynamics of a network of generators to motivate examples from the grid for application of the three stage reconstruction procedure.

## 5.7 Applications in Power Systems

In this section we present a model for a radial network of generators in a power system and demonstrate that this model fits the bi-directed LDG framework. The topology of

**Algorithm 3** Elimination of spurious edges involving leaf nodes from $\overline{\mathcal{T}}$ to obtain the estimate $\mathcal{T}^*$

**Input:** $\overline{\mathcal{T}} = (V, \mathcal{E}_{\overline{\mathcal{T}}}), V_l, V_{nl}$
**Output:** $\mathcal{T}^* = (V, \mathcal{E}_{\mathcal{T}^*})$

```
Edge set $\mathcal{E}_{\mathcal{T}} \leftarrow \{\}$
for all $a \in V_l$ do
    if $card(K_{\mathcal{T}}(a)) \geq 3$ then
        determine $b_j \in V_{nl}$ in $K_{\mathcal{T}}(a)$ which is a neighbor of all nodes in $K_{\mathcal{T}}(a) \cup \{a\}$, and,
$\mathcal{E}_{\overline{\mathcal{T}}} \leftarrow \mathcal{E}_{\overline{\mathcal{T}}} - \{(a, b_i)\}_{i \neq j, b_i \in K_{\mathcal{T}}(a)}$
    end if
    if $card(K_{\mathcal{T}}(a)) = 2$ then
        Use Theorem 5.6.5 to determine $x_{j_2}$ and update $\mathcal{E}_{\overline{\mathcal{T}}} \leftarrow \mathcal{E}_{\overline{\mathcal{T}}} - (a, x_{j_2})$
    end if
end for
$\mathcal{E}_{\mathcal{T}^*} \leftarrow \mathcal{E}_{\overline{\mathcal{T}}}$
```

the power network is modeled by a graph $G = (V, A)$ where nodes in $V$ represent buses and edges in $A$ represent transmission lines. Each bus $i$ is associated with a voltage phase angle $\theta_i$ that determines its state. The state dynamics in each node in the system is governed by the following second order equation:

$$m_i \ddot{\theta}_i + d_i \dot{\theta}_i = -p_{e,i} + p_{in,i}, \; i = 1, 2, \cdots, m, \tag{5.2}$$

Here $p_{in,i}$ and $p_{e,i}$ are power input and electrical power output respectively at node $i$. Equation (5.2) describes the swing dynamics for $\theta_i$ with $m_i > 0$ and $d_i > 0$ being the rotational inertia and damping of the generator or rotating load device at node $i$ respectively. The electrical power output is complex valued (AC current). However, for small dynamics, we assume constant voltage magnitudes, purely inductive lines and a small signal approximation [111]. The electrical power output from node $i$ is then given by [89]:

$$p_{e,i} = \sum_{k=1}^{m} b_{ik}(\theta_i - \theta_k), i \in \{1, \cdots, m\}, \tag{5.3}$$

where $b_{i,k} \geq 0$ is the susceptence on the line between nodes $i, k \in A$. Indeed, $b_{ik}(\theta_i - \theta_k)$ represents the power flow from node $i$ to node $k$ in the network. Using $f_i = \dot{\theta}_i$, we can write the following linear state space representation of the power system dynamics

$$\begin{bmatrix} \dot{\theta} \\ \dot{f} \end{bmatrix} = \begin{bmatrix} \mathbf{0} & \mathbf{I} \\ -\mathbf{M}^{-1}\mathbf{L} & -\mathbf{M}^{-1}\mathbf{D} \end{bmatrix} \begin{bmatrix} \theta \\ f \end{bmatrix} + \begin{bmatrix} \mathbf{0} \\ \mathbf{M}^{-1} \end{bmatrix} p_{in}, \tag{5.4}$$

where, $\mathbf{M} = \text{diag}\{m_i\}$, $\mathbf{D} = \text{diag}\{d_i\}$ are diagonal mass and damping matrices of the network, $\mathbf{I} \in \mathbb{R}^{m \times m}$ is the identity matrix , $\mathbf{0} \in \mathbb{R}^{m \times m}$ is the zero matrix. $\mathbf{L} = \mathbf{L}^T \in \mathbb{R}^{m \times m}$ is the network susceptance weighted Laplacian with off-diagonal elements $\mathbf{L}(i,k) = -b_{ik}$ and diagonal elements $\mathbf{L}(i,i) = \sum_{k=1,k\neq i}^{m} b_{ik}$. The state vector $[\theta^T \ f^T]^T \in \mathbb{R}^{2m}$ is comprised of a stacked vector of all angles $\theta \in \mathbb{R}^m$ and frequencies $f \in \mathbb{R}^m$. The vector $p_{in} \in \mathbb{R}^m$ is a collection of power inputs to all nodes in the system. The output equation of the network in discrete time is given by,

$$X(k) = \begin{bmatrix} \mathbf{I} & \mathbf{0} \end{bmatrix} \begin{bmatrix} \theta(k) \\ \omega(k) \end{bmatrix}, \tag{5.5}$$

where the states $\theta$ is measured using nodal PMUs [101]. All state and input variables in (5.4) can be interpreted as deviations from the steady state, $p_{in}$ thus represents ambient deviations from input and modelled as a vector of zero mean uncorrelated WSS processes.

The discretized version of the continuous time network dynamics characterized by (5.4) and (5.5) takes the form $X(k) = \mathbb{H}(z)X(k) + E$, which justifies the modeling of a network of generators as a LDG $(\mathbb{H}(z), E)$. The bi-directedness arises due to the symmetric nature of $\mathbf{L}$. In the next section we apply the three stage topology identification process to *LDGs* of generators governed by the swing equations with the underlying topology being a tree.

## 5.8 Results

We apply the algorithms described in the previous sections to a network of generators whose underlying topology is a tree $\mathcal{T}$. Consider the five node chain of generators as shown in Figure 5.5(I)(a). The dynamics of the chain is simulated using (5.2) and the input $p_{in}$ is considered to be zero mean correlated WSS process. Applying the

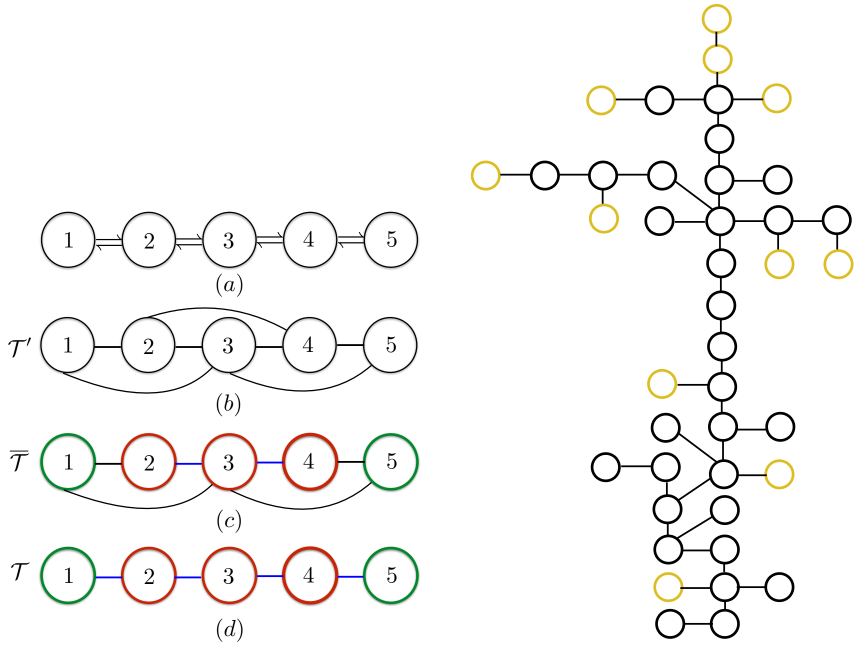

(I) (II)

Figure 5.5: (I) (a) Chain of 5 generators governed by Swing equations (5.2), (b) the kin graph $\mathcal{T}'$ of the chain obtained using Algorithm 1(Wiener filtering), (c) inference of nodes $2, 3, 4$ as non leaf nodes(red), nodes $1, 5$ as leaf nodes(green) and the edges $(2, 3), (3, 4)$ as edges between non leaf nodes(blue) to obtain $\overline{\mathcal{T}}$ by using Algorithm 2 on $\mathcal{T}'$, (d) elimination of spurious edges associated with leaf nodes 1 and 5(black edges in (c)) to obtain $\mathcal{T}$ by using Algorithm 3 on $\overline{\mathcal{T}}$, (II) IEEE 39 bus network topology with the loops removed.

Wiener filtering based network reconstruction procedure (Algorithm 1) on the output data from the chain, results in the kin graph of the chain $\mathcal{T}'$ as shown in Figure 5.5(I)(b). Next we apply Algorithm 2 on the kin graph $\mathcal{T}'$ and obtain $V_{nl} = \{2, 3, 4\}$, $\mathcal{E}_{\mathcal{T}} = \{(2, 3), (3, 4)\}$ and $V_l = \{1, 5\}$. The reduced graph $\overline{\mathcal{T}}$ is shown in Figure 5.5(I)(c). Applying Algorithm 3 on $\overline{\mathcal{T}}$ eliminates the spurious links involving leaf nodes and leads to $\mathcal{E}_{\mathcal{T}^*} = \{(1, 2), (2, 3), (3, 4), (4, 5)\} = \mathcal{E}_{\mathcal{T}}$ as shown in Figure 5.5(I)(d).

Next, we apply our three stage topology identification procedure to the tree shown in Figure 5.5(II) which is derived from the IEEE 39 bus [4, 112] by removing the cycles (four lines removed). There are 11 generator nodes (shown in yellow) and the rest are load nodes. The simulation parameters are available in [112]. We apply the three stage reconstruction procedure on the simulated phase angle information ($10^7$ samples per node) to recover the topology shown in Figure 5.5. The reconstruction is exact and is not shown separately.

## 5.9 Summary

We discussed a Wiener filter and graphical separation based three-stage algorithm to reconstruct the exact topology of a bidirectional radial network of dynamically related WSS processes. The advantage of our approach is that it does not use any prior information about the network except the fact that the underlying topology is a tree. In particular, it is extremely useful in estimating the operating topology of radial power grid using phase angle measurements. We illustrate the proposed algorithm with an example of a 5 node chain and also on a modified tree-version of the IEEE 39 bus test system .

# Chapter 6

# Structure Learning: Linear Systems with Loopy Topology

## 6.1 Prologue

In the previous chapter, we presented an algorithm for exact topology inference for radial bi-directed linear dynamical systems. In particular, the radial topology property was exploited heavily to develop the pruning step to recover the exact topology. In this chapter, we will present a exact topology learning algorithm for linear dynamical systems with a loopy topology, which will exploit the system physics to come up with a pruning step. We demonstrate the efficacy of the method on simulation examples from the power grid and building thermal dynamics as well as experimental data from a network of agents performing distributed computations. Furthermore, we introduce regularizers to improve the performance of the structure learning algorithms in the low sample regime.

## 6.2 Introduction

In [3] the authors present a multivariate Wiener filtering for inferring the network structure of agents that interact via linear dynamical relations. If interactions between the present state of an agent with the present state of another agent exists in the network, then inferred topology is shown to indicate only dependencies and does not provide causal characterization of the inferred edges. However, in the case where the present state of an agent depends only on the strict past of other agents of the network, it is shown that the network structure can be inferred exactly along with causal characterization of the inferred edges. For nonlinear systems with a known bound on the in degree of a node, the authors in [113] use a directed information approach to infer directed graphs. The assumption of strictly causal dynamics is indeed a significant enabling factor to guarantee exact topology inference with edge directions in [3] and [113] . In [114] the authors use a power spectral analysis approach to infer the network topology. For consensus dynamics, a decentralized and distributed topology learning scheme is presented in [115] and [116] respectively. The works summarized above, primarily use a mix of signal processing or optimization schemes or structural restrictions like radial topology [117] to infer the topology. A crucial characteristic is that, none of the above works, utilize any knowledge about the underlying physics of the system toward topology learning.

In this chapter, we focus on topology learning in dynamical physical systems like power networks [118] and thermal dynamic networks [119], where influences between agents, when present, are bi-directional representing a form of coupling and not necessarily a cause effect relationship. In these type of situations, the assumption of strict causality is not valid. We present a new algorithm for exact topology inference, which utilizes both the magnitude and phase response of multivariate Wiener filters for determining the presence/absence of links between two nodes. The main result establishes that the confounding effects of indirect effects of an agent on another can be detected using the phase information in the multivariate Wiener filters that estimate a time-series from the rest. We provide provable guarantees for consistency of the inferred topology with the underlying topology, without resorting to structural restrictions like the topology being radial [120] or bounded in-degree or strictly causal dynamics and without relying on information of system parameters or exogenous inputs. The consistency result holds even in the presence of feedback loops unlike [121], [120]. More importantly, the algorithm is applicable even when the nodal exogenous inputs/noise are colored unlike prior work where assumptions of noise being white are necessary [122]. Of particular focus in our work are physical flow networks like power networks, thermal dynamic networks where we present interesting connections of the phase response in our algorithm with physical conservation laws.

An important application of topology learning is in real time monitoring of a network, which places a requirement of algorithms that can can infer the topology with finite/ limited samples of measurements from each node. The algorithm proposed in this chapter when used with conventional Wiener filtering, is guaranteed to recover the exact topology when sufficient data samples per node are available; here, particularly in the low sample regime the errors in topology inference are high. We introduce group Lasso [123] based regularizers in the Wiener filtering optimization problem and demonstrate that our algorithm when used with regularized version of Wiener filtering provides accurate topology estimation even in the low sample regime. We demonstrate the benefit of using regularizers in topology learning for real time applications. The effectiveness of the algorithms and theory presented is illustrated through simulations on power distribution networks, thermal dynamics of buildings and directed consensus networks. Preliminary work subsumed by this chapter instantiated to various application domains have appeared in [120] for power grid networks, [124] for thermal dynamics of buildings and [125] for consensus networks.

In the next section we present the framework, define the problem of topology learning and provide some motivating examples. Wiener filtering approach for topology inference is summarized in Section 6.4 followed by the derivation of the exact topology learning algorithm and its connections with physical conservation laws in 6.5 In Section 6.6, we illustrate the performance of the learning algorithm on power grid simulations, Energy plus based building simulation and Raspberry Pi based experimental data from consensus dynamics. The chapter is summarized in Section 6.7.

## 6.3 Preliminaries

Suppose $x_i$, $i = 1, \ldots, n$ represent $n$ measured time-series. Further assume that the dynamics generating the time-series $x_i$ satisfy,

$$\sum_{m=1}^{l} a_{m,i} \frac{d^m x_i}{dt^m} = \sum_{j=1, j\neq i}^{n} b_{ij}(x_j(t) - x_i(t)) + p_i(t), \tag{6.1}$$

$i \in \{1, 2, .., n\}$, where, the exogenous forcing $p_i(t)$ is a zero mean wide sense stationary (WSS) process uncorrelated with $p_j(t)$ for $j \neq i$. Note that a linear transformation of $\{p_j(k)\}_{j=1}^n$ results in $\{x_j(k)\}_{j=1}^n$. We assume that the above dynamics is stable. Thus, $\{x_j(k)\}_{j=1}^n$ are a collection of WSS processes and the collection $(\{x_j(k)\}_{j=1}^n, \{p_j(k)\}_{j=1}^n)$ are jointly wide sense stationary processes (JWSS) [126]. Here, $x_i(t) \in \mathbb{R}$ is a state of the system, which is assumed to be measured, and, $a_{m,i} \in \mathbb{R}$, $b_{ij} \in \mathbb{R}_{\geq 0}$. The $z$ transform of the discretization of continuous time dynamics (6.1) is given by,

$$S_i(z)X_i(z) = \sum_{j=1, j\neq i}^{n} b_{ij} X_j(z) + P_i(z), \tag{6.2}$$

where, $S_i(z) = \sum_{m=1}^{l} a_{m,i}((\frac{2(1-z^{-1})}{\Delta t(1+z^{-1})})^m + \sum_{j=1,j\neq i} b_{ij}$, is the $z$ domain operator determined by $x_i$ and its derivatives along with their coefficients in (6.1) and the sampling time $\Delta t$ (using Bilinear transform). Here, $X_i(z)$ is the $z$ transform of $x_i(k)$. Rewriting (6.2) we have,

$$X_i(z) = \sum_{j=1, j\neq i}^{n} H_{ij}(z) X_j(z) + E_i(z) \tag{6.3}$$

where, $H_{ij}(z) = \frac{b_{ij}}{S_i(z)}, E_i(z) = \frac{1}{S_i(z)} P_i(z)$. It can be shown that $e_i(k)$ are uncorrelated with $e_j(k)$ for $j \neq i$, where, $e_i(k)$, is the inverse $z$ transform of $E_i(z)$, and is a zero mean wide sense stationary sequence for all $i = 1, ..., n$. Summarizing, the network dynamics is represented as,

$$\begin{aligned} &X(z) = H(z)X(z) + E(z), \text{ where }, \\ &X(z) = [X_1(z)\ X_2(z)\ ...\ X_n(z)]^T, \\ &E(z) = [E_1(z)\ E_2(z)\ ...\ E_n(z)]^T, H(z)(i,j) = H_{ij}(z). \end{aligned} \tag{6.4}$$

Note that the diagonal entries of the matrix $H(z)$ are 0. For well posedness we assume that $I - H(z)$ is invertible almost everywhere. Next, we associate a graphical representation derived from the transfer function matrix $H(z)$.

**Graphical Representation:** Consider a directed graph $\mathcal{G} = (\mathcal{V}, \mathcal{E})$ with $\mathcal{V} = \{1, ..., n\}$ being the nodes and $\mathcal{E} = \{(i, j) | H_{ij}(z) \neq 0\}$ as the edge set. Each node

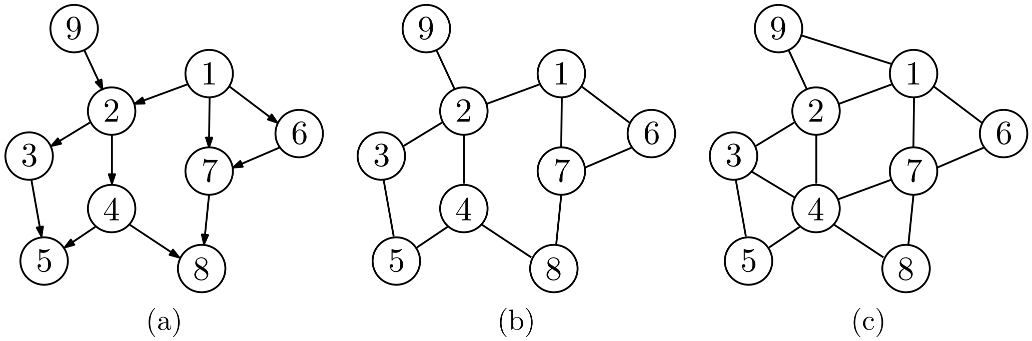

Figure 6.1: A generative graph $\mathcal{G}$ is shown in (a), its topology $\mathcal{G}_T$ in (b), and its moral graph, $\mathcal{G}_M$ in (c) [3].

$i \in \mathcal{V}$ is a representation of the measured time series $x_i(k)$. We refer to the directed graph $\mathcal{G}$ to be the *generative graph* of the measured time series. In the graph $\mathcal{G}$, $(i,j)$ denotes a directed edge from $j$ to $i$ if $H_{ij}(z) \neq 0$, where $j$ is referred as the parent of $i$ and $i$ is referred as the child of $j$. We will refer to nodes having common children as spouses of each other, for example $i \in \mathcal{V}$ and $j \in \mathcal{V}$ are spouses if there exist a node $k \in \mathcal{V}$ such that $H_{ki}(z) \neq 0$ and $H_{kj}(z) \neq 0$ almost surely. Let $C_j, P_j, K_j$ denote the set of nodes consisting of children, parents and spouses of node $j$ in the generative graph $\mathcal{G}$. For illustration, in Fig. 6.1 we show a generative graph, where, nodes 1 and 9 are parents of node 2, while, node 2 is the child of nodes 1 and 9. Here, nodes 1 and 9 are spouses of each other. Given a generative graph $\mathcal{G}$, its *topology* is defined as the undirected graph $\mathcal{G}_T = (\mathcal{V}, \mathcal{E}_T)$ obtained by removing the orientation on all its edges, while avoiding repetition. An example of topology of the generative graph in Fig. 6.1(a) is shown in Fig. 6.1(b). The moral graph, $\mathcal{G}_M = (\mathcal{V}, \mathcal{E}_M)$ of the generative graph $\mathcal{G}$, is defined as the undirected graph obtained by removing the orientation on all its edges, avoiding repetition and adding an undirected edge between spouses. The moral graph of the generative graph in Fig. 6.1(a) is shown in Fig. 6.1(c). Next, we present terminology which will be useful in the subsequent discussion.

**Definition 18.** Path: *A path between two nodes* $x_0, x_k$ *in an undirected graph* $\mathcal{G}_T = (\mathcal{V}, \mathcal{E}_T)$ *is a set of unique nodes* $\{x_0, x_1, \cdots, x_k\} \subseteq \mathcal{V}$ *where* $\{(x_0, x_1), \cdots, (x_{k-1}, x_k)\} \subseteq \mathcal{E}_T$. *We will denote a path by* $x_0 - x_1 - x_2 - \cdots - x_{k-1} - x_k$. *The length of a path is one less than the number of nodes in the path. For example:* $1-2-3-5$ *is a path of length three between node* 1 *and* 5 *in the undirected graph of* Figure 6.1(b).

**Definition 19.** $m$ Hop Neighbor: *In an undirected graph* $\mathcal{G}_T = (\mathcal{V}, \mathcal{E}_T)$*,* $j \in \mathcal{V}$ *is a* $m$ *hop neighbor of* $i \in \mathcal{V}$*, if there is a path of length* $m$ *between* $i$ *and* $j$ *in* $\mathcal{G}_T$*. For example: nodes* 1 *and* 5 *are three hop neighbors in the undirected graph in* Figure 6.1(b)*. If there is a path of length one between* $i$ *and* $j$ *then they are neighbors in* $\mathcal{G}_T$*. The set of* $m$ *hop neighbors of a node* $i \in \mathcal{V}$ *is denoted by* $\mathcal{N}_{i,m}$*.*

There are many systems which satisfy the dynamics represented by (6.1) some of which are discussed below.

1. Consensus dynamics: Distributed decision making methods in multi-agent systems often use the first order consensus protocol, where each agent updates its states based on the difference between other agents' present value and itself, descibed by

$$\frac{dx_i}{dt} = \sum_{j=1}^{n} c_{ij}(x_j - x_i) + p_j, \tag{6.5}$$

   where, $p_j$ denotes the receiver noise for agent $j$ [127]. Inferring, the communication topology of a network of agents in a multi agent system is a relevant objective of a cyber attacker, and appropriate hardware/ software tools need to be designed to avert such attacks. Here, based on the non zero values of $b_{ij}$, the generative graph $\mathcal{G}$ can be obtained.

2. RC networks: Tractable grey box modeling with lumped parameters prove effective for real-time control of buildings. Here *RC* models that assume discretized physical space are employed where every identified zone is represented by a common temperature. Such a lumped parameter model is described by

$$\mathcal{C}_i \frac{dT_i}{dt} = \sum_{j=1}^{n} \frac{T_j - T_i}{R_{ij}} + p_j(t), \tag{6.6}$$

   where, $\mathcal{C}_j > 0$ is the capacitance of zone $j$, $R_{ij} \geq 0$ denotes the thermal resistance between node $i$ and $j$, $p_j$ is the total internal heat generated in zone $j$. In the dynamics above, $R_{ji} = R_{ij}$ and thus in the description corresponding to (6.3) with measured variable $x_i$ identified with temperature $T_i$, the underlying generative dynamics is bi-directional. We consider the problem of inferring the influence topology using temperature sensors ubiquitously at possible zonal locations.

3. Power Grid Network Dynamics: For small disturbances in the power grid, the dynamics of the deviation of voltage phase angle at bus $j$ from the nominal value, denoted by $\theta_j$, is modeled by the following linearized Swing Equation [89],

$$M_i\ddot{\theta}_i + D_i\dot{\theta}_i = \sum_{j=1,\neq i}^{n} c_{ij}(\theta_j - \theta_i) + p_i(t), \tag{6.7}$$

   where, $M_j$ denotes the inertia of the rotating mass, $D_j$ denotes the damping and $p_j(t)$ is the power imbalance injections at the node $j$. Here, $b_{ij}(\theta_j - \theta_i)$ gives the line flow from node $j$ to $i$, where $c_{ij}$ is the susceptance of the line. Under equilibrium conditions power balance is satisfied at each node. Here, $c_{ij} = c_{ji}$, implying, if $H_{ij}(z) \neq 0$ then $H_{ji}(z) \neq 0$ almost surely. Thus, similar to RC networks, the generative graph $\mathcal{G}$ has bi-directional edges. Inferring the topology of a power networks is often the first step to optimize flows and network monitoring for fault detection.

Thermal dynamics and power grid dynamics are such that the physics of the system naturally lead to a bi-directed generative graph, where there is no clear notion of cause and effect among the nodes. Many other physical flow dynamics posses similar characteristics. Here, if $i, j$ are neighbors in the topology $\mathcal{G}_T$, then, $i$ is a parent as well as a child of $j$ in the generative graph. Furthermore, if $i, j$ are two hop neighbors in $\mathcal{G}_T$, then, $i$ and $j$ are spouses in the generative graph. The exact inference of the topology in these physical flow networks is equivalent to exact network inference of the bi-directed generative graph.

## 6.4 Topology Learning

In this chapter, the topology learning problem that we are interested in, involves inferring the underlying topology $\mathcal{G}_T$ of a linear dynamical system described by (6.1) with the generative graph $\mathcal{G}$, based solely on time series measurements $\{x_1(k), ..., x_n(k)\}$ without the knowledge of the system parameters $\{a_{m,i}, b_{ij}\}$ where exogenous inputs $\{p_i\}$ are not measured.

Earlier approaches considered the measurements as *iid* (independent and identically distributed) samples of random variables with a joint distribution; here, states

$\{x_j(k)\}_{j=1}^n$ are modeled as a collection of *iid* samples of a multivariate Gaussian distribution. The framework is relevant when the sampling time $k$ is sufficiently far apart such that $\{x_j(k)\}_{j=1}^n$ satisfy the *iid* sample requirement. Inference of the topology from *iid* samples $\{x_j(k)\}_{j=1}^n$ (also known as Gaussian graphical model inference) is a well studied problem with Graph Lasso (maximum likelihood estimator of the topology from *iid* samples) [37] being a well known approach. However, this framework becomes ineffective for high resolution data where dynamic effects between the measured variables are prominent. The inadequacies of the static framework of random variables is illustrated in [128], where, the authors show that these static approaches are unable to infer the true topology even with large data sets. Moreover, [128] shows that the static approach fails to correctly infer three node cycles present in power networks.

Existing approaches in a dynamical setting with temporally correlated samples, model the exogenous inputs $p_i$ to be Gaussian white noise and independent from $p_j$ for $i \neq j$ [122]. In this work we show that, one can infer the exact topology $\mathcal{G}_T$ of the linear dynamical system described by (6.1), even where exogenous inputs are colored, that is, correlated across time and can detect three node cycles accurately. We begin by recalling the idea of power spectral density.

**Definition 20.** Power Spectral Density(PSD) Matrix: *For a $n$ dimensional collection of WSS time series $x(k) = \{x_1(k), ..., x_n(k)\}^T$, the power spectral density matrix is defined as $\Phi_X(\omega) := \sum_{k=-\infty}^{\infty} \mathbb{E}(x(k)x(0)^T)e^{-\hat{j}\omega k}$, where, $\mathbb{E}(\cdot)$ denotes the expectation operator.*

### 6.4.1 Multivariate Wiener Filtering

Let $v$ and $x_1, ..., x_m$ be a collection of jointly wide sense stationary (JWSS) stochastic processes. Let $x(k) := [x_1(k), ...., x_m(k)]^T$ and $\mathcal{X} := span\{x_1(k), ..., x_m(k)\}_{k=-\infty}^{\infty}$. Consider the following least square optimization problem:

$$\hat{v}(k) := \arg \inf_{q \in \mathcal{X}} \mathbb{E}(v(k) - q)^2. \tag{6.8}$$

If $\Phi_X(\omega) \succ 0$ (that is $\Phi_X(\omega)$ is positive definite) almost surely, then the optimal solution $\hat{v}(k) \in \mathcal{X}$ exists, is unique and is given by

$$\begin{aligned}\hat{V}(z) &= \mathbf{W}(z)X(z), \mathbf{W}(z) = \Phi_{vX}(z)\Phi_X(z)^{-1}\\ &= [W_{v1}(z) \ ... \ W_{vm}(z)]X(z)\\ &= \sum_{j=1}^{m} W_{vj}(z)X_j(z),\end{aligned}$$

where $\mathbf{W}(z) = \Phi_{vX}(z)\Phi_X(z)^{-1}$ is the Wiener filter. Here, $\hat{V}(z)$ is the $z$ transform of $\hat{v}(k)$. Refer [3] for further details. The next result details the properties of Wiener filter for topology inference of linear dynamical systems described by (6.1).

### 6.4.2 Learning the Moral Graph using Multivariate Wiener Filtering

**Theorem 6.4.1.** *Consider the linear dynamical system in* (6.1) *with topology* $\mathcal{G}_T$ *and* $(H(z), E(z))$ *specifying the network dynamics in* (6.4). *The nodal state measurements are given by* $x(k) = [x_1(k), ..., x_n(k)]^T$. *Define the space* $\mathcal{X}_{\bar{j}} = \text{span}\{x_i(k)\}_{i\neq j, k=-\infty}^{k=\infty}$. *The non-causal Multivariate Wiener filter estimate* $\hat{x}_j(k) \in \mathcal{X}_{\bar{j}}$ *of the signal* $x_j(k)$ *is given by,*

$$\hat{X}_j(z) = \sum_{i\neq j, i=1}^{n} W_{ji}(z)X_i(z), \tag{6.9}$$

*where,* $W_{ji}(z) \neq 0$ *implies* $i \in \mathcal{N}_j \cup K_j$ *in* $\mathcal{G}_T$.

*Proof.* The proof follows from the main result of [3], which states that, $W_{ji}(z) \neq 0$ implies that $j$ and $i$ share a children-parent or spouse relationship in the generative graph $\mathcal{G}$. It follows that, in terms of the topology $\mathcal{G}_T$, if $W_{ji}(z) \neq 0$ then $i$ and $j$ are neighbors or spouses. □

**Remark 3.** *The above result does not guarantee that if* $i \in \mathcal{N}_j \cup K_j$, *then* $W_{ji}(z) \neq 0$. *However, such cases are pathological* (see [3]).

Thus the set of children, parents and spouses of each node in the network can be identified using non-zero entries in the corresponding multivariate Wiener filter. The

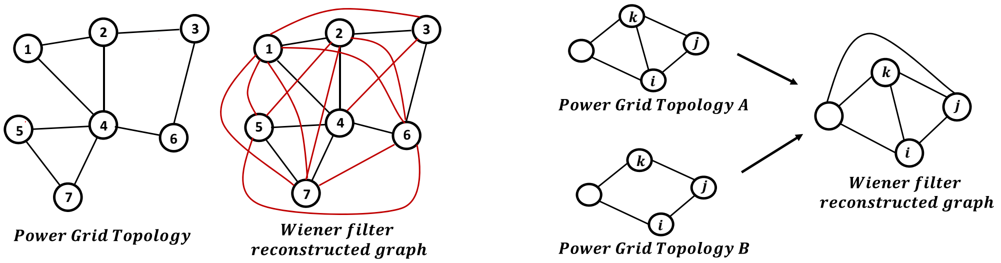

(a) (b)

Figure 6.2: (a) Number of spurious links (red edges) in the Wiener reconstructed graph are comparable with the number of true links (black edges) in the underlying power grid topology (b) Example of two power grid topology which result in the same reconstructed graph of non-trivial Wiener filters

moral graph, $\mathcal{G}_M$, can be obtained by adding a link between nodes with non zero entries in the corresponding multivariate Wiener filter. We summarize the procedure to obtain $\mathcal{G}_M$ from nodal time series measurement in Algorithm 1 below.

**Algorithm 4** Learning Moral Graph using Wiener Filtering

**Input:** samples $x_i(k)$ for nodes $i \in \{1, 2, ..., n\}$ from generative graph $\mathcal{G}$, thresholds $\rho, \tau$, frequency points $\Omega = \{\omega_1, ..., \omega_m\}$ where $\omega_i \in [-\pi, \pi]$

**Output:** Estimate of edges of $\mathcal{G}_M$, $\bar{\mathcal{E}}_M$(for large number of samples per node, $\bar{\mathcal{E}}_M$ coincides with $\mathcal{E}_M$)

```
Edge set $\bar{\mathcal{E}}_M \leftarrow \{\}$
for all $j \in \{1, 2, ..., n\}$ do
    Compute Wiener filter $W_j(e^{\hat{j}\omega}) = [W_{j1}(e^{\hat{j}\omega}) \cdots W_{j,j-1}(e^{\hat{j}\omega}), W_{j,j+1}(e^{\hat{j}\omega}) \cdots W_{jn}(e^{\hat{j}\omega})]$
end for
for all $i, j \in \{1, 2, ..., n\}, i \neq j$ do
    if $\sup_{\omega_i \in \Omega} \|W_{ji}(e^{\hat{j}\omega_i})\| > \rho$ then
        $\bar{\mathcal{E}}_M \leftarrow \bar{\mathcal{E}}_M \cup \{(i, j)\}$
    end if
end for
```

Algorithm 1 results in the moral graph, which has spurious spouse edges apart from the edges present in the topology. For bi-directed generative graphs considered here, the number of spurious links in the moral graph is of the same order as that of true links; here, for every pair of two hop neighbor we get one edge in the moral graph which is not present in the generative graph. Indeed, consider the power grid topology in Fig. 6.2(a) and its moral graph; it is evident that the number of spurious links (links not present in the topology) is substantial. Furthermore, consider the example in Fig. 6.2 (b), where both the topology $A$ and $B$ obtained from the generative graphs of two power grids, following the swing equation dynamics, result in the same reconstructed moral graph using multivariate Wiener filtering. The Wiener filtering based reconstructed edge between $i$ and $k$ in Fig. 6.2 can thus represent a true edge or a spurious edge between spouses. Thus, elimination of spurious edges to recover the actual topology is a non trivial and important task owing to the significant presence of spurious links and presence of many candidate topologies for a given moral graph.

For radial topologies (undirected connected graph with no cycles) associated with bi-directed generative graphs, it is possible to distinguish between true edges between neighbors and spurious two hop neighbor edges in $\mathcal{G}_M$ by using a local graph separation rule as presented in [117]. However for bi-directed generative graphs with topologies having cycles or loops, such graph separation results do not hold in general [128]. In the next section, we present methods that eliminate spurious links obtained from Algorithm 1, for a perfect reconstruction of the generative graph. Here the physics of the dynamics given by (6.1) will prove crucial.

## 6.5 Exact Reconstruction of the generative graph

The following theorem presents an explicit characterization of the contribution of neighbors $\mathcal{N}_j$ and two-hop neighbors $\mathcal{N}_{j,2}$ of node $j$ to the multivariate non causal Wiener filter $\{W_{ji}(z)\}_{i=1,i\neq j}^{n}$.

**Theorem 6.5.1.** *Consider the generative graph* $\mathcal{G} = (\mathcal{V}, \mathcal{E})$ *described by* (6.1)*, with* $x(k) = (x_1(k) \ \cdots \ x_n(k))^T$ *as the output at time instant* $k$*. Let the* $z$ *transform of the multivariate non causal Wiener filtering estimate* $\hat{x}_j(k)$ *of* $x_j(k)$ *be,* $\hat{X}_j(z) = \sum_{i,i\neq j}$

$W_{ji}(z)X_i(z)$. *Then,* $W_{ji}(z) = \hat{C}_{ji}(z) + \hat{P}_{ji}(z) + \hat{K}_{ji}(z)$, *where,*

$$\hat{C}_{ji}(z) = \frac{b_{ij}S_i(z)\Phi_{p_i}^{-1}(z)}{|S_j(z)|^2\Phi_{p_j}^{-1}(z) + \sum_{l\in P_j} b_{lj}^2\Phi_{p_l}^{-1}(z)}, \tag{6.10}$$

$$\hat{P}_{ji}(z) = \frac{b_{ji}S_j^*(z)\Phi_{p_j}^{-1}(z)}{|S_j(z)|^2\Phi_{p_j}^{-1}(z) + \sum_{l\in \mathcal{N}_j} b_{lj}^2\Phi_{p_l}^{-1}(z)}, \text{ and,} \tag{6.11}$$

$$\hat{K}_{ji}(z) = -\frac{\sum_{k\in\mathcal{N}_i\cap\mathcal{N}_j} b_{kj}b_{ki}\Phi_{p_k}^{-1}(z)}{|S_j(z)|^2\Phi_{p_j}^{-1}(z) + \sum_{l\in P_j} b_{lj}^2\Phi_{p_l}^{-1}(z)}. \tag{6.12}$$

*Proof.* It is shown in [3] that, $W_{ji}(z) = \hat{C}_{ji}(z) + \hat{P}_{ji}(z) + \hat{K}_{ji}(z)$, where,

$$\begin{aligned}
\hat{C}_{j*}(z) &= \frac{\Phi_{e_j}(z)H_{*j}^*(z)\Phi_e^{-1}(z)}{1 + |H_{*j}^*(z)\Phi_e^{-1}H_{*j}(z)|\Phi_{e_j}(z)},\\
\hat{P}_{j*}(z) &= (1 - \hat{C}_{j*}(z)H_{*j}(z))H_{j*}(z),\\
\hat{K}_{ji}(z) &= -\hat{C}_{j*}(z)H_{*i}(z),
\end{aligned}$$

with $H_{*j}(z)$ and $H_{j*}(z)$ representing the $j-th$ column and $j-th$ row of the $H(z)$ matrix respectively and $H_{*j}^*(z)$ represents complex conjugate transpose of the vector $H_{*j}(z)$. Here $\hat{C}_{ji}$, $\hat{P}_{ji}$ and $\hat{K}_{ji}$ are contributions of the $i^{th}$ time-series in the estimation of the $j^{th}$ time-series for being the child, parent and spouse of $j$ respectively. Note that $\hat{C}_{jj}(z) = 0$ and $\hat{P}_{jj}(z) = 0$. In the context of a the generative graph $\mathcal{G}$ with dynamics described by (6.1), $\hat{C}_{j*}(z)$ is a $1 \times n$ row of transfer functions described by,

$$\begin{aligned}
\hat{C}_{j*}(z) &= \frac{\Phi_{e_j}(z)H_{*j}^*(z)\Phi_e^{-1}(z)}{1 + |H_{*j}^*(z)\Phi_e^{-1}H_{*j}(z)|\Phi_{e_j}(z)}\\
&= \frac{[H_{1j}^*(z)\Phi_{e_1}^{-1}(z)\ H_{2j}^*(z)\Phi_{e_2}^{-1}(z)\ \cdots\ H_{nj}^*(z)\Phi_{e_n}^{-1}(z)]}{\Phi_{e_j}^{-1}(z) + \sum_{l\in P_j}|H_{lj}(z)|^2\Phi_{e_l}^{-1}(z)}\\
&= \frac{[\frac{b_{1j}}{S_1^*(z)}|S_1(z)|^2\Phi_{p_1}^{-1}(z)\ \cdots\ \frac{b_{nj}}{S_n^*(z)}|S_n(z)|^2\Phi_{p_n}^{-1}(z)]}{|S_j(z)|^2\Phi_{p_j}^{-1}(z) + \sum_{l\in P_j}\frac{b_{lj}^2}{|S_l(z)|^2}|S_l(z)|^2\Phi_{p_l}^{-1}(z)}\\
&= \frac{[b_{1j}S_1(z)\Phi_{p_1}^{-1}(z)\ \cdots\ b_{nj}S_n(z)\Phi_{p_n}^{-1}(z)]}{|S_j(z)|^2\Phi_{p_j}^{-1}(z) + \sum_{l\in P_j} b_{lj}^2\Phi_{p_l}^{-1}(z)}.
\end{aligned}$$

Thus, contribution to $W_{ji}(z)$ due to $i$ being a child of $j$ is given by, $\hat{C}_{ji}(z) = \frac{b_{ij} S_i(z) \Phi_{p_i}^{-1}(z)}{|S_j(z)|^2 \Phi_{p_j}^{-1}(z) + \sum_{l \in P_j} b_{lj}^2 \Phi_{p_l}^{-1}(z)}$. Similarly, contribution from all parents of node $j$ in the generative graph $\mathcal{G}$, $\hat{P}_{j*}(z)$ is a $1 \times n$ row of transfer functions described by,

$$\begin{aligned}
&\hat{P}_{j*}(z) = (1 - \hat{C}_{j*}(z) H_{*j}(z)) H_{j*}(z) \\
&= (1 - \frac{\sum_{l \in N_j} b_{lj}^2 \Phi_{p_l}^{-1}(z)}{|S_j(z)|^2 \Phi_{p_j}^{-1}(z) + \sum_{l \in P_j} b_{lj}^2 \Phi_{p_l}^{-1}(z)}) \\
&[H_{j1}(z) \ \cdots \ H_{jn}(z)] \\
&= \frac{|S_j(z)|^2 \Phi_{p_j}^{-1}(z)}{|S_j(z)|^2 \Phi_{p_j}^{-1}(z) + \sum_{l \in P_j} b_{lj}^2 \Phi_{p_l}^{-1}(z)} \frac{1}{S_j(z)} \\
&[b_{j1}(z) \ \cdots \ b_{jn}(z)] \\
&= \frac{S_j^*(z) \Phi_{p_j}^{-1}(z)}{|S_j(z)|^2 \Phi_{p_j}^{-1}(z) + \sum_{l \in P_j} b_{lj}^2 \Phi_{p_l}^{-1}(z)} [b_{j1}(z) \ \cdots \ b_{jn}(z)].
\end{aligned}$$

Thus, the contribution to $W_{ji}(z)$ due to $i$ being a parent of $j$ is $\hat{P}_{ji}(z) = \frac{b_{ji} S_j^*(z) \Phi_{p_j}^{-1}(z)}{|S_j(z)|^2 \Phi_{p_j}^{-1}(z) + \sum_{l \in P_j} b_{lj}^2 \Phi_{p_l}^{-1}(z)}$. The net contribution to $W_{ji}(z)$ due to $i \in \mathcal{N}_j$, is given by, $\hat{N}_{ji}(z) = \hat{C}_{ji}(z) + \hat{P}_{ji}(z)$. The contribution, $\hat{K}_{ji}$, to $W_{ji}$ for $i$ for being a spouse of $j$ in the generative graph $\mathcal{G}$ with dynamics described by (6.1) is,

$$\begin{aligned}
\hat{K}_{ji}(z) &= -\hat{C}_{j*}(z) H_{*i} \\
&= -\frac{\sum_{k \in C_j \cap C_i} b_{kj} S_k(z) \frac{b_{ki}}{S_k(z)} \Phi_{p_k}^{-1}(z)}{|S_j(z)|^2 \Phi_{p_j}^{-1}(z) + \sum_{l \in P_j} b_{lj}^2 \Phi_{p_l}^{-1}(z)} \\
&= -\frac{\sum_{k \in C_j \cap C_i} b_{kj} b_{ki} \Phi_{p_k}^{-1}(z)}{|S_j(z)|^2 \Phi_{p_j}^{-1}(z) + \sum_{l \in P_j} b_{lj}^2 \Phi_{p_l}^{-1}(z)}.
\end{aligned}$$

This proves the theorem. □

Next, we use the expressions derived in Theorem 6.5.1 to distinguish between true and spurious edges in the moral graph $\mathcal{G}_M$ formed by non-zero entries of multivariate Wiener filter. The next theorem presents a result using the phase response of the non causal Wiener filter for spurious edges corresponding to strict spouse relationships, enabling them to be distinguished from true edges.

**Theorem 6.5.2.** *Consider the generative graph* $\mathcal{G} = (\mathcal{V}, \mathcal{E})$ *described by* (6.1), *with* $x(k) = (x_1(k) \ \cdots \ x_n(k))^T$ *as the output at time instant* $k$. *If* $i$ *and* $j$ *are strict spouses in* $\mathcal{G}$, *that is,* $C_i \cap C_j \neq \phi$ *and* $i \notin \mathcal{N}_j$, $j \notin \mathcal{N}_i$, *then* $\angle(W_{ji}(e^{\hat{j}\omega})) = \pi$ *for all* $\omega \in [-\pi, \pi]$.

*Proof.* As $i \notin \mathcal{N}_j$ and $j \notin \mathcal{N}_i$, $b_{ij} = 0, b_{ji} = 0$. It follows from Theorem 6.5.1 that, $\hat{N}_{ji}(z) = 0$. Since, $i$ and $j$ are spouses, there exist $k \in C_i \cap C_j$ such that $b_{kj} > 0$ and $b_{ki} > 0$, implying $\hat{K}_{ji}(z) \neq 0$. Since, $\hat{K}_{ji}(z)$ is dependent on $\{\Phi_{p_j}(z)\}_{j=1,2,\cdots,n}$, which are positive real numbers for WSS processes, it follows that, $\hat{K}_{ji}(z) < 0$ for all $z \in \mathbb{C}$. Thus,

$$\angle(W_{ji}(e^{\hat{j}\omega})) = \angle(\hat{K}_{ji}(e^{\hat{j}\omega})) = \pi, \text{for all } \omega \in [-\pi, \pi].$$

□

We will use the above theorem to identify spurious edges in the moral graph $\mathcal{G}_M$ to recover the true topology $\mathcal{G}_T$. We now show that the above result does not hold for nodes that are neighbors. The next theorem lists a condition under which $\angle(W_{ji}(e^{\hat{j}\omega})) = \pi$ for all $\omega \in [-\pi, \pi]$ for nodes $i$ and $j$ that are neighbors as well as spouses.

**Theorem 6.5.3.** *Consider the generative graph* $\mathcal{G} = (\mathcal{V}, \mathcal{E})$ *described by* (6.1), *with* $x(k) = (x_1(k) \ \cdots \ x_n(k))^T$ *as the output at time instant* $k$. *Suppose* $i$ *and* $j$ *are such that* $i \in \mathcal{N}_j$, $i \in K_j$. *Then* $\angle(W_{ji}(e^{\hat{j}\omega})) = \pi$ *for all* $\omega \in [-\pi, \pi]$, *if and only if,*

$$\begin{aligned}
&Im(b_{ij} S_i(e^{\hat{j}\omega}) \Phi_{p_i}^{-1}(e^{\hat{j}\omega}) + b_{ji} S_j^*(e^{\hat{j}\omega}) \Phi_{p_j}^{-1}(e^{\hat{j}\omega})) = 0, \\
&Re(b_{ij} S_i(e^{\hat{j}\omega}) \Phi_{p_i}^{-1}(e^{\hat{j}\omega}) + b_{ji} S_j^*(e^{\hat{j}\omega}) \Phi_{p_j}^{-1}(e^{\hat{j}\omega})) - \\
&\sum_{k \in \mathcal{N}_i \cap \mathcal{N}_j} b_{kj} b_{ki} \Phi_{p_k}^{-1}(e^{\hat{j}\omega}) < 0.
\end{aligned}$$

*for all* $\omega \in [-\pi, \pi]$, *where* $Im(z)$ *and* $Re(z)$ *represent imaginary and real parts of the complex number* $z$.

*Proof.* Using (6.10), (6.11) and (6.12),

$$W_{ji}(e^{\hat{j}\omega}) = \frac{b_{ij}S_i(e^{\hat{j}\omega})\Phi_{p_i}^{-1}(e^{\hat{j}\omega}) + b_{ji}S_j^*(e^{\hat{j}\omega})\Phi_{p_j}^{-1}(e^{\hat{j}\omega})}{|S_j(e^{\hat{j}\omega})|^2\Phi_{p_j}^{-1}(e^{\hat{j}\omega}) + \sum_{l\in P_j} b_{lj}^2\Phi_{p_l}^{-1}(e^{\hat{j}\omega})} - \frac{\sum_{k\in\mathcal{N}_i\cap\mathcal{N}_j} b_{kj}b_{ki}\Phi_{p_k}^{-1}(e^{\hat{j}\omega})}{|S_j(e^{\hat{j}\omega})|^2\Phi_{p_j}^{-1}(e^{\hat{j}\omega}) + \sum_{l\in P_j} b_{lj}^2\Phi_{p_l}^{-1}(e^{\hat{j}\omega})} \tag{6.13}$$

The second term in the above expression has no imaginary component and the denominator of both the terms are real.

($\Rightarrow$) Since, $\angle(W_{ji}(e^{\hat{j}\omega})) = \pi$ for all $\omega \in [-\pi, \pi]$ it follows that the conditions hypothesized in the theorem statement hold.

($\Leftarrow$) If the system parameters satisfy the conditions described in the only if part of the theorem statement, it follows from (6.13) that, $\angle(W_{ji}(e^{\hat{j}\omega})) = \pi$ for all $\omega \in [-\pi, \pi]$. □

**Remark 4.** *The conditions presented in the previous theorem are such that for neighbor nodes i and j which are also spouses,* $\angle(W_{ji}(e^{\hat{j}\omega})) = \pi$ *for all* $\omega \in [-\pi, \pi]$, *is pathological because the system parameters have to take a specific set of values for the above mentioned conditions to be true at all frequencies and hence is pathological.*

Finally, the next theorem shows that $\angle(W_{ji}(e^{\hat{j}\omega})) = 0$ for $\omega = 0$ when $i$ and $j$ are neighbors and not spouses.

**Theorem 6.5.4.** *Consider the generative graph* $\mathcal{G} = (\mathcal{V}, \mathcal{E})$ *described by* (6.1), *with* $X(k) = (x_1(k) \ \cdots \ x_n(k))^T$ *as the output at time instant k. Nodes i and j are such that* $i \in \mathcal{N}_j$ *and* $i \notin K_j$. *Then,* $\angle(W_{ji}(e^{\hat{j}\omega}))|_{\omega=0} = 0$.

*Proof.* Since $i \notin K_j$, $\hat{K}_{ji}(z) = 0$. It follows that,

$$\begin{aligned} W_{ji}(e^{\hat{j}\omega}) &= \hat{N}_{ji}(z) \\ &= \frac{b_{ij}S_i(e^{\hat{j}\omega})\Phi_{p_i}^{-1}(e^{\hat{j}\omega}) + b_{ji}S_j^*(e^{\hat{j}\omega})\Phi_{p_j}^{-1}(e^{\hat{j}\omega})}{|S_j(e^{\hat{j}\omega})|^2\Phi_{p_j}^{-1}(e^{\hat{j}\omega}) + \sum_{l\in\mathcal{N}_j} b_{lj}^2\Phi_{p_l}^{-1}(e^{\hat{j}\omega})}. \end{aligned} \tag{6.14}$$

The denominator of the expression on the right hand side of (6.14) is real and positive for all $\omega \in [-\pi, \pi]$. The numerator of the expression on the right hand side of (6.14), $[b_{ij}S_i(e^{\hat{j}\omega})\Phi_{p_i}^{-1}(e^{\hat{j}\omega}) + b_{ij}S_j^*(e^{\hat{j}\omega})\Phi_{p_j}^{-1}(e^{\hat{j}\omega})]_{\omega=0}$ is also real and positive. Thus, $W_{ji}(e^{\hat{j}\omega})|_{\omega=0}$ is real and positive, implying, $\angle(W_{ji}(e^{\hat{j}\omega}))|_{\omega=0} = 0$. □

**Remark 5.** *Theorems 6.5.2, 6.5.3 and 6.5.4 demonstrate that aside from pathological cases, the phase of the Wiener filter* $\angle(W_{ji}(e^{\hat{\jmath}\omega})) = \pi$ *for all* $\omega \in [-\pi, \pi]$ *only when* $i$ *and* $j$ *are* ***not*** *neighbors but are spouses in the generative graph* $\mathcal{G}$*. In other words, aside for the pathological cases, the converse of Theorem 6.5.2 holds and can be used as a criteria to differentiate between true edges and spurious edges in the moral graph* $\mathcal{G}_M$*.*

We now present Algorithm 2 that estimates the topology of the generative graph $\mathcal{G}$ based on time-series of nodal measurements pertaining to dynamics expressed by (6.1). The algorithm consists of two parts. The first part (Steps 2 - 9) determines the multivariate Wiener filter $W_{ji}(z)$ to estimate the moral graph and is same as Algorithm 1. In the next part (Steps 10 - 15), we consider a representative set of frequency points $\Omega$ in the interval $[-\pi, \pi)$ and evaluate the phase angle of the Wiener filters for edges in $\mathcal{E}^w$. If the phase angle is within a pre-defined threshold $\tau$ of $-\pi$, the algorithm designates them as spurious edges (see Theorem 6.5.2) and prunes them from $\mathcal{E}^w$ to produce edge set $\bar{\mathcal{E}}$ of the estimated true topology.

**Algorithm 5** Topology Learning using Wiener Filtering with Pruning Step

**Input:** nodal time samples $x_i(k)$ for nodes $i \in \{1, 2, ..., n\}$ in the generative graph $\mathcal{G}$, thresholds $\rho, \tau$, frequency points $\Omega = \{\omega_1, ..., \omega_m\}$ where $\omega_i \in [-\pi, \pi]$

**Output:** Estimate of Edges $\bar{\mathcal{E}}_T$ in the topology of $\mathcal{G}$. For large samples, $\bar{\mathcal{E}}_T$ coincides with $\mathcal{E}_T$

```
 1: Edge set $\mathcal{E}^w \leftarrow \{\}$
 2: for all $j \in \{1, 2, ..., n\}$ do
 3:     Compute Wiener filter $W_j(e^{\hat{\jmath}\omega}) = [W_{j1}(e^{\hat{\jmath}\omega}) \ \cdots W_{jn}(e^{\hat{\jmath}\omega})]$
 4: end for
 5: for all $i, j \in \{1, 2, ..., n\}, i \neq j$ do
 6:     if $\sup_{\omega_i \in \Omega} \|W_{ji}(e^{\hat{\jmath}\omega_i})\| > \rho$ then
 7:         $\mathcal{E}^w \leftarrow \mathcal{E}^w \cup \{(i, j)\}$
 8:     end if
 9: end for
10: Edge set $\bar{\mathcal{E}}_T \leftarrow \mathcal{E}^w$
11: for all $i, j \in \{1, 2, ..., n\}, i \neq j$ do
12:     if $\pi - \tau \leq |\angle(W_{ji}(e^{\hat{\jmath}\omega_i}))| \leq \pi + \tau, \forall \omega_i \in \Omega$ then
13:         $\bar{\mathcal{E}}_T \leftarrow \bar{\mathcal{E}}_T - \{(i, j)\}$
14:     end if
15: end for
```

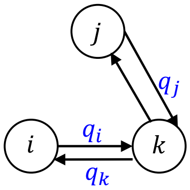

Figure 6.3: A three node system, with the flow on the edge indicated in blue.

**Interpretation of Pruning Step for Physical Flow Networks** Consider nodes $i, j, k$ in a physical flow system like a thermal RC network or a power network, where $k$ is a common neighbor of both $i, j$ but $i, j$ are not neighbors. Let $q_i, q_j$ denote the flow out of node $i, j$ respectively while $q_k$ is the total flow received at node $k$ as shown in Figure 6.3. Here, $q_i, q_j, q_k$ could represent flow of heat, electrical power or even a fluid driven by the difference in temperature, voltage or pressure respectively. These flow variables $q_i, q_j, q_k$ are directly proportional to the nodal state $x_i, x_j, x_k$ respectively. It follows from flow conservation,

$$q_k = q_i + q_j,$$
$$q_i = q_k - q_j,$$

where, a negative correlation is observed between $q_i$ and $q_j$ owing to flow conservation constraint. This translates into an inverse relationship between nodal state variables $x_i$ and $x_j$ leading to phase $\pi$ relationship of the corresponding Wiener filter. Thus, the flow conservation in physical flow networks translates into phase angle being $\pi$ for the associated Wiener filters providing a physics based pruning step in our topology learning algorithm.

## 6.6 Simulation and Experimental Validation

In this section we present simulation and experimental validation of the topology inference algorithm presented in the previous section. First, we present the method employed to compute the Wiener filter using nodal time series measurements and is used in Algorithm 2.

**Wiener filter computation** Let $x_j(k)$ be the nodal time series to be estimated from $\{x_i(k)\}_{i=1, i\neq j}^{m}, k \in \mathbb{Z}$. Consider the following least square optimization problem on the Hilbert space of $\mathcal{L}_2$ random variables,

$$\{h_{ji,o}\} = \arg \inf_{\{h_{ji}\}_{i=1,\dots,m,i\neq j}} \mathbb{E}(x_j(k) - \sum_{i=1,i\neq j}^{m} \sum_{L=-F}^{F} h_{ji}^{L} x_i(k-L))^2, \tag{6.15}$$

where, $h_{ji} = [h_{ji}^{-F}, ..., h_{ji}^{0}, ..., h_{ji}^{F}]$. From the implementation viewpoint, we consider lags up to a finite order $F$ in (6.8). The solution to the above optimization problem is referred as the *finite impulse response multivariate non-causal Wiener filter*) [129], $W_j(z) = [W_{j,1}(z), ..., W_{j,j-1}(z), W_{j,j+1}(z), ..., W_{j,m}(z)]$, where,

$$W_{ji}(z) = \sum_{L=-F}^{F} h_{ji,o}^{L} z^{-L}. \tag{6.16}$$

It is important to note that the multivariate Wiener filter, which is obtained from solving the above optimization problem is determined entirely from the measured time series without any knowledge of system parameters or the statistics of the exogenous inputs. Next, we demonstrate the effectiveness of Algorithm 2 for inference of network structure of agents undergoing linear consensus dynamics.

### 6.6.1 Validation on Consensus Dynamics

Here, the performance of Algorithm 2 in estimating the topology of a network of agents undergoing consensus iterations is demonstrated on a 5 node network depicted in Fig. 6.4(a). We present two set of results, first based on MATLAB simulations, and second based on experimental results on a network of Raspberry Pis. For our simulations, the receiver noise at each node is considered to be white. The trends from the nodal measurement time series are removed using the ‘detrend’ function in MATLAB. The reconstructed topology using Algorithm 1 with $10^7$ samples from each node is shown in Fig. 6.4(c), where, the dashed edges denote the spurious links recovered. Fig. 6.5(a) and Fig. 6.5(b) show the frequency response of Wiener filters between node 2 and all other nodes in Fig. 6.4(a) that are derived using Algorithm 2 with $10^7$ samples for each node. It is clear from Fig. 6.5(a) that the magnitude of the filter $W_{25}$ is small across the frequency

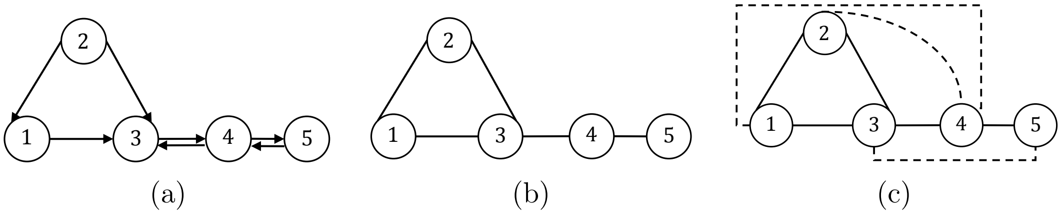

Figure 6.4: (a) Generative graph of 5 node network undergoing consensus dynamics, (b) associated network topology, (c) reconstructed topology of the 5 node network of Fig. 6.4(a) obtained using multivariate Wiener filtering with $10^7$ samples from each node. The dashed links are the spurious links due to spouse relationship.

range and thus it can be concluded that there exist no edge between nodes 2 and 5. Using the pruning step, the absolute values of the phase response of $W_{21}(z), W_{23}(z), W_{24}(z)$ are analyzed as shown in Fig. 6.5(b). Here, the phase of the filter $W_{24}$ remains close to $\pi$ throughout the frequency range. It follows from Theorem 6.5.2 that the edge between 2 and 4 is spurious (phase response being close to $\pi$).

Fig. 6.6(a) shows the experimental setup, which consists of five Raspberry Pi [130] units that interact according to consensus dynamics with the interaction topology described by Fig. 6.4(a). The details of the experimental platform can be found in [131]. The relative error (false negatives and false positives over the number of true edges) percentage of Algorithm 2 with respect to number of samples for simulations as well as experiments is shown in Fig. 6.6(b). It is seen that as the number of samples per node increases, the error decreases.

### 6.6.2 Validation on Power Distribution Network

In this section, we demonstrate the effectiveness of Algorithm 2 on the IEEE 39 bus power distribution network [4] shown in Fig. 6.7(a) with network dynamics as described by (6.7). Here $p_i$ are modeled as filtered white Gaussian noise (colored noise unlike iid Gaussian in [2]) to generate time series data for evaluation of the proposed algorithm. The output at each node is sampled at $0.01s$. Consider the neighbors (green) and two-hop neighbors (red) of node 25 in the IEEE 39 bus system as shown in Fig 6.7. Application of steps 1 to 9 of Algorithm 1 with a threshold $\rho$ of $10^{-5}$ in step 3 and $6.5 \times 10^6$ phase samples per node leads to edges between node 25 and all nodes in Fig. 6.7(b). The absolute values of the phase response of the multivariate Wiener filters for node 25 and

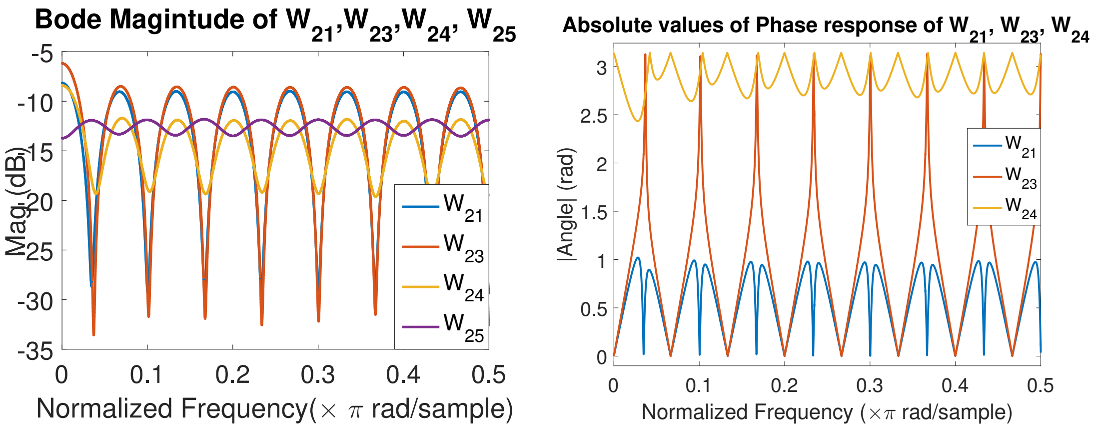

(a) (b)

Figure 6.5: (a) Bode magnitude plot of $W_{21}(z), W_{23}(z), W_{24}(z), W_{25}(z)$, (b) absolute values of phase response of $W_{21}(z)$,$W_{23}(z)$,$W_{24}(z)$, $W_{25}(z)$. $W_{24}(z)$ has a phase response in the vicinity of $\pi$ for all frequencies, hence, is eliminated by the pruning step.

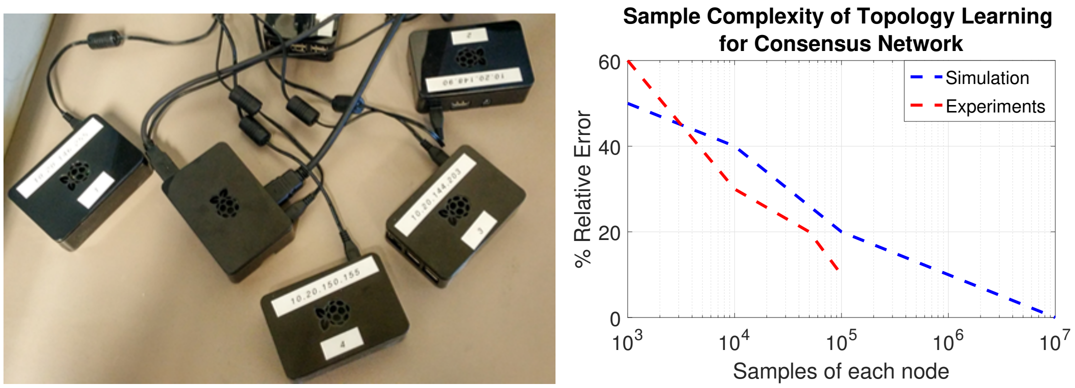

(a) (b)

Figure 6.6: (a) Experimental setup of 5 Raspberry Pi units interacting through wifi according to consensus dynamics with the interaction topology being the undirected graph in Fig. 6.4, (b) error percentage variation with number of samples per node in simulation as well as experiments.

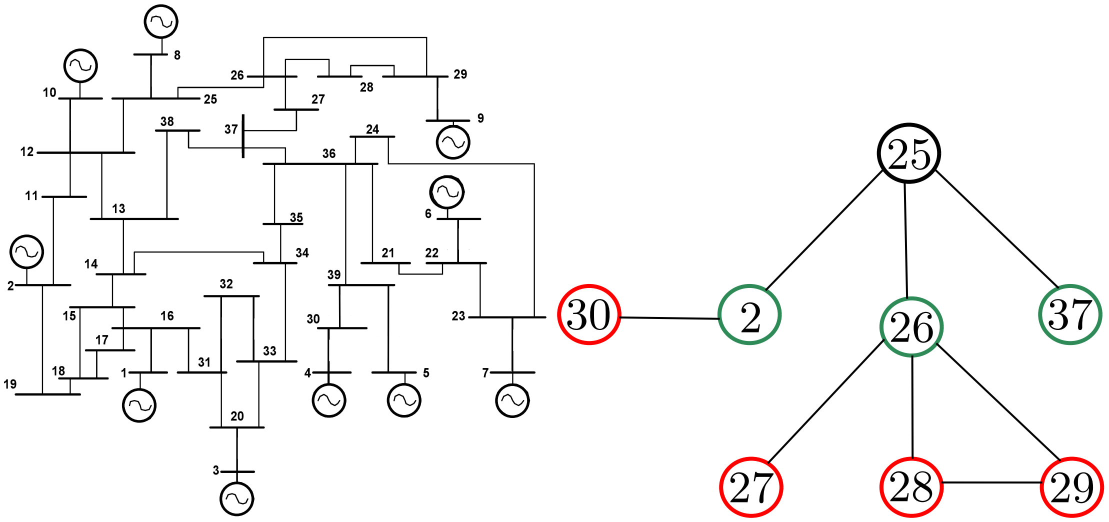

(a) (b)

Figure 6.7: (a) IEEE 39 bus system with generators at 10 buses [4] (b) The neighbors (green nodes) and strict two-hop neighbors (red nodes) of node 25 in the IEEE 39 bus system.

the nodes in its two-hop neighborhood are shown in Fig. 6.8(a). It is seen that the phase response of the Wiener filters corresponding to the nodes two hops away are close to $\pi$ rad, while that of the neighbor nodes start from 0 rad. Thus using the pruning step, all the two-hop neighbors can be removed, recovering the true physical topology. The relative error percentage in topology estimation for the IEEE 39 bus system as a function of sample size is shown in Fig. 6.8(b). The threshold $\rho$ was chosen as $10^{-3}$ while $\tau = 0.2\pi$. In many cases, pruning step eliminated 58% of the total false positive edges obtained after step 9 of Algorithm 2.

### 6.6.3 Comparative study and validation on Thermal Dynamics of Building

In this section, we will estimate the interaction topology amongst zonal temperatures in a building using Algorithm 2 and also highlight the limitations in inference of three node cycles using static approaches. Here, we illustrate that by applying Algorithm 2 to the temperature data of a five zone office building, the true topology is recovered exactly. The building envelope is created in Google SketchUp Make 2017 [132] (see Fig. 6.9) and its RC network model in Fig. 6.9(b). The temperature data is generated using

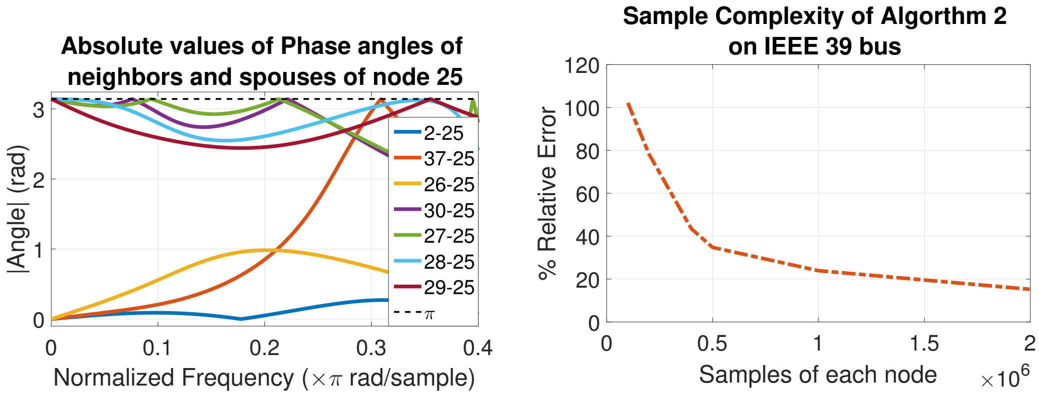

(a) (b)

Figure 6.8: (a) Absolute values of the phase response of the Wiener filters between node 25 and its two-hop neighborhood in the IEEE 39 bus system. The phase response begins from 0 rad for all three neighbors and from $\pi$ for all spouses of node 25. (b) Relative error percentage of Algorithm 2 with samples per node for IEEE 39 bus systems.

EnergyPlus [133]. EnergyPlus solves the nonlinear energy balance equation where the heat transfer coefficients are functions of temperature (See equation 6.19 in Appendix $A$). For more details on EnergyPlus see Section $A$ in Appendix. The building is located in Minneapolis, Minnesota, USA and the weather file used in EnergyPlus is obtained from `https://energyplus.net/weather`. The exogenous inputs to the building are heat gains from lights, electrical equipments and people. For our simulations, we consider the electrical and lighting loads as time-correlated wide sense stationary processes. The correlated inputs are generated by filtering white Gaussian noise through 1D digital filter in MATLAB.

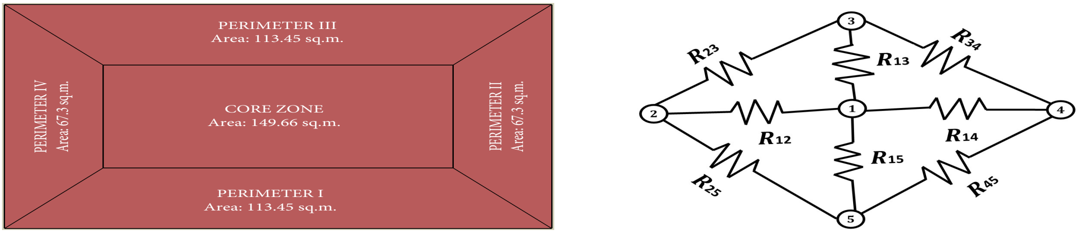

(a) (b)

Figure 6.9: (a) Topview of EnergyPlus building model consisting of 5 zones, where, the height of the building is 3.05 m, (b) Thermal resistor network of the building with thermal capacitance at each node. Node 1 corresponds to core zone and rest of the nodes are referred to as perimeter zones

This temperature data is obtained with one minute granularity and used for topology inference. Here, we perform a comparative study of four algorithms: graphical lasso [37] (random variable framework for Gaussian graphical models, see Appendix $B$ for details), graphical lasso with sign based pruning [103], [128](see Appendix $C$ for details), Algorithm 2 with Wiener filtering computation according to (6.8) and Algorithm 2 with Wiener filtering computation with regularizer (group lasso [134]) as described in (6.17) below. The motivation behind introducing regularization in the Wiener filter optimization problem is to improve the performance of Algorithm 2 in low sample regime. It is seen in Fig. 6.10 that the error in the low sample regime is about 20% for Algorithm 2 with Wiener filters computed using the approach described in (6.15). Regularizers are commonly used to improve the performance of inference algorithms primarily in the high dimensional setting, where, number of nodes are large and samples are limited [36, 37]. Here, we introduce the group lasso regularizer [134] to enforce sparsity and reduce over-fitting in the case of availability of limited number of samples per node.

**Wiener filter with regularization:** Here, we present a method that provides estimates of the optimal Wiener filter which is well suited for scenarios when data-records are short. In order to account for limited samples of measurements at each node, a regularized version of multivariate Wiener filtering in (6.8) is obtained by minimizing the following objective function:

$$\{h_{ji,\gamma}\} = \arg \inf_{\{h_{ji}\}_{i=1,\dots,m,i\neq j}} \mathbb{E}(x_j(k) - \sum_{i=1,i\neq j}^{m} \sum_{L=-F}^{F} h_{ji}^{L} x_i(k-L))^2 + \gamma \sum_{i=1,i\neq j}^{m} \|h_{ji}\|_2. \tag{6.17}$$

Here $\gamma \geq 0$ is the regularization parameter and $h_{ji} := [h_{ji}^{-F}, ..., h_{ji}^{0}, ..., h_{ji}^{F}]$. The regularized Wiener filter is given as,

$$W_{ji}^{\gamma}(z) = \sum_{L=-F}^{F} h_{ji,\gamma}^{L} z^{-L}. \tag{6.18}$$

Using regularized Wiener filters in Algorithm 2, the relative errors for the topology inference of the thermal dynamics of the building described above is shown in Figure

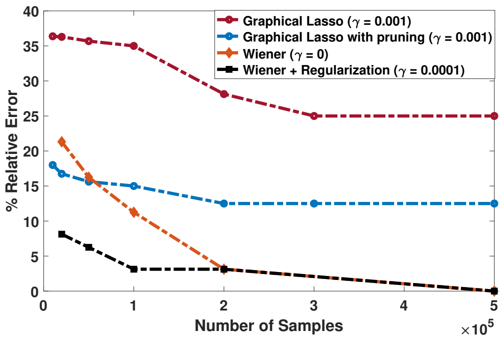

Figure 6.10: Error percentage variation with number of samples per node for Algorithm 2 (with and without regularizers) when inputs are WSS .

6.10. It is seen that in the low sample regime, the error in inference reduces by about half due to use of regularization in Wiener filter computations. The relative error percentage with number of samples for the graphical lasso based algorithms is shown in Fig.6.10. It is seen that, the graphical lasso and graphical lasso with pruning step is unable to recover the exact topology of the underlying RC network, even in the large sample limit. This is a limitation of the random variable framework for networks with three node undirected cycles, which was also highlighted in the introduction of this chapter. However, the time series based approach of Algorithm 2 with and without regularizer have zero error in topology inference in the large sample limit. This is attributed to the ability to analyze the Wiener filters at multiple frequencies in the time series framework as compared to only $\omega = 0$ in the random variable setting, which renders three node undirected cycles unidentifiable.

## 6.7 Summary

In this chapter, we presented an algorithm for exact topology inference of linear dynamical systems with a particular focus on physical flow networks. The flow conservation constraint provides a basis for pruning out spurious spouse links, which crop up in topology learning from time series measurements. We utilized the phase response of multivariate Wiener filters to distinguish between true and spurious edges. The algorithm proposed in this chapter can handle colored noise exogenous inputs, unlike the white noise assumption in some of the recent work on topology inference from time series measurements. Moreover, the proposed algorithm guarantees exact topology inference even in the presence of loops in the network. It is worth noting that, the proposed algorithm does not require any knowledge on statistics of the exogenous inputs or system parameters for topology inference. We believe that using phase response of filters to eliminate spurious links in topology learning can also be extended to other network topology learning approaches like directed information and spectral analysis, as connections of these approaches with the Wiener filtering approach is well understood [98], [3]. The chapter, also highlighted the short comings of state of the art random variables approaches in dealing with networked dynamical systems, particularly in inferring three node cycles and the superiority of the algorithm proposed in such scenarios. We also illustrated the benefit of using regularizers in Wiener filter computations, for obtaining better topology inference performance in the low sample regime. This is particularly important for deploying the proposed algorithm for topology inference from finite size data windows of measurements across the network.

## 6.8 Implementation Details

### Overview of EnergyPlus

EnergyPlus is a building energy simulation engine developed by U.S. Department of Energy. It is an open-source software that can be downloaded at `https://energyplus.net/downloads`. The inputs to the EnergyPlus is a text file with detailed information of the building structure, construction, equipment, location, orientation, weather details along with the occupancy, electrical, lighting schedules. It is a sophisticated simulation tol for thermal analysis of building.

EnergyPlus assumes each thermal zone as a single node and solves the heat balance equations to arrive at the thermal zone temperatures developed in the building and its power consumption. The heat balance equation for a zone [135] is given by:

$$\mathcal{C}_z \frac{dT_z}{dt} = \sum_{i=1}^{N_{sl}} \dot{Q}_i + \sum_{i=1}^{N_{surf}} h_i A_i (T_{si} - T_z) + \sum_{i=1}^{N_{zones}} \dot{m}_i \mathcal{C}_p (T_{zi} - T_z) + \dot{m}_{inf} \mathcal{C}_p (T_\infty - T_z) + \dot{Q}_{sys} \tag{6.19}$$

where, $\mathcal{C}_z \frac{dT_z}{dt}$ is the energy stored in zone air, $\sum_{i=1}^{N_{sl}} \dot{Q}_i$ is internal convective load, $\sum_{i=1}^{N_{surf}} h_i A_i (T_{si} - T_z)$ is surface convective heat transfer, $\sum_{i=1}^{N_{zones}} \dot{m}_i \mathcal{C}_p (T_{zi} - T_z)$ is interzone heat transfer, $\dot{m}_{inf} \mathcal{C}_p (T_\infty - T_z)$ is heat transfer by air infiltration, $\dot{Q}_{sys}$ is air systems output. Note that $h_i$ is a non-linear function of temperatures.

## Graphical Lasso

In the random variable framework [37], consider $N$ independent and identically distributed random variables of a dimension $p$, with mean $\mu$ and covariance $\Sigma$. Let $\Theta = \Sigma^{-1}$, $\rho$ is the regularization parameter and $S$ be the empirical covariance matrix. Then the maximum likelihood estimator of $\Theta$ based on sparsity constraints is given by,

$$\Theta^* = \underset{\Theta}{\operatorname{argmax}}\, logdet\Theta - tr(S\Theta) - \rho \|\Theta\|_1 \tag{6.20}$$

Please see the Algorithm 6 for step by step procedure for topology reconstruction.

**Algorithm 6** Topology Learning using Graphical Lasso

**Input:** nodal time samples $x_i(k)$ for nodes $i \in \{1, 2, ..., n\}$ in the generative graph $\mathcal{G}$, thresholds $\epsilon$

**Output:** Estimate of Edges $\bar{\mathcal{E}}_T$ in the topology of $\mathcal{G}$

```
for all $j \in \{1, 2, ..., n\}$ do
    Compute inverse covariance matrix $\Theta^*$ from 6.20
end for
Edge set $\mathcal{E}^w \leftarrow \{\}$
for all $i, j \in \{1, 2, ..., n\}, i \neq j$ do
    if $|{\Theta^*}_{ij}| > \epsilon$ then
        $\mathcal{E}^w \leftarrow \mathcal{E}^w \cup \{(i, j)\}$
    end if
end for
```

### Graphical Lasso with sign based pruning

After estimating the inverse covariance matrix $\Theta^*$ as described above, the steps for identifying the neighbors and pruning out the spurious links are described here based on the. description in [103], [128].

**Algorithm 7** Topology Learning using Graphical Lasso with sign based pruning

**Input:** nodal time samples $x_i(k)$ for nodes $i \in \{1, 2, ..., n\}$ in the generative graph $\mathcal{G}$, thresholds $\epsilon$

**Output:** Estimate of Edges $\bar{\mathcal{E}}_T$ in the topology of $\mathcal{G}$

```
for all $j \in \{1, 2, ..., n\}$ do
    Compute $\Theta^*$ from 6.20
end for
Edge set $\mathcal{E}^w \leftarrow \{\}$
for all $i, j \in \{1, 2, ..., n\}, i \neq j$ do
    if $|\Theta^*{}_{ij}| > \epsilon$ then
        $\mathcal{E}^w \leftarrow \mathcal{E}^w \cup \{(i, j)\}$
    end if
end for
Edge set $\bar{\mathcal{E}}_T \leftarrow \mathcal{E}^w$
for all $i, j \in \{1, 2, ..., n\}, i \neq j$ do
    if $\Theta^*_{ij} > \epsilon$, then
        $\bar{\mathcal{E}}_T \leftarrow \bar{\mathcal{E}} - \{(i, j)\}$
    end if
end for
```

# Chapter 7

# Structure Learning: Radial Topology with Unobserved Nodes

## 7.1 Prologue

In Chapter 5 and Chapter 6, the topology learning algorithms presented assumed that all the nodes in the network are observed. Here, we present sufficient conditions for sensor placement in bi-directed linear dynamical systems with radial topology as well as an algorithm for exact inference of the topology. The approach presented use a mixture of the algorithms presented in the previous two chapters and is guaranteed to infer the exact topology.

## 7.2 Introduction

Recently, there has been considerable interest in the topology learning for linear dynamical systems from time series measurements. It this regard some of the notable works are [3, 98, 38, 114, 39, 136]. However, these works assume that all nodes in the network are observed or full network observability. Topology reconstruction from passive measurements for a network of linear dynamical systems with unobserved nodes is discussed in [137, 138]. The problem formulation in [137] is focused on directed poly-tree network of linear dynamical systems with unobserved nodes. The framework presented in [138] is restricted to Gaussian stationary time series and does not include consistency of identification results. In this , we present an algorithm which leads to recovering the exact topology of the network under partial observation of the nodes. In particular, we are interested in radial linear dynamical systems, which are characterized by a tree topology with undirected (that is bi-directed) edges between neighbors rather than uni-directed edges. Indeed the directed loops are a part of the framework presented here unlike [137].

Radial linear dynamical systems (RLDS) [117] represent an important class of networks in engineering systems. Among others, RLDS can model dynamics in power distribution systems. An algorithm for exact topology learning for RLDS with all nodes being observed is presented in [117]. We show that for RLDS, under the assumption that unobserved nodes are 'deep into the network'such that their effects are felt through observed nodes, it is possible to recover the underlying interaction topology exactly. In this regard, we build upon topological separation ideas of [117] and phase response properties of [120], to devise an algorithm which provably recovers the exact topology of the RLDS. Our algorithm uses only the time series measurements from the nodes and does not use any knowledge of system parameters as well as the exogenous injections. The efficacy of the algorithm is demonstrated on a 39 bus radial power network with linearized swing dynamics [89].

In the next section, we introduce definitions and notations useful for the subsequent discussion, following which in Section 7.4 we present an algorithm for inference of topology with unobserved nodes using inverse power spectral density. In Section 7.5, we present algorithms for exact topology learning of RLDS with partial observability, followed by results in Section 7.6 and summary in Section 7.7.

## 7.3 Preliminaries

Consider the continuous time linear dynamical system,

$$\sum_{m=1}^{l} a_{m,i} \frac{d^m x_i}{dt^m} = \sum_{j=1, j\neq i}^{n} b_{ij}(x_j(t) - x_i(t)) + p_i(t), \tag{7.1}$$

,$i \in \{1, 2, .., n\}$, where, the exogenous forcing $p_i(t)$ is a zero mean wide sense stationary process uncorrelated with $p_j(t)$ for $j \neq i$. Here, $x_i(t) \in \mathbb{R}$ is a state of the system, $a_{m,i} \in \mathbb{R}$ and $b_{ij} \in \mathbb{R}_{\geq 0}$. Assuming that discrete time samples of the state $x_i$ are available as an output, we discretize the above continuous time dynamics using $z$ transform to obtain,

$$S_i(z)X_i(z) = \sum_{j=1,j\neq i}^{n} b_{ij}X_j(z) + P_i(z),$$

where, $S_i(z)$ is the frequency domain operator determined by the time derivatives of $x_i$. We rewrite the above equation as,

$$X_i(z) = \sum_{j=1,j\neq i}^{m} H_{ij}(z)X_j(z) + E_i(z) \tag{7.2}$$

where, $H_{ij}(z) = \frac{b_{ij}}{S_i(z)}, E_i(z) = \frac{1}{S_i(z)}P_i(z)$. Note that, for $j \neq i$, $e_i(k)$ are uncorrelated with $e_j(k)$ ($e_i$ is the inverse $z$ transform of $E_i(z)$ for all $i = 1, ..., n$) and is a zero mean wide sense stationary sequence. Then, the dynamics of the entire network can be written as,

$$\begin{aligned}
&X(z) = H(z)X(z) + E(z), \text{ where },\\
&X(z) = [X_1(z)\ X_2(z)\ ...\ X_n(z)]^T\\
&E(z) = [E_1(z)\ E_2(z)\ ...\ E_n(z)]^T, H(z)(i,j) = H_{ij}(z).
\end{aligned}$$

We assume that $I - H(z)$ is invertible almost everywhere. Since we are interested in bi-directed linear dynamical system, we make the following assumption in the rest of the chapter.

**Assumption** 1: $H_{ij}(z) \neq 0$ almost surely implies $H_{ji}(z) \neq 0$ almost surely.

Assumption 1 is valid in linearized models of diverse engineering systems around an operating/ equilibrium point. For example - swing dynamics for power systems, lumped parameter RC network models for heat transfer dynamics and consensus networks. Note that the transfer functions $H_{ij}(z)$ and $H_{ji}(z)$ need not be same. We now associate a graphical model to the transfer function matrix $H(z)$.

**Graphical Representation:** Consider a directed graph $\mathcal{G} = (\mathcal{V}, \mathcal{E})$ with $\mathcal{V} = \{1, ..., n\}$ and $\mathcal{E} = \{(i,j)|H_{ij}(z) \neq 0\}$. Each node $i \in \mathcal{V}$ is representative of the measured time series $x_i(k)$. In the graph $\mathcal{G}$, there is a directed edge from $j$ to $i$ if $H_{ij}(z) \neq 0$. It

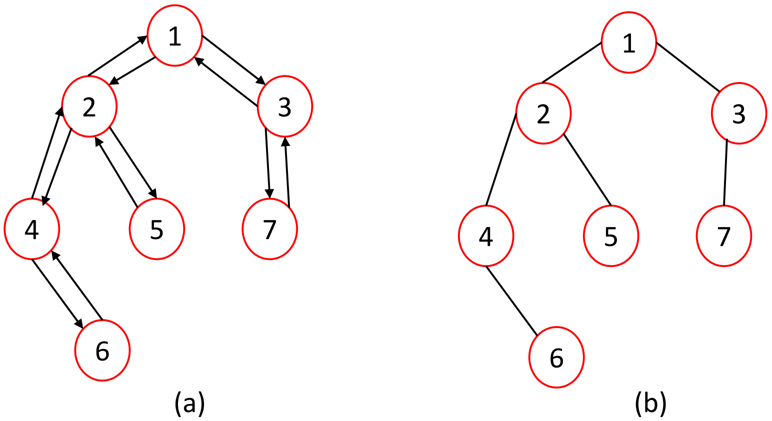

Figure 7.1: (a) Graphical representation of a linear dynamical system where Assumption 1 holds, and (b) its associated topology.

follows from Assumption 1 that, there is a directed edge from $i$ to $j$ as well. Thus $\mathcal{G}$ is a bi-directed graph. We call $\mathcal{G}$ to be the *generative graph* of the measured time series. Given generative graph $\mathcal{G}$, its *topology* is defined as the undirected graph $\mathcal{G}_T = (\mathcal{V}, \mathcal{E}_T)$ obtained by removing the orientation on all its edges, and avoiding repetition. An example of bi-directed generative graph and its topology are shown in Figure 7.1(a) and Figure 7.1(b) respectively. Next, we present terminology for undirected graphs which will be useful in the subsequent discussion.

**Definition 21.** *(Path) A path between two nodes* $x_0, x_k$ *in an undirected graph* $\mathcal{G}_T = (\mathcal{V}, \mathcal{E}_T)$ *is a set of unique nodes* $\{x_0, x_1, \cdots, x_k\} \subseteq \mathcal{V}$ *where* $\{(x_0, x_1), (x_1, x_2), \cdots, (x_{k-1}, x_k)\} \subseteq \mathcal{E}_T$*. We will denote a path by* $x_0 - x_1 - x_2 - \cdots - x_{k-1} - x_k$*. The length of a path is one less than the number of nodes in the path. For example:* $1-2-4-6$ *is a path of length three between node* $1$ *and* $6$ *in the undirected graph of Figure 7.1(b).*

**Definition 22.** *(n Hop Neighbor) In an undirected graph* $\mathcal{G}_T = (\mathcal{V}, \mathcal{E}_T)$*,* $j \in \mathcal{V}$ *is a* $n$ *hop neighbor of* $i \in \mathcal{V}$*, if there is a path of length* $n$ *between* $i$ *and* $j$ *in* $\mathcal{G}_T$*. For example:* $1$ *and* $6$ *are three hop neighbors in the undirected graph in Figure 7.1(b). If* $n = 1$*,* $i$ *and* $j$ *are termed neighbors in* $\mathcal{G}_T$*.*

**Definition 23.** *(Tree) A connected undirected graph without cycles is called a tree. There is a unique path between any two nodes in a tree.*

**Definition 24.** *(Leaf Node/ non-leaf Node of a Tree) In a tree* $\mathcal{T}$*, a node with degree* $1$ *is called a leaf node. Nodes with degree greater than* $1$ *are called non-leaf nodes.*

Next we present the formal definition of a radial linear dynamical system (RLDS).

**Definition 25.** *(Radial Linear Dynamical System) Consider a generative graph* $\mathcal{G}$ *with the associated topology being a tree, which is denoted by* $\mathcal{T}$*. A linear dynamical system with the above properties is referred to as a Radial Linear Dynamical System(RLDS). Figure 7.1(a) shows a RLDS with the corresponding topology* $\mathcal{T}$ *shown in Figure 7.1(b).*

**Definition 26.** *(Power Spectral Density(PSD) Matrix) For a* $n$ *dimensional collection of WSS time series* $x(k) = \{x_1(k), ..., x_n(k)\}^T$*, the power spectral density matrix is defined as* $\Phi_X(\omega) = \sum_{k=-\infty}^{\infty} E(x(k)x(0)^T)e^{-\iota\omega k}$.

In this chapter, we will focus on learning the topology of *radial linear dynamical systems* following Assumption 1. The only information available for topology estimation are time series measurements obtained from a subset of nodes in the system, while certain nodes are unobserved. Our analysis uses properties of inverse power spectral density of linear dynamical systems, which is presented next.

## 7.4 Topology Learning using Inverse PSD

Let $X(z) \in \mathbb{C}^n$ denote the vector of $z$ transform of $n$ nodal states, with $X(z) = [X_o(z)^T, X_h^T(z)]^T$, where, $X_o(z) \in \mathbb{C}^m$ and $X_h(z) \in \mathbb{C}^{n-m}$ are the $z$ transform of the nodal states corresponding to $m$ observed and $n-m$ unobserved nodes respectively. The network dynamics is represented in a compact form as,

$$\begin{bmatrix} X_o(z) \\ X_h(z) \end{bmatrix} = \begin{bmatrix} H_{oo}(z) & H_{oh}(z) \\ H_{ho}(z) & H_{hh}(z) \end{bmatrix} \begin{bmatrix} X_o(z) \\ X_h(z) \end{bmatrix} + \begin{bmatrix} E_o(z) \\ E_h(z) \end{bmatrix}$$

where, $E_o(z)$ and $E_h(z)$ denote the exogenous inputs at the observed and hidden nodes respectively. We assume that the unobserved nodes are not neighbors in $\mathcal{G}_T$, that is, $H_{hh}(z) = \mathbf{0}$. Let $\mathcal{V}_o$ denote the set of observed nodes and $\mathcal{V}_h$ denote the set of unobserved nodes and $\mathcal{V} = \mathcal{V}_o \cup \mathcal{V}_h$.

For notational simplicity we drop the argument $z$ in the discussion below. Let $\Phi_X$ denote the power spectral density matrix of the nodal states, that is,

$$\Phi_X = (I - H)^{-1}\Phi_E(I - H)^{-*}, \tag{7.3}$$

where, $\Phi_E$ is the diagonal matrix of power spectral densities of exogenous inputs and $*$ denotes the Hermittian operator. The objective of the following analysis is to show that inverse of the power spectral density of the states at the observed nodes (denoted by $\Phi_{oo}$) leads to a graph with spurious edges connecting up to four hop neighbors in $\mathcal{G}_T$. Let $J$ denote the inverse power spectral density matrix, that is,

$$\begin{aligned} J = \begin{bmatrix} J_{oo}(z) & J_{oh}(z) \\ J_{ho}(z) & J_{hh}(z) \end{bmatrix} = \Phi_X^{-1} = \begin{bmatrix} \Phi_{oo}(z) & \Phi_{oh}(z) \\ \Phi_{ho}(z) & \Phi_{hh}(z) \end{bmatrix}^{-1}, \\ = (I - H(z))^* \Phi_E^{-1} (I - H(z)). \end{aligned}$$

Using the matrix inversion lemma [139] it follows that,

$$\begin{aligned} \Phi_{oo}^{-1} &= J_{oo} - J_{oh} J_{hh}^{-1} J_{ho} \\ &=: \Gamma + \Delta + \Sigma \end{aligned} \tag{7.4}$$

where,

$$\begin{aligned} \Gamma &= (I - H_{oo}^*) \Phi_{E_o}^{-1} (I - H_{oo}), \\ \Delta &= H_{ho}^* \Phi_{E_h}^{-1} H_{ho}, \text{ and,} \\ \Sigma &= -\Psi^* \Lambda^{-1} \Psi, \text{ where} \\ \Lambda &= H_{oh}^* \Phi_{E_o}^{-1} H_{oh} + \Phi_{E_h}^{-1}, \\ \Psi &= H_{oh}^* \Phi_{E_o}^{-1} (I - H_{oo}) + \Phi_{E_h}^{-1} H_{ho}, \end{aligned} \tag{7.5}$$

**Lemma 7.4.1.** *The following assertions hold*

1. *Suppose $i$ and $j$ are observed nodes and suppose in $\mathcal{G}_T$ (i) there is no path of the form $i - k - j$ with $k$ also observed and (ii) $i - j$ is not present, then $\Gamma(i,j) = 0$.*

2. *If in $\mathcal{G}_T$ there is no path between two observed nodes $i$ and $j$, connected via a single unobserved node, $k_u$, of the form $i - k_u - j$, then $\Delta(i,j) = 0$.*

3. *Suppose in $\mathcal{G}_T$ there is no path between two unobserved nodes with a single intermediate observed node; of the form $k_u - i - k'_u$ where $k_u$ and $k'_u$ are not observed and $i$ is observed, then $\Lambda$ is real and diagonal.*

4. *If in $\mathcal{G}_T$ for $j$ in the observed set of nodes and $k_u$ in the unobserved set of nodes; (i) $j - k_u$ is not present and (ii) there is no path of the form $j - p - k_u$ with $p$ being a observed node, then $\Psi(k,j) = 0$.*

5. *Suppose $\Lambda$ is diagonal, and if in $\mathcal{G}_T$, for observed nodes $i$ and $j$ and unobserved node $k_u$, there are no paths of the form $i - p - k_u$ or $i - k_u$ and $j - p' - k_u$ or $j - k_u$ for any $p$ and $p'$ being observed, then $\Sigma(i, j) = 0$.*

*Proof.* 1) From (7.5),

$$\Gamma \;=\; \Phi_{E_o}^{-1} - \Phi_{E_o}^{-1} H_{oo} - H_{oo}^{*} \Phi_{E_o}^{-1} + H_{oo}^{*} \Phi_{E_o}^{-1} H_{oo}.$$

Note that $\Phi_{E_o}$ is diagonal for $i \neq j$; from which it follows that,

$$\begin{aligned}\Gamma(i,j) \;&=\; -\Phi_{E_o}^{-1}(i,i) H_{oo}(i,j) - \overline{H_{oo}(j,i)} \Phi_{E_o}^{-1}(j,j) \\ &\quad + \textstyle\sum_{k=1}^{m} \overline{H_{oo}(k,i)} H_{oo}(k,j) \Phi_{E_o}^{-1}(k,k).\end{aligned}$$

The first two terms are zero if $i - j$ is not present in $\mathcal{G}_T$ and the third term is zero if a path of the form $i - k - j$ with $k$ being a observed node is not present in $\mathcal{G}_T$.

2) Note that $\Delta = H_{ho}^{*} \Phi_{E_h}^{-1} H_{ho}$ and thus for $i$ and $j$ in the observed set

$$\Delta(i,j) = \sum_{k_u \in \mathcal{V}_h} \overline{H_{ho}(k_u, i)} \Phi_{E_h}^{-1}(k_u, k_u) H_{ho}(k_u, j).$$

Thus if there is no path of the form $i - k_u - j$ where $k_u$ is unobserved, then $\Delta(i,j) = 0$.

3) Suppose $k_u \neq k_u^{'}$ with $k_u$ and $k_u^{'}$ being unobserved nodes. Note that $\Lambda(k_u, k_u^{'}) = [H_{oh}^{*} \Phi_{E_o}^{-1} H_{oh} + \Phi_{E_h}^{-1}](k_u, k_u^{'})$. Thus $\Lambda(k_u, k_u^{'}) = \sum_{i \in \mathcal{V}_o} H_{oh}^{*}(k_u, i) \Phi_{E_o}^{-1}(i,i) H_{oh}(i, k_u^{'}) = \sum_{i \in \mathcal{V}_o} \overline{H_{oh}(i, k_u)} \Phi_{E_o}^{-1}(i,i) H_{oh}(i, k_u^{'})$, which is zero if there is no path of the from $k_u - i - k_u^{'}$ with $i$ being an observed node. Moreover, $\Lambda(k_u, k_u) = \sum_{i \in \mathcal{V}_o} \overline{H_{oh}(i, k_u)} \Phi_{E_o}^{-1}(i,i) H_{oh}(i, k_u) + \Phi_{E_h}^{-1}(k_u, k_u) = \sum_{i \in \mathcal{V}_o} \Phi_{E_o}^{-1}(i,i) |H_{oh}(i, k_u)|^2 + \Phi_{E_h}^{-1}(k_u, k_u) \in \mathbb{R}$.

4) Note that

$$\begin{aligned}&\Psi(k_u, j) \\ &= [H_{oh}^{*} \Phi_{E_o}^{-1}](k_u, j) - [H_{oh}^{*} \Phi_{E_o}^{-1} H_{oo}](k_u, j) + [\Phi_{E_h}^{-1} H_{ho}](k_u, j) \\ &= \overline{H_{oh}(j, k_u)} \Phi_{E_o}^{-1}(j,j) - \sum_{p=1}^{m} \overline{H_{oh}(p, k_u)} \Phi_{E_o}^{-1}(p,p) H_{oo}(p,j) \\ &\quad + \Phi_{E_h}^{-1}(k_u, k_u) H_{ho}(k_u, j). \qquad (7.6)\end{aligned}$$

The first and the last term are zero if $j - k_u$ is not present in $\mathcal{G}_T$ and the second term is zero if there exist no path of the form $j-p-k_u$ in $\mathcal{G}_T$, with $p$ being an observed node.

5) Note that if $\Lambda$ is diagonal, then,

$$\Sigma(i,j) = -\sum_{k_u \in \mathcal{V}_h} \overline{\Psi(k_u,i)}\Lambda^{-1}(k_u,k_u)\Psi(k_u,j),$$

Thus if there is no unobserved node $k_u$ with paths of the form $i-p-k_u$ or $i-k_u$ and $j-p'-k_u$ or $j-k_u$ for any $p$ and $p'$ being observed in $\mathcal{G}_T$, then from 4) of Lemma 7.4.1, $\overline{\Psi(k_u,i)}\Psi(k_u,j) = 0$ for every unobserved node $k_u$, which will imply $\Sigma(i,j) = 0$. This completes the proof. □

We use the above lemma to present a result on topology inference using the inverse of the power spectral density of the observed time series. In this regard we make the following assumption in the rest of the chapter.

**Assumption** 2: The unobserved nodes in topology $\mathcal{G}_T$ are at least four or more hops away from each other.

**Remark 6.** *All the results presented in this chapter assume that the latent nodes are at least three or more hops away from each other except in Theorem 7.5.3, which requires that unobserved nodes are four or more hops away from each other.*

**Theorem 7.4.1.** *Consider a linear dynamical system with topology $\mathcal{G}_T$ such that Assumption 2 holds. Then $\Phi_{oo}^{-1}(i,j)(\omega) \neq 0$ almost surely for $\omega \in [0,2\pi)$, implies that, $i$ and $j$ are within four hops of each other in the graph $\mathcal{G}_T$.*

*Proof.* It follows from (7.4) that, $\Phi_{oo}^{-1}(i,j)(\omega) = \Gamma(i,j)+\Delta(i,j)+\Sigma(i,j)$. Suppose $i$ and $j$ are more than four hops away. We will conclude that $\Phi_{oo}^{-1}(i,j)(\omega) = 0$ almost surely. As two and one hop paths are not present, it follows from 1) and 2) of Lemma 7.4.1 that $\Gamma(i,j) = 0$ and $\Delta(i,j) = 0$ respectively.

From the assumption that unobserved nodes are at least four or more hops away, it follows from 3) of Lemma 7.4.1 that $\Lambda$ is real and diagonal.

Suppose there are paths of the form $i-p-k$ and $j-p'-k$ then $i-p-k-p'-j$ is a four hop path that connects $i$ and $j$, which contradicts that $i$ and $j$ are more than four hops away. Thus, paths of the form $i-p-k$ and $j-p'-k$ cannot be present simultaneously. Similarly, one can show that paths of the form $i-k$ and $j-p^{'}-k$ or

$i-p-k$ and $j-k$ cannot be present as it would imply $i, j$ are three hop neighbors. Thus, from 5) of Lemma 7.4.1, we conclude that $\Sigma(i,j) = 0$. This implies that $\Phi_{oo}^{-1}(i,j) = 0$ and completes the proof. □

**Remark 7.** *Note that the non-zero values in* $\Sigma(i,j)$ *(and subsequently in* $\Phi_{oo}^{-1}(i,j)$*) for three and four hop observed nodes* $i, j$ *result from paths of the form* $i-q-k_u-j, i-k_u-p-j$ *and* $i-q-k_u-p-j$ *in* $\mathcal{G}_T$*, with* $q$ *and* $p$ *being observed neighbors of* $i$ *and* $j$ *respectively and* $k_u$ *being an unobserved node.*

**Remark 8.** *Note that the system transfer functions have to take very specific forms in order for* $\Gamma(i,j)+\Delta(i,j)+\Sigma(i,j)$ *to be zero even though* $i, j$ *are either neighbors or two hop neighbors. Thus, except for these pathological cases, if* $i$ *and* $j$ *are neighbors, two hop neighbors (with the common neighbor being observed or unobserved)* $\Phi_{oo}^{-1}(i,j) \neq 0$ *almost surely. Furthermore, for* $i, j$ *being three or four hop neighbors,* $\Gamma(i,j) = 0$ *and* $\Delta(i,j) = 0$*. The second term of* $\Psi(i,j)$ *is a contributor to three/ four hop contributions and is non zero in a large number of applications. For example: suppose that* $b_{ij} \geq 0, a_{m,i} \geq 0$ *for all* $i, j$ *in (7.1) (which is true for engineering networks like power distribution systems, RC networks etc.); then it is not possible that* $\Phi_{oo}^{-1}(i,j) = 0$ *if* $i$ *and* $j$ *are three or four hop neighbors in* $\mathcal{G}_T$*. We assume that the systems of interest do not belong to the small set of pathological cases.*

If we form a graph $\mathcal{G}_m$ using the non-zero values in $\Phi_{oo}^{-1}(i,j)(\omega)$ as the adjacency matrix, we obtain all links up to four hop neighbors in $\mathcal{G}_T$. This is summarized as Algorithm 1 and is the first step in our topology learning scheme. The next objective is to identify the true links as well as eliminate the spurious links and identify the location of the unobserved nodes in $\mathcal{G}_m$ obtained from Algorithm 1. Note that Theorem 7.4.1 does not depend on the linear dynamical system being radial. However in the subsequent analysis, we will explicitly use the fact that $\mathcal{G}_T = \mathcal{T}$ is a RLDS.

## 7.5 Exact Topology Recovery in Radial Linear Dynamical Systems

To recover the exact topology of the radial linear dynamical system (RLDS) there the two tasks: one is to determine the set of true edges in the graph obtained from Algorithm

**Algorithm 8** Topology Learning using Power Spectrum

```
Input: Time series $x_i(k)$ from observed nodes
Output: $\mathcal{G}_m = (\mathcal{V}_o, \mathcal{E}_{\mathcal{G}_m})$.
Edge set $\mathcal{E}_{\mathcal{G}_m} \leftarrow \{\}$
Compute $\Phi_{oo}^{-1}(\omega)$
for all $i \in \{1, 2, ..., m\}, i \neq j$ do
    if $\Phi_{oo}^{-1}(j,i)(\omega) \neq 0$ then
        $\mathcal{E}_{\mathcal{G}_m} \leftarrow \mathcal{E}_{\mathcal{G}_m} \cup \{(i,j)\}$
    end if
end for
```

1 and the next is to determine the location of the unobserved nodes. We accomplish these tasks in the following two subsections.

### 7.5.1 True Edge Discovery between Observed Nodes

Consider a RLDS with a tree topology $\mathcal{T}$. Let the unobserved nodes be at least four or more hops away from each other as per Assumption 2. The graph $\mathcal{T}_m$ obtained using Algorithm 1 has edges between observed nodes that are up to four hops away in $\mathcal{T}$. The objective of this section is to design an algorithm to identify the true links as well as eliminate the spurious links and detect the location of the missing nodes in $\mathcal{T}_m$ to recover $\mathcal{T}$ from $\mathcal{T}_m$. In this regard, we introduce the following assumption and the notion of separation in graphs.

**Assumption 3:** Each unobserved node is at least three hops away from all leaf nodes in $\mathcal{T}$.

Based on the above assumption, it is clear that all leaf nodes in $\mathcal{T}$ are observed nodes. Put differently, each unobserved node is buried deep into the network so that their effect is 'felt' at multiple observed nodes.

**Definition 27.** *(Separation in Graph) In an undirected graph $\mathcal{U}$, the set of nodes $Z$ is said to separate the path between nodes $i$ and $j$, if there exist no path between $i$ and $j$ in $\mathcal{U}$ after removing the set of nodes $Z$. We will use the notation sep$(i, Z, j)$, which is to be read as $Z$ separates the path between $i$ and $j$ in $\mathcal{U}$. For example, in Figure 7.1(b) sep$(1, \{2, 4\}, 6)$ holds.*

Next, we present a result, which enables us to categorize true and spurious edges between observed non-leaf nodes in $\mathcal{T}_m$. The proofs of the results presented below are omitted due to space restrictions.

**Theorem 7.5.1.** *Consider a RLDS with a tree topology $\mathcal{T}$ such that Assumption 2 and 3 hold. Let $\mathcal{T}_m$ be such that there are links between any two observed nodes that are within four hops in the underlying topology $\mathcal{T}$ (that is no link up to four hops is undetected as discussed in Remark 8). There exist observed nodes $c, d$ distinct from observed nodes $a, b$ such that $sep(c, \{a, b\}, d)$ holds in $\mathcal{T}_m$ if and only if $a - b$ is an edge (and thus a true edge) in $\mathcal{T}$ and $a, b$ are non-leaf nodes.*

**Remark 9.** *The above theorem provides a topological test on $\mathcal{T}_m$ (which can be performed in polynomial time) to identify the observed non-leaf nodes, $\mathcal{V}_{nl,o}$ and the true edges between them. All other observed nodes in the graph $\mathcal{V}_l := \mathcal{V}_o \backslash \mathcal{V}_{nl,o}$ then are leaf nodes.*

Note that of all edges connected to a leaf node in $\mathcal{T}_m$, only one edge is connected to its true non-leaf neighbor in $\mathcal{T}$ (rest are spurious edges). From Assumption 3, each leaf node is at least three hops away from any unobserved node in $\mathcal{T}$. By Lemma 7.4.1 and Remark 7, it clear that spurious edges connected with a leaf node in $\mathcal{T}_m$ include those to its two-hop neighbors. The next result utilizes the phase response of the entries of $\Phi_{oo}^{-1}$ to determine the true and spurious edges associated with leaf nodes.

**Theorem 7.5.2.** *Consider a RLDS such that Assumption 2 and 3 hold. Let $a$ be a leaf node in $\mathcal{T}$ and let $v$ be a non-leaf neighbor of $a$ in $\mathcal{T}_m$. Then, $\angle\Phi_{a,v}^{-1}(\omega) = 0$ for all $\omega \in [0, 2\pi)$ if and only if $a, v$ are two hop neighbors in $\mathcal{T}$.*

The proof uses algebraic expansions of the expressions for $\Phi_{a,v}^{-1}(\omega)$ for leaf $v$ and non-leaf $a$. We use the theorems mentioned above to devise Algorithm 2 that identifies all true edges between observed nodes in the system.

The last task that remains is to locate the unobserved nodes, which is discussed in the next subsection.

### 7.5.2 Location of Unobserved Nodes

After application of Algorithm 1 followed by Algorithm 2, we end up with a graph $\overline{\mathcal{T}}$ of observed nodes and edges between them. However the discovered network will have multiple disconnected radial components, with the disconnections being at the locations of unobserved nodes. We will refer to $\overline{\mathcal{T}}_j$ as a **discovered disconnected component**. For example, consider a tree $\mathcal{T}$ with just one unobserved node $l$ as shown in Fig. 7.2.

**Algorithm 9** True Edge Set Discovery Algorithm

```
Input: $\mathcal{T}_m = (V, \mathcal{E}_{\mathcal{T}_m})$ generated by Algorithm 1
Output: $\overline{\mathcal{T}} = (V, \mathcal{E}_{\overline{\mathcal{T}}})$
Edge set $\mathcal{E}_{\overline{\mathcal{T}}} \leftarrow \{\}$
for all edge $a - b$ in $\mathcal{E}_{\mathcal{T}_m}$ do
    if $Z := \{a, b\}$ there exist $I \neq \{\phi\}$ and $J \neq \{\phi\}$ such that $sep(I, Z, J)$ holds in $\mathcal{T}_m$ then
        $V_{nl} \leftarrow V_{nl} \cup \{a, b\}$, $\mathcal{E}_{\overline{\mathcal{T}}} \leftarrow \mathcal{E}_{\overline{\mathcal{T}}} \cup \{(a, b)\}$
    end if
end for
$V_l \leftarrow V - V_{nl}$
for all $a \in V_l, b \in V_{nl}$ with $(a, b) \in \mathcal{E}_{\mathcal{T}_m}$ do
    if $\angle\Phi_{oo}^{-1}(a, b) \neq 0$ for all $\omega \in [0, 2\pi)$ then
        $\mathcal{E}_{\overline{\mathcal{T}}} \leftarrow \mathcal{E}_{\overline{\mathcal{T}}} \cup \{(a, b)\}$
    end if
end for
```

Let $l$ be between observed nodes $c, e$. Then there exist the path $C - c - l - e - E$ in $\mathcal{T}$, with

$C := \{v \in \mathcal{V} | \text{path between } v, l \text{ involves node } c\}$,

$E := \{v \in \mathcal{V} | \text{path between } v, l \text{ involves node } e\}$.

Using Algorithm 2 leads to discovery of the individual components $C - c$ and $e - E$ in $\overline{\mathcal{T}}$. Based on our assumptions, it can be shown that each such component has at least three observed nodes. Since, $\mathcal{T}$ is a connected graph, the discovered disconnected components need to be connected by locating the unobserved node in $\overline{\mathcal{T}}$. Next, we present the result which enables us to do so.

**Theorem 7.5.3.** *Let $\mathcal{T}_m$ be such that there are links between any two observed nodes that are within four hops in the topology $\mathcal{T}$. Consider two discovered disconnected components $\overline{\mathcal{T}}_1, \overline{\mathcal{T}}_2$ in $\overline{\mathcal{T}}$ with observed nodes $c \in \overline{\mathcal{T}}_1$ and $e \in \overline{\mathcal{T}}_2$. If $\forall\ b \in \overline{\mathcal{T}}_1$, $\forall f \in \overline{\mathcal{T}}_2$ such that $b - c$ and $e - f$ are edges in $\mathcal{T}$ and $b, c, e, f$ form a clique in $\mathcal{T}_m$, then, there exists an unobserved node $l$ such that $c - l - e$ is a path in $\mathcal{T}$.*

Based on Theorem 7.5.3, we present Algorithm 3 that inserts hidden nodes by considering spurious edges between pairs of disconnected components in the discovered network. As each observed node can have a maximum of only one hidden node as neighbor, we merge hidden nodes that may have been duplicated in Algorithm 3 while checking for Theorem 7.5.3 between multiple disconnected components connected to the same hidden node.

**Algorithm 10** Unobserved Node Placement Algorithm

```
Input: $\overline{\mathcal{T}} = (\mathcal{V}_{\overline{\mathcal{T}}}, \mathcal{E}_{\overline{\mathcal{T}}}) = \cup_{j=1}^{h} \overline{\mathcal{T}}_j$
Output: $\tilde{\mathcal{T}} = (V_{\tilde{\mathcal{T}}}, \mathcal{E}_{\tilde{\mathcal{T}}})$.
Node set $V_{\tilde{\mathcal{T}}} \leftarrow \mathcal{V}_{\overline{\mathcal{T}}}$
Edge set $\mathcal{E}_{\tilde{\mathcal{T}}} \leftarrow \mathcal{E}_{\overline{\mathcal{T}}}$
for all $j \in \{1, 2, ..., h\}$ do
    for all $i \in \{j+1, ..., h\}$ do
        if there exist a pair of nodes $a, b$ such that $a \in \overline{\mathcal{T}}_j$ and $b \in \overline{\mathcal{T}}_i$ such that all their neighbors in $\overline{\mathcal{T}}$ are connected in $\mathcal{T}_m$ then
            $V_{\tilde{\mathcal{T}}} \leftarrow V_{\tilde{\mathcal{T}}} \cup l_j$
            $\mathcal{E}_{\tilde{\mathcal{T}}} \leftarrow \mathcal{E}_{\tilde{\mathcal{T}}} \cup \{(a, l_j), (l_j, b)\}$
        end if
    end for
end for
Merge hidden nodes that are neighbors of the same observed node.
```

## 7.6 Results

Topology inference for power distribution networks can be applied towards fault isolation, control and flow optimization. Penetration of devices like Phasor Measurement Units(PMUs) enable real time measurement of phases of various nodes and facilitate inverse problems like topology inference and state estimation [2]. However, these meters cannot be deployed at all nodes and partial network observability is indeed the situation.

We demonstrate the efficacy of the algorithm presented by testing it on data obtained from simulations of the linearized swing equations (see (7.7) below) on a 39 bus radial topology. This radial system is obtained by deleting a few edges from the IEEE 39 bus system and is shown in Figure 7.3(a). The state $x_i(t)$ denotes the fluctuations of the phase angles of node $i$ from equilibrium values while $p_i(t)$ denote the nodal injections due to generation and losses. The nodal injections $p_j$ are colored noise and are generated by filtered version of a white noise sequence. Four nodes are unobserved in this study. For $i = 1, 2, ..., 39$,

$$m_i \ddot{x}_i + d_i \dot{x}_i = \sum_{j=1, j \neq i}^{39} b_{ij}(x_j(t) - x_i(t)) + p_i(t), \tag{7.7}$$

Here, $m_i, d_i, b_{ij} \in \mathbb{R}_{\geq 0}$ for all $i, j \in \{1, 2, ..., 39\}$.

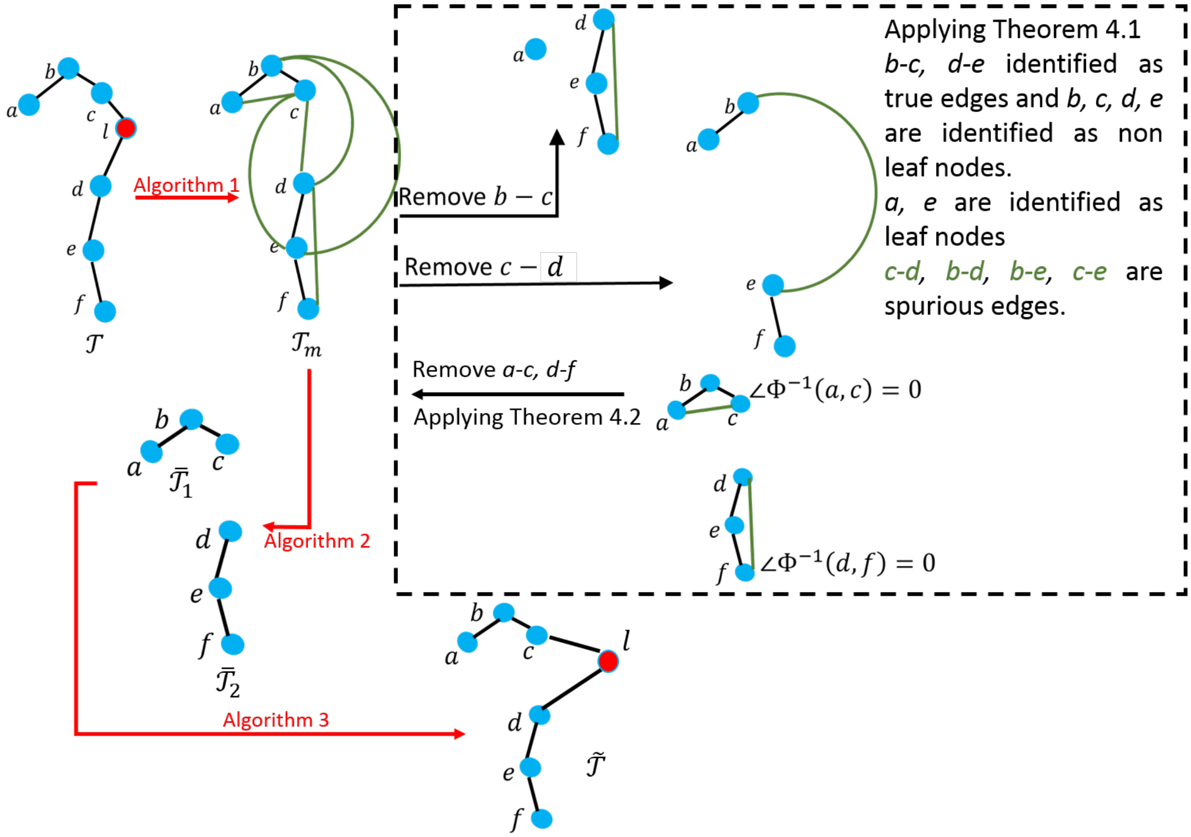

Figure 7.2: Illustration of the application of Algorithm 1, Algorithm 2 and Algorithm 3 in succession. The red node is the latent node and green edges denote the spurious edges up to four hop neighbors.

The error proportion is defined as the ratio of the sum of number of true links undetected and number of false links detected to the total number of true links. The error proportion for the RLDS in Figure 7.3(a) using the algorithms presented previously is shown in Figure 7.3(b). As the samples per observed node is increased it is seen that the error proportion decreases rapidly. We reemphasize that our algorithms do not use any knowledge of the system parameters and noise injections. Moreover, the noise injections used in the simulation is colored noise unlike white noise models used in previous studies.

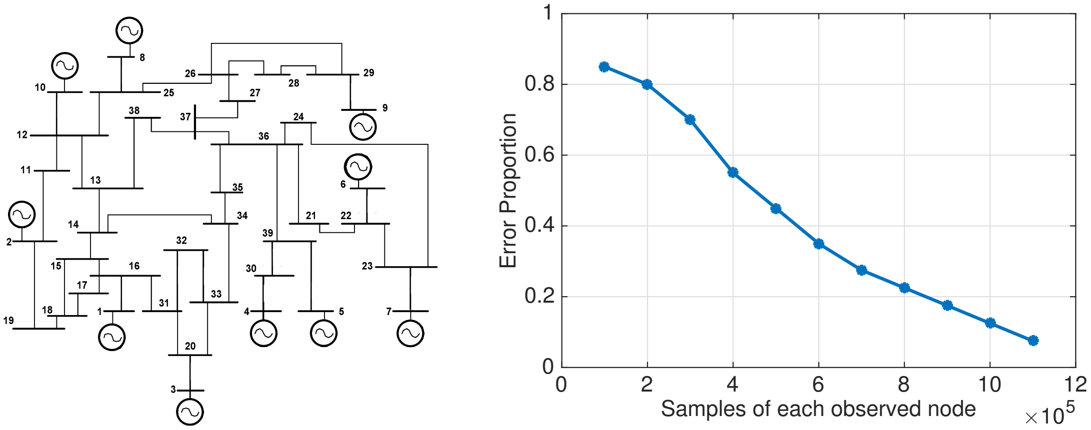

(a) (b)

Figure 7.3: (a) A RLDS obtained from the IEEE 39 bus system, (b) error proportion against the number of samples in topology inference of the system shown in Figure 2(a).

## 7.7 Summary

We presented algorithms, which when applied in succession, leads to the exact topology recovery of a RLDS in the 'sufficient statistics'(large number of data samples) regime under partial observation of the network. The proofs involve a synergy of tools from signal processing and probabilistic graphical models. Algorithm 2 and Algorithm 3 being graph based checks, can be executed in polynomial time. Among all the algorithms presented, Algorithm 1 is computationally most intensive due to computation of the inverse. We demonstrated the performance of the algorithm on a 39 node radial power distribution network. This work also provides insights on placement of sensors for observing the network for monitoring and fault detection applications.

## Chapter 8

# Structure Learning: Cyclostationary Time Series

## 8.1 Prologue

In Chapters $5, 6, 7$, the observed time series were assumed to be wide sense stationary. In this chapter, we expand the scope of the algorithms presented previously to a class of non-stationary processes, namely cyclostationary processes.

## 8.2 Introduction

Cyclostationary processes arise naturally from periodic phenomenon [140]. In telecommunications, telemetry, radar and sonar applications; modulation, sampling, multiplexing, and coding operations give rise to periodicity. Periodicity in mechanical systems is due to rotation and reciprocation of gears, belts, chains, shafts, propellers, pistons, and so on [141]. In power generation the rotational motion of turbines and generators is responsible for periodic AC signals. In inverters PWM switching is responsible for the generation of periodic AC signals. In astronomy, periodicity arises due to rotation and revolution of celestial bodies. In econometric and climate systems, seasonality of markets gives rise to periodic behavior [142, 143].

A common feature of the time series data obtained in these examples is that they exhibit periodic statistics. Often multiple frequencies are observed in the time series data.

These processes are not necessarily periodic functions of time but are characterized by periodic statistics. It of interest to understand the relationship between various components of large scale interconnected dynamical systems like power distribution networks or climate systems. The complexity of such systems call for use of data driven methods to understand system behavior. In this chapter, an algorithm is developed to reconstruct networks of cyclostationary processes which are dynamically related by transfer functions. It is shown that non causal Wiener filtering is capable of reconstructing the kin topology of the network which recovers the set of parents, children and spouses of every agent in the network. Furthermore the reconstruction algorithm is extended to accommodate poly-periodic processes. We show that the algorithm presented is applicable for inferring the interconnection topology of a network of dynamically related processes which can be modeled as Wide Sense Stationary (WSS) processes and demonstrate its robustness for applications where observations are available for finite time.

The chapter is organized as follows. In Section 8.3 we present definitions and key results of cyclostationary processes. Section 8.4 describes a class of models that will suit our purpose of describing an interconnected structure of dynamical systems. Section 8.5 presents basic concepts of non causal Wiener filtering. In Section 8.6 we show that non causal Wiener filtering is able to recover the parents, children and spouses (i.e., Markov blanket) of each node. Section 8.7 deals with simulation results to illustrate the developed algorithm. Section 8.8 summarizes the chapter.

### Notation:

The symbol := denotes a definition
$\|x\|$: 2 norm of a vector $x$
$A_{j*}$: $j-th$ row of matrix $A$
$A_{*i}$: $i-th$ column of matrix $A$
$\mathbf{0}$:zero matrix of appropriate dimension
$A^*$: the conjugate transpose of matrix $A$
$A'$: transpose of a matrix $A$
$A \succ 0$: $A$ is a positive definite matrix

## 8.3 Cyclostationary Processes and Vector Stationary Processes

In this section we present a brief introduction to cyclostationary processes and its connections with vector stationary processes. For more details the reader is referred to [144]. We first recollect the notion of a wide sense stationary(WSS) stochastic process.

A random process $x(t), t \in \mathbb{Z}$ is wide sense stationary *(WSS)* if its mean function, $m(t) := \mathbb{E}[x(t)]$ is constant and correlation function, $R_x(s,t) := \mathbb{E}[x(s)x(t)]$ is a function of $s-t$, where $\mathbb{E}[.]$ denotes the expectation operator. The Fourier transform of the correlation function is the power spectral density which is denoted as $\Phi_x(e^{\iota\omega})$. The random processes $x(t)$ and $y(t)$ are said to be jointly WSS if $x(t)$ and $y(t)$ are WSS and the cross correlation function,$R_{xy}(s,t) := \mathbb{E}[x(s)y(t)]$ is a function of $s-t$. The Fourier transform of the cross correlation function is the cross spectral density which is denoted as $\Phi_{xy}(e^{\iota\omega})$. Next, we define a cyclostationary processes.

**Definition 28** (Cyclostationary Process)**.** *A random process $x(t), t \in \mathbb{Z}$ is said be cyclostationary or periodically correlated process with period $T \in \mathbb{Z}_+$ if for every $s, t \in \mathbb{Z}$,*

$$m(t) = m(t+T) \tag{8.1}$$

$$R_x(s,t) = R_x(s+T, t+T). \tag{8.2}$$

Here, by period we mean the smallest positive integer $T$ for which the above hold. Examples of cyclostationary process: (i) A WSS process is a cyclostationary processes with period 1, (ii) any signal which can be described as a sum of a periodic signal and a wide sense stationary(WSS) noise results in a cyclostationary process.

Two random processes $x(t)$ and $e(t)$ are said to be jointly cyclostationary with period $T$ if $x(t)$ and $e(t)$ are cyclostationary with period $T$ and the cross correlation function $R_{x,e}(s,t) := E(x(s)e(t))$ is periodic with period $T$. Next, we define a vector WSS process.

**Definition 29** (Vector WSS Process)**.** *Consider a q-variate random sequence $X(t) = [x_1(t), \cdots, x_q(t)]', t \in \mathbb{Z}$. Here $X^j(t)$ is used to denote the $j^{th}$ element of $X(t)$. $X(t)$ is* *said to be a vector WSS process if*

$$m_j := \mathbb{E}[x_j(t)],$$

*is a constant for all* $j \in \{1, 2, ..., q\}$*, and,*

$$R_X^{jk}(s,t) := \mathbb{E}[x_j(s)x_k(t)]$$

*is a function of* $s-t$ *for all* $s, t \in \mathbb{Z}$*, and* $j, k \in \{1, 2, \cdots, q\}$*. Here* $m := [m_1, m_2, \cdots, m_q]'$ *is the mean vector* $[R_X^{jk}(\tau)]_{j,k=1}^{q}$ *as the correlation matrix of* $X(t)$*.*

$X(t) \in \mathbb{R}^{1\times q}$ and $Y(t) \in \mathbb{R}^{1\times r}$ are jointly vector WSS process if they are vector WSS processes and $R_{XY}^{jk}(s,t) := \mathbb{E}[X^j(s)Y^k(t)]$ is a function of $s-t$ for all $s, t \in \mathbb{Z}$ and $j \in \{1, 2, ..., q\}, k \in \{1, 2, ..., r\}$.

Lifting is a way of representing scalar time series as a realization of a vector time series. Vector sequences of size $T$ obtained from lifting of scalar sequences $x(t)$ will be indexed by $n$ and denoted as $X(n)$. The scalar sequence $x(t)$ is related to the $T$ variate lifted sequence $X_(n)$ by $X^j(n) = x(j + nT), n \in \mathbb{Z}, j = 0, 1, \cdots, T-1$. The next result relates cyclostationary processes with vector WSS processes.

**Theorem 8.3.1.** [144] *A scalar random sequence* $x(t) : t \in \mathbb{Z}$ *is cyclostationary with period* $T$ *if and only if the* $T$*-variate lifted sequence* $\boldsymbol{X}(n)$ *of* $x()$ *is a vector WSS process.*

*Proof.* ($\Rightarrow$)Suppose $x(t)$ is cyclostationary with period $T$. Let $S := \{0, 1, \cdots, T-1\}$. So,

$$\begin{aligned}
\mathbb{E}[X^j(n)] &= \mathbb{E}[x(j+nT)] = \mathbb{E}[x(j)] := m_j, j \in S \text{ and} \\
R_X^{jk}(n,m) &= \mathbb{E}[X^j(n)X^k(m)] = \mathbb{E}[x(j+nT)x(k+mT)] \\
&= R_x(j+nT, k+mT) = R_x(j+(n-m)T, k) \\
&= \mathbb{E}[x(j+(n-m)T)x(k)] = \mathbb{E}[X^j(n-m)X^k(0)] \\
&= R_X^{jk}(n-m), \text{ for all } n, m \in \mathbb{Z} \text{ and } j, k \in S
\end{aligned}$$

Therefore $X(n)$ is a $T$-variate vector WSS process.

($\Leftarrow$) Suppose $\boldsymbol{X}(n)$ is a $T$ variate vector WSS process obtained by lifting $x(t)$. Then it follows from the definition of vector WSS process that,

$$\begin{aligned} \mathbb{E}[X^j(n)] &= \mathbb{E}[X^j(0)], \text{for all} j \in S, n \in \mathbb{Z} \text{which implies,} \\ \mathbb{E}[x(j+nT)] &= \mathbb{E}[x(j)], \text{for all } j \in S. \end{aligned}$$

Let $j + nT = t$, implying, $j = t - nT$. So,

$$\mathbb{E}[x(t)] = \mathbb{E}[x(t-nT)], \text{for all } t, n \in \mathbb{Z}$$

Let $n = 1$. Thus, $\mathbb{E}[x(t)] = \mathbb{E}[x(t-T)]$, for all $t \in \mathbb{Z}$ and substituting $t - T$ with $p$,

$$\mathbb{E}[x(p+T)] = \mathbb{E}[x(p)], \text{for all } p \in \mathbb{Z}. \tag{8.3}$$

Since, $X(n)$ is vector WSS process,

$$\begin{aligned} &R_X^{jk}(n,m) = R_X^{jk}(n-m), \text{for all } m, n \in \mathbb{Z}, j, k \in S, \text{that is,} \\ &\mathbb{E}[X^j(n)X^k(m)] = \mathbb{E}[X^j(n-m)X^k(0)], \text{ which implies that,} \\ &\mathbb{E}[x(j+nT)x(k+mT)] = \mathbb{E}[x(j+(n-m)T)x(k)]. \end{aligned}$$

Let $s := j + nT$ and $t := k + mT$. Then,

$$\mathbb{E}[x(s)x(t)] = \mathbb{E}[x(s-mT)x(t-mT)], \text{for all } s, t, m \in \mathbb{Z}.$$

Let $m = 1$, it follows that,

$$\mathbb{E}[x(s)x(t)] = \mathbb{E}[x(s-T)x(t-T)], \text{for all } s, t \in \mathbb{Z}.$$

Substituting $s - T, t - T$ with $q, r$ respectively, we have

$$\begin{aligned} \mathbb{E}[x(q+T)x(r+T)] &= \mathbb{E}[x(q)x(r)], \text{for all } q, r \in \mathbb{Z} \\ R_x(q+T, r+T) &= R_x(q, r), \text{for all } q, r \in \mathbb{Z} \end{aligned}$$

Therefore $x_t$ is cyclostationary with period $T$. This completes the proof. □

**Theorem 8.3.2.** *If $x(n)$ and $e(n)$ are jointly cyclostationary sequence with period $T$,* *Then* $y(n) := h(n) * x(n) + e(n)$ *is cyclostationary with period* $T$. *Here, * denotes the convolution operator.*

*Proof.* It can be easily verified that $\mathbb{E}[y(s)] = \mathbb{E}[h(s)*x(s)+e(s)] = \sum_{k=-\infty}^{k=\infty} h(k)\mathbb{E}[x(s-k)] + \mathbb{E}[e(s)]$. Similarly, one can show that $\mathbb{E}[y(s+T)] = \sum\limits_{k=-\infty}^{k=\infty} h(k)\mathbb{E}[x(s+T-k)] + \mathbb{E}[e(s+T)]$. Since, $x(n)$ and $e(n)$ are cyclostationary with period $T$, $\mathbb{E}[x(s-k+T)] = \mathbb{E}[x(s-k)]$ and $\mathbb{E}[e(s+T)] = \mathbb{E}[e(s)]$. Therefore, $\mathbb{E}[y(s+T)] = \mathbb{E}[y(s)]$, for all $s \in \mathbb{Z}$. Let us now look at the correlation function of $y(n)$.

$$
\begin{aligned}
&R_y(s,t) = \\
&\mathbb{E}[(\sum_{k=-\infty}^{k=\infty} h(k)x(s-k) + e(s))(\sum_{j=-\infty}^{j=\infty} h(j)x(t-j) + e(t))] \\
&= \sum_{k=-\infty}^{k=\infty} h(k) \sum_{j=-\infty}^{j=\infty} h(j)R_x(s-k,t-j) + \\
&\sum_{j=-\infty}^{j=\infty} h(j)R(ex)(s,t-j) + \sum_{k=-\infty}^{k=\infty} h(k)R_{xe}(s-k,t) + R_e(s,t).
\end{aligned}
$$

Similarly,

$$
\begin{aligned}
&R_y(s+T,t+T) = \\
&\sum_{k=-\infty}^{k=\infty} h(k) \sum_{j=-\infty}^{j=\infty} h(j)R_x(s+T-k,t+T-j) \\
&+ \sum_{j=-\infty}^{j=\infty} h(j)R_{ex}(s+T,t+T-j) \\
&+ \sum_{k=-\infty}^{k=\infty} h(k)R_{xe}(s+T-k,t+T) + R_e(s+T,t+T).
\end{aligned}
$$

Since, $x(n)$ and $e(n)$ are jointly cyclostationary with period $T$, $R_x(s-k+T, t-j+T) = R_x(s-k,t-j), R_{ex}(s+T,t+T-j) = R_x(s,t-j), R_{xe}(s+T-k,t+T) = R_{xe}(s-$

$k, t)$ and $R_e(s+T, t+T) = R_e(s,t)$. Therefore,

$$R_y(s+T, t+T) = R_y(s,t), \text{for all } s, t \in \mathbb{Z}.$$

Thus, $y_n$ is cyclostationary with period $T$. $\square$

The above theorem states that the processing of a cyclostationary signal by a linear time invariant filter is a cyclostationary process with the same period.

## 8.4 Topology Learning: Problem Formulation

Consider a collection of $m$ cyclostationary time series $\{x_j(t)\}_{j\in\{1,2,\dots,m\}, t\in\mathbb{Z}}$ such that,

$$x_j(k) = \sum_{i=1, i\neq j}^{m} h^{ji}(k) * x_i(k) + e_j(k), \tag{8.4}$$

where, $e_j(k)$ is an exogenous input influencing the evolution of time series $x_j(k)$. Consider, $\{x_j(k)\}_{j=1}^{m}$ and $\{e_j(k)\}_{j=1}^{m}$ to be jointly cyclostationary processes with period $T$, with, $e_i(k)$ uncorrelated with $e_j(k)$, for $i \neq j, k \in \mathbb{Z}$. Using $z$ transform,

$$\mathsf{x}_j(z) = \mathsf{e}_j(z) + \sum_{i=1, i\neq j}^{n} H_{ji}(z)\mathsf{x}_i(z),$$

where, $\mathsf{x}_i(z), \mathsf{e}_j(z)$ is the $z$ transform of $x_i(k), e_j(k)$ respectively. Here, $H_{ji}(z)$ is the transfer function. Consider a directed graph $\mathcal{G} := (\mathcal{V}, \mathcal{A})$, where, $\mathcal{V} = \{1, \dots, m\}$ denotes the nodes or vertices and $\mathcal{A} := \{(j,i) | i, j \in \mathcal{V}, H_{ji}(z) \neq 0 \ a.s.\}$ denotes the edge set (ordered pairs). The edge $(j,i)$ is represented as an arrow starting at $i$ and ending in $j$ $(i \rightarrow j)$. In this chapter, $\mathcal{G} := (\mathcal{V}, \mathcal{A})$ is said to be the generative graph of the processes $\{x_j(k)\}_{j\in\{1,\dots,m\}, k\in\mathbb{Z}}$. We refer to $j$ as the child of $i$ and $i$ as parent of $j$ if $H_{ji}(z) \neq 0$ almost surely. Moreover, we refer to $i \in \mathcal{V}$ and $j \in \mathcal{V}$ as spouses if there exist $k \in \mathcal{V}$ such that $H_{ki}(z) \neq 0$ and $H_{kj}(z) \neq 0$ almost surely. Let $C_j, P_j, K_j$ denote the set of all children, parents and spouses of node $j$. Next, we define the topology, $\mathcal{G}_T$ and moral graph $\mathcal{G}_M$ associated with a generative graph $\mathcal{G}$.

**Definition 30** (Topology of a graph). *Given a generative graph* $\mathcal{G} = (\mathcal{V}, \mathcal{A})$*, its topology*

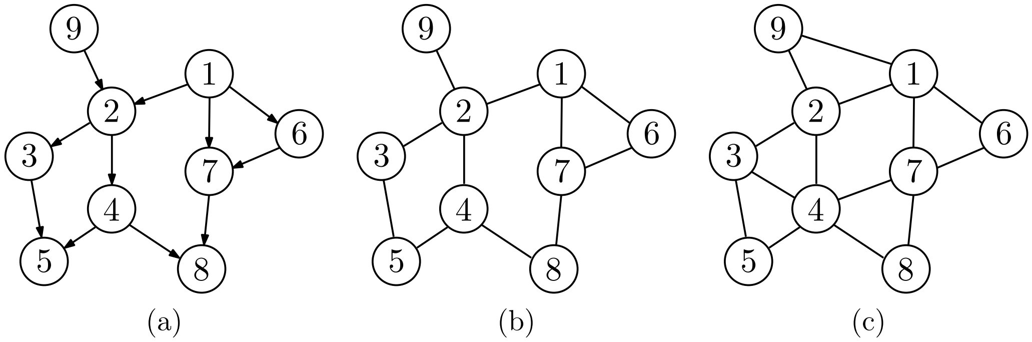

(a) (b) (c)

Figure 8.1: (a) A directed graph, (b) its topology (nodes 2 and 3 are neighbors, 2 and 5 are two hop neighbors) and (c) its moral graph.

*$\mathcal{G}_T$ is the undirected graph that is obtained by removing the orientation on all edges of $\mathcal{G}$ and avoiding repetition. An example of a generative graph is represented in* Figure 8.1(a) *with its topology in* Figure 8.1(b).

**Definition 31** (Moral Graph)**.** *Given a generative graph $\mathcal{G}$, its moral $\mathcal{G}_M$ is the undirected graph that is obtained by removing the orientation on all edges of $\mathcal{G}$ avoiding repetition and adding an undirected edge between spouses in $\mathcal{G}$. As an example,* Figure 8.1(c) *is the moral graph of the generative graph represented in* Figure 8.1(a).

**Topology learning** addressed in this chapter refers to reconstruction of $\mathcal{G}_T$ from only the cyclostationary time series measurements from the nodes, $\{x_j(k)\}_{j=1,k\in\mathbb{Z}}^{m}$, based on the dynamics described by (8.4). We will now discuss the application of lifting technique to transform the objective of topology inference for a collection of cyclostationary processes into topology inference of a collection of vector stationary processes. Using Theorem 8.3.1, $x_j(k)$ can be mapped into a $T$-variate vector stationary process $X_j(n)$. Similarly, the exogenous input $e_j(k)$ can be mapped into a $T$ variate vector stationary process $E_j(n)$ which is uncorrelated with and $\{E_i(n)\}_{i\neq j}$. We assume that the vector WSS processes $\{X_j(n)\}_{j=\{1,\dots,m\}}$ zero mean vector stationary processes. The network dynamics of the equivalent vector WSS processes in $z$ domain is given by,

$$\begin{aligned}
\mathsf{X}_j(z) &= \sum_{i=1}^{m} \mathcal{H}_{ji}(z)\mathsf{X}_i(z) + \mathsf{E}_j(z), \text{ where,} \qquad (8.5)\\
\mathsf{X}_j(z) &= [1 \ z \ \cdots \ z^{T-1}]'\mathsf{x}_j(z),\\
\mathsf{E}_j(z) &= [1 \ z \ \cdots \ z^{T-1}]'\mathsf{e}_j(z),\\
\mathcal{H}_{ji}(z) &= diag\{1, z, ..., z^{T-1}\}H_{ji}(z),
\end{aligned}$$

where, $\mathcal{H}_{ji}(z)$ is $T \times T$ transfer matrix and $I_{T\times T}$ is the identity matrix of size $T \times T$. If there is no dynamical link from $x_i(k)$ to $x_j(k)$ then $H_{ji}(z) = 0$, which implies, $\mathcal{H}_{ji}(z) = \mathbf{0}$ ($\mathbf{0}$ denotes a matrix of zeros of appropriate dimension), which means that there is no dynamical link from the vector stationary process $X_i(k)$ to $X_j(k)$. Similarly, if there is no dynamical link from $X_i(k)$ to $X_j(k)$ then $\mathcal{H}_{ji}(z) = \mathbf{0}$, which implies $H_{ji} = 0$, that is, there is no dynamical link from the scalar cyclostationary process $x_i(k)$ to $x_j(k)$. The notion of a generative graph for a collection of cyclostationary processes can be analogously carried forward to the equivalent representation of vector stationary processes. Note that the generative graph, topology and moral graph are identical for both the representations. Thus, we have the following Lemma.

**Lemma 8.4.1.** *Two cyclostationary processes have a dynamical link (through a transfer function) if and only if there is a dynamical link between their vector stationary process representations (through a transfer matrix). Moreover, the structure of the generative graph, topology and moral graph is preserved under lifting of a collection of cyclostationary processes into vector stationary processes.*

*Proof.* The proof follows from the discussion above. □

Theorem 8.3.1 and Lemma 8.4.1 enable us to interpret a dynamical network of scalar cyclostationary processes as a dynamical network of vector stationary processes. This enables us to design topology inference algorithms for the vector stationary representation and presence/absence of links in the vector stationary representation is directly mapped to the presence or absence of links in the scalar cyclostationary case. The discussion henceforth would focus on the inference of topology of a network of $T \times 1$ vector stationary processes.

## 8.5 Wiener Separation

We assume that the operator $(\mathbb{I}-\mathbb{H}(z))$ is invertible and the power spectral density matrix of the exogenous inputs $E(k)$, $\Phi_E(e^{\iota\omega})$ is positive definite almost surely. Consider the following least squares problem,

$$\inf_{\{W_{ij}(k)\}_{i=1,i\neq j,k\in\mathbb{Z}}^{m}} \mathbb{E}(X_i(k) - \sum_{i=1,j\neq i}^{m} \boldsymbol{W}_{ij}(k) * X_j(k))^2, \tag{8.6}$$

for all $k \in \mathbb{Z}$. Here, $*$ denotes a convolution operator and $\boldsymbol{W}_{ij}(k)$ is a $T \times T$ impulse response matrix of filtering the vector valued process $X_j(k)$. The least squares solution for estimation of $X_i(k)$ from the rest of the time series $X_{\bar{i}}(k) := [X_1(k)', ..., X_j(k)', ..., X_m(k)']'_{j\neq i}$ as shown above is known as the multivariate Wiener filter, which is given by, $\mathbf{W}_i(z) = \Phi_{X_i X_{\bar{i}}} \Phi_{X_{\bar{i}}}^{-1}$. Then, $\hat{\mathsf{X}}_i(z) = \mathbf{W}_i(z)\mathsf{X}_{\bar{i}}(z)$ is the closest approximation of $\mathsf{X}_i(z)$ based on the rest of the time series (using Parseval theorem, $\hat{X}_i(k)$ is the closest approximation of $X_i(k)$ based on $X_{\bar{i}}(k)$). Here, $\mathbf{W}_i(z)$ is a $T \times (m-1)T$ matrix and is of the form $\mathbf{W}_i(z) = [\mathbf{W}_{i,1}(z) ... \mathbf{W}_{i,i-1}(z)\ \mathbf{W}_{i,i+1}(z)\ ...\ \mathbf{W}_{i,m}(z)]$, where $\{\mathbf{W}_{i,j}(z)\}_{j=1,j\neq i}^{m}$ is a $T \times T$ transfer matrix. Please refer to the Section 8.9 for a detailed derivation of multivariate Wiener filtering. Next we introduce the definition of conditional non causal Wiener uncorrelation or Wiener separation.

**Definition 32** (Wiener Uncorrelated or Wiener Separated)**.** *Let $V(k)$, $X_1(k), ..., X_m(k)$ be vector stationary processes obtained from lifting of the jointly cyclostationary processes $v(k), x_1(k), ..., x_m(k)$ respectively. The process $V(k)$ is said to be Wiener-uncorrelated with $X_i(k)$, for any $i \in \{1, ..., m\}$, given the processes $\{X_j(k)\}_{j\neq i}$ if the i-th block of the Wiener filter to estimate $V(k)$ from $X(k) := [X_1(k)'\ ...\ X_m(k)']'$ is zero, that is, $\Phi_{VX}\Phi_X^{-1}\boldsymbol{B}_i = \mathbf{0}$, where, $\boldsymbol{B}_i = [\mathbf{0}\ \mathbf{0}\ \cdots\ \mathbf{0}\ \boldsymbol{I}_{T\times T}\ \mathbf{0}\ \cdots\ \mathbf{0}]'$ is a matrix $\in \mathbb{R}^{mT\times T}$ that has $\boldsymbol{I}_{T\times T}$ (identity matrix) as the $i-th$ block and $\mathbf{0}$ as all other blocks.*

**Lemma 8.5.1.** *Let $X_1(k), ..., X_m(k)$ be $T \times 1$ vector stationary processes and define $X(k) = [X_1(k)'\ ...\ X_m(k)'(k)]'$. Assume that $\Phi_X$ has full normal rank. The process $X_i(k)$ is Wiener-uncorrelated with $X_j(k)$ given the processes $\{X_l(k)\}_{l\neq i,j}$, if and only if, the $(i,j)$ block matrix, or equivalently the $(j,i)$ block matrix, of $\Phi_X^{-1}(e^{\iota\omega})$ is $\mathbf{0}$, that is,* *for $i \neq j$,*

$$\boldsymbol{B}_j' \Phi_X^{-1} \boldsymbol{B}_i = \boldsymbol{B}_i' \Phi_X^{-1} \boldsymbol{B}_j = \mathbf{0}. \tag{8.7}$$

*Proof.* Without any loss of generality, let $j = m$ and define $X_{\overline{m}}(k) = [X_1(k)' \dots X_{m-1}(k)']'$. Let $\mathsf{W}_{m\overline{m}}(z)$ be the non-causal Wiener filter for estimating $X_m(k)$ from $\{X_{\overline{m}}(k)\}_{k \in \mathbb{Z}}$. Then

$$\mathsf{X}_m(z) = \mathcal{E}_m(z) + \mathsf{W}_{m\overline{m}}(z)\mathsf{X}_{\overline{m}}(z) \tag{8.8}$$

where, from (8.14), the error $\mathcal{E}_m(z)$ has the property that $\Phi_{\mathcal{E}_m X_{\overline{m}}}(z) = \mathbf{0}$. Define $\mathsf{R}(z) := [\mathsf{X}_{\overline{m}}'(z), \mathcal{E}_m(z)']'$ and observe that,

$$\mathsf{R}(z) = \begin{pmatrix} \boldsymbol{I}_{(m-1)T} & \mathbf{0} \\ -\mathsf{W}_{m\overline{m}}(z) & \boldsymbol{I}_T \end{pmatrix} \mathsf{X}(z);$$

$$\mathsf{X}(z) = \begin{pmatrix} \boldsymbol{I}_{(m-1)T} & \mathbf{0} \\ \mathsf{W}_{m\overline{m}}(z) & \boldsymbol{I}_T \end{pmatrix} \mathsf{R}(z).$$

It follows that,

$$\Phi_R(z) = \begin{pmatrix} \Phi_{X_{\overline{m}}}(z) & \mathbf{0} \\ \mathbf{0} & \Phi_{\mathcal{E}_m}(z) \end{pmatrix};$$

$$\Phi_X = \begin{pmatrix} \boldsymbol{I}_{(m-1)T} & \mathbf{0} \\ \mathsf{W}_{m\overline{m}}(z) & \boldsymbol{I}_T \end{pmatrix} \Phi_R(z) \begin{pmatrix} \boldsymbol{I}_{(m-1)T} & \mathbf{0} \\ \mathsf{W}_{m\overline{m}}(z) & \boldsymbol{I}_T \end{pmatrix}^*,$$

which implies that,

$$\begin{aligned} &\Phi_X^{-1}(z) \\ &= \begin{pmatrix} \boldsymbol{I}_{(m-1)T} & -\mathsf{W}_{m\overline{m}}^*(z) \\ \mathbf{0} & \boldsymbol{I}_T \end{pmatrix} \Phi_R{}^{-1}(z) \begin{pmatrix} \boldsymbol{I}_{(m-1)T} & \mathbf{0} \\ -\mathsf{W}_{m\overline{m}}(z) & \boldsymbol{I}_T \end{pmatrix} \\ &= \begin{pmatrix} \Phi_{X_{\overline{m}}} + \mathsf{W}_{m\overline{m}}^* \Phi_{\mathcal{E}_m}^{-1} \mathsf{W}_{m\overline{m}} & -\mathsf{W}_{m\overline{m}}^* \Phi_{\mathcal{E}_m}^{-1} \\ -\Phi_{\mathcal{E}_m}^{-1} \mathsf{W}_{m\overline{m}} & \Phi_{\mathcal{E}_m}^{-1} \end{pmatrix} (z) \end{aligned}$$

Pre-multiplying $\Phi_X^{-1}$ by $\boldsymbol{B}_m'$ and post-multiplying by $\boldsymbol{B}_i$ with $i \neq m$ provides the $(m, i)$

block matrix of $\Phi_X^{-1}$. Thus,

$$\boldsymbol{B}'_m \Phi_X^{-1}(z) \boldsymbol{B}_i = -\Phi_{\mathcal{E}_m}^{-1}(z) \mathsf{W}_{m\overline{m}}(z) \boldsymbol{B}_i$$

In the above step there is a slight abuse of notation for $\boldsymbol{B}_i$ on the right hand side of the equation. The $\boldsymbol{B}_i$ on the right hand side is of dimension $(m-1) \times T$ while on the right hand side is $mT \times T$.

($\Rightarrow$) Suppose $X_m(k)$ is Wiener uncorrelated with $X_i(k)$. Then $\mathsf{W}_{m\overline{m}}(z)\boldsymbol{B}_i = \mathbf{0}$ which implies $\boldsymbol{B}'_m \Phi_X^{-1} \boldsymbol{B}_i = \mathbf{0}$.Thus, $(m, i)$ as well as $(i, m)$ block matrix of $\Phi_X^{-1}$ is $\mathbf{0}$.

($\Leftarrow$) Suppose that the $(m, i)$ block of $\Phi_X^{-1}$ is $\mathbf{0}$. Then $-\Phi_{\mathcal{E}_m}^{-1} \mathsf{W}_{m\overline{m}}(z)\boldsymbol{B}_i = \mathbf{0}$,which implies $\mathsf{W}_{m\overline{m}}(z)\boldsymbol{B}_i = \mathbf{0}$. Thus, $X_m(k)$ and $X_i(k)$ are Wiener uncorrelated. □

## 8.6 Structure Learning using Wiener Filtering

In this section we present results which are sufficient conditions to determine if two nodes are kins. Consider the generative graph $\mathcal{G}$ associated with the $T$ variate vector stationary time series $\{X_i(k)\}_{i=1,\dots,m,k\in\mathbb{Z}}$ with dynamics described by (8.5). The dynamics of all the nodes can be collectively written as,

$$\mathsf{X}(z) = \mathbb{H}(z)\mathsf{X}(z) + \mathsf{E}(z), \tag{8.9}$$

where, $\mathsf{X}(z)$ is the z transform of $X(k) = [X_1(k)' \ \dots \ X_m(k)']'$, $\mathsf{E}(z)$ is the $z$ transform of $E(k) = [E_1(k)' \ \dots \ E_m(k)']'$ and $\mathbb{H}(z)(i,j) = \mathcal{H}_{ij}(z)$. We assume that $(\mathbb{I} - \mathbb{H}(z))^{-1}$ exists almost surely (referred as well posedness condition) and $\Phi_E(e^{\iota\omega})$ is positive definite for all $\omega \in [0, 2\pi)$ almost surely (referred as topological detectability condition). With these two assumptions, we will show that if two nodes $i$ and $j$ are not parents, children or spouses in the generative graph $\mathcal{G}$ then the Wiener filter transfer matrix for estimating $X_i(k)$ from $X_j(k)$ given the rest of the time series (and vice versa) is a zero matrix.

**Theorem 8.6.1.** *Consider a generative graph $\mathcal{G}$ associated with the $T$ variate vector stationary processes $\{X_i(k)\}_{i=\{1,\dots,m\},k\in\mathbb{Z}}$ described by (8.5) and is well-posed and topologically detectable . Let $\mathsf{X}(z)$ be the z transform of $X(k) := [X_1(k)', \dots, X_m(k)']'$. Define the space $\mathcal{X}_j =$ tf-span$\{X_i\}_{i\neq j}$. The approximation of the signal $X_j(k)$ using rest of the* *time series based on multivariate Wiener filtering is given by,*

$$\hat{X}_j(z) = \sum_{i \neq j} \boldsymbol{\mathsf{W}}_{ji}(z) X_i(z). \tag{8.10}$$

*Then* $\boldsymbol{\mathsf{W}}_{ji}(z) \neq \mathbf{0}$ *implies* $i \in C_j \cup P_j \cup K_j$.

*Proof.* The collective dynamics of entire collection of time series, $\mathsf{X}(z)$ is given by $\mathsf{X}(z) = (\mathbb{I} - \mathbb{H}(z))^{-1}\mathsf{E}(z)$ which implies that

$$\Phi_X^{-1}(z) = (\mathbb{I} - \mathbb{H}(z))^* \Phi_E^{-1}(z)(\mathbb{I} - \mathbb{H}(z)). \tag{8.11}$$

Consider the $(i, j)$ block matrix of $\Phi_X^{-1}(z)$, with $i \neq j$. Using the block diagonal structure of $\Phi_E$ we have,

$$\begin{aligned}
\boldsymbol{B}_j' \Phi_X^{-1} \boldsymbol{B}_i &= (\boldsymbol{B}_j{}' - (\mathbb{H}_{*,j})^*) \Phi_E^{-1} (\boldsymbol{B}_i - \mathbb{H}\boldsymbol{B}_i) \\
&= -\Phi_{E_j}^{-1} \boldsymbol{B}_j' \mathbb{H}_{*,i} - (\mathbb{H}_{*,j})^* \boldsymbol{B}_i \Phi_{E_i}^{-1} + \sum_{k=1}^{m} (\mathbb{H}_{k,j})^* \Phi_{E_k}^{-1} (\mathbb{H}_{k,i}) \\
&= -\Phi_{E_j}^{-1} \mathbb{H}_{j,i} - \mathbb{H}_{i,j}{}^* \Phi_{E_i}^{-1} + \sum_{k=1}^{m} (\mathbb{H}_{k,j})^* \Phi_{E_k}^{-1} (\mathbb{H}_{k,i}) \\
&= -\Phi_{E_j}^{-1} \mathcal{H}_{ji} - \mathcal{H}_{ij}{}^* \Phi_{E_i}^{-1} + \sum_{k=1}^{m} (\mathcal{H}_{kj})^* \Phi_{E_k}^{-1} (\mathcal{H}_{ki}).
\end{aligned} \tag{8.12}$$

The theorem is proved if it is shown that given $i$ is not a child, parent or spouse of $j$ then $\boldsymbol{\mathsf{W}}_{ji}(z) = \mathbf{0}$. If $i$ is not parent of $j$ then $\mathcal{H}_{ij}(z) = \mathbf{0}$, if $i$ is not a child of $j$ then $\mathcal{H}_{ij}(z) = \mathbf{0}$, and if $i$ and $j$ are not spouses then there does not exist any $k \in \{\{1, ..., m\} | \mathcal{H}_{kj}(z) \neq \mathbf{0}$ and $\mathcal{H}_{ki}(z) \neq \mathbf{0}\}$. Thus, the entry $(j, i)$ block of $\Phi_X^{-1}(z)$ is null. Using Lemma (8.5.1), $\boldsymbol{\mathsf{W}}_{ji}(z) = \mathbf{0}$ and the assertion is proved. $\square$

**Remark 10.** *The above result does not guarantee that if* $i$ *is a child, parent or spouse of* $j$ *then,* $\boldsymbol{\mathsf{W}}_{ji}(z) \neq \mathbf{0}$ *almost surely. However, in such a case, to obtain* $\boldsymbol{\mathsf{W}}_{ji}(z) = \mathbf{0}$ *almost surely, the terms on the right hand side of (8.12) should add up to zero, that is, the system transfer functions and exogenous input must satisfy a particular constraint for* $\boldsymbol{\mathsf{W}}_{ji}(z) = \mathbf{0}$ *almost surely, despite* $i$ *being a child, parent or spouse of* $j$ *in* $\mathcal{G}$. *System parameters have to take specific values for the constraint to be satisfied and hence, such* *cases are deemed pathological. For most applications, the above result can be used as an 'if and only if' result.*

Using the above Theorem and Remark, we arrive at the following algorithm, which enables us to infer the moral graph $\mathcal{G}_M$ of $\mathcal{G}$ from the measured time series $\{x_1(k), ..., x_m(k)\}_{k\in\mathbb{Z}}$.

**Algorithm 11** Learning Algorithm for learning the moral graph of LDG with cyclostationary inputs

**Input:** Time series $X_i(k)$ for each node $i \in \{1, 2, ...m\}$ which is WSCS. Thresholds $\rho$. Frequency points $\Omega$.

**Output:** Reconstruct the kin topology with an edge set $\mathcal{E}_{\mathcal{K}}$

```
Perform a periodogram analysis of the time series data to determine the period $T$. Arrange each cyclostationary time series as vectors of size $T$
for all $l \in \{1, 2, ..., n\}$ do
    Compute the Wiener filter $\boldsymbol{W}_{lp}(z)$ using the voltage time series $\forall p \in \{1, 2, ..., m\} \setminus l$
end for
Edge set $\bar{\mathcal{E}}_K \leftarrow \{\}$
for all $l, p \in \{1, 2, ..., n\}, l \neq p$ do
    if $\|[\boldsymbol{W}_{pl}(z)]\|_\infty > \rho$ then
        $\bar{\mathcal{E}}_K \leftarrow \bar{\mathcal{E}}_K \cup \{(l, p)\}$
    end if
end for
Edge set $\mathcal{E}_{\mathcal{K}} \leftarrow \bar{\mathcal{E}}_{\mathcal{K}}$
Error $= \frac{\text{Number of false edges}}{\text{Number of true edges}}$
```

**Remark 11.** *Suppose that the mean and correlation function of $\{x_j(k)\}_{j=1}^{j=m}$ are periodic with period $T_1, T_2, \cdots, T_n$, that is, the second order statistics of the time series are poly periodic. The moral graph inference procedure described above for cyclostationary process with period $T$ is applicable to poly-periodic processes with $T = T_{eff} = LCM\{T_1, T_2, \cdots, T_n\}$ where poly-periodic processes can be treated as cyclostationary processes with period $T_{eff}$. Here, $LCM$ stands for the Least Common Multiple.*

It is important to note that non causal Wiener filtering provides information on the presence or absence of the link and no conclusion on the direction of the arrows can be drawn from it. This approach returns the moral graph of the generative graph and not the exact topology of the generative graph. The moral graph contains spurious edges between spouses which is not present in the true topology of the generative graph. In the next section, we show that for tree topology with the generative graph being bi-directed, the spurious edges obtained in the moral graph can be pruned out to obtain the true topology.

## 8.7 Simulation Results

### 8.7.1 Validation on cyclostationary and poly periodic processes

A simulation is performed in Matlab to illustrate the reconstruction procedure using non causal Wiener filtering for networks of cyclostationary processes. A five node network as shown in Figure 8.2 is used for the illustration of the key results derived earlier. In this network, node 2 and node 3 are spouses. Each link in Figure 8.2(a) is a 4th order finite impulse response transfer function $1 + 0.9z^{-1} + 0.5z^{-2} + 0.3z^{-3}$. The sequence $e_i$ used is simulated as zero mean white Gaussian noise. Node 1 has a sinusoid of frequency $\pi/3$ rad/sample which is an exogenous input and is responsible for the time series of all nodes being cyclostationary with period $T = 6$ samples. The network is simulated and about initial 600 samples are removed to ensure that the observed data is cyclostationary and transient effects are removed. The time period $T$ is estimated from the periodogram of the observed data by rounding it off to the nearest integer. The presence or absence of a link is decided by comparing the 2 norm of the Wiener filter matrix $\boldsymbol{W}_{ij}(z)$ to a threshold of 0.1. If the 2 norm of $\boldsymbol{W}_{ij}(z) < 0.1$ then it is decided that $\boldsymbol{W}_{ij}(z)$ is negligible and there is no edge between node $i$ and node $j$. It is seen in Figure 8.2(b) that the Wiener reconstruction provides the kin topology of the original graph associated with the true linear dynamic graph. The Wiener reconstruction introduces a spurious link between nodes 2 and 3 because these nodes share a common child and hence are kins.

Next we show the extension of the algorithm to poly-periodic processes. The setup is the same as in Figure 8.2(a) with the difference being that the exogenous inputs to Node 1 are now multiple sinusoids with frequency $2\pi/9, \pi/3$ and $2\pi/3$ rad/ sample. These multiple frequencies are responsible for the poly-periodicity of the $2^{nd}$ order statistics with periods $T = 9, 6$ and 3 samples. These periods are being estimated from the data using periodogram analysis which now shows three peaks corresponding to the

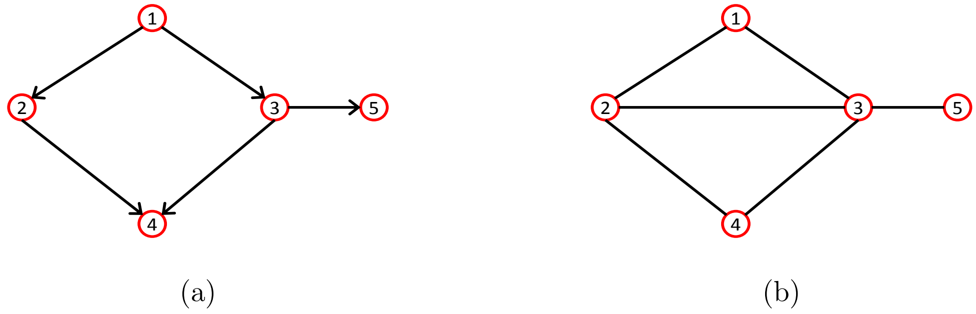

Figure 8.2: The associated graph of a Linear Dynamic Graph of cyclostationary processes (a) and the reconstructed graph obtained using the Wiener projection technique suggested by Theorem 8.6.1 (b). Spurious links are introduced between the spouses 2-3.

respective frequencies. The reconstruction procedure developed for cyclostationary processes is applied to the poly-periodic data with $T_{eff} = LCM\{9, 6, 3\} = 18$ samples. The reconstructed topology is the same as shown in Figure 8.2(b). This example illustrates that non causal Wiener filtering is capable of inferring the kin topology of LDGs of poly-periodic processes.

### 8.7.2 Evidence of Robustness to Finite Data Effects

WSS processes are cyclostationary processes with period 1. Thus, the $2^{nd}$ order statistics of WSS processes are periodic with a period $T$, where $T$ is any natural number. Using Theorem 8.3.1, it is concluded that WSS processes have equivalent $T$ dimensional vector stationary process representations. So there are two ways to reconstruct the underlying structure of a LDG of WSS processes -

1. Wiener filtering of WSS processes to detect kin relationships [145]. Here, the reconstruction procedure adds a link between nodes $i$ and $j$ if the Wiener filter transfer function between $i$ and $j$ is non zero.

2. Wiener filtering of the equivalent $T$ dimensional vector stationary processes using Theorem 8.6.1 to infer the kin topology. In this approach the reconstruction algorithm identifies a link between node $i$ and $j$ if the Wiener filter transfer matrix (of size $T \times T$) between nodes $i$ and $j$ is non zero.

It is essential to note that decision on absence of link is taken based on $T^2$ transfer functions being zero in the $2^{nd}$ method described above while in the $1^{st}$ method the decision on absense of link is based on just a single transfer function. Thus it can be said that the $2^{nd}$ procedure is robust to detection of links because of larger number of decision variables. This could be useful to address link detection issues when the observations are not of sufficient length. Consider the 5 node LDG of Figure 8.2 (without the exogenous sinusoidal inputs at Node 1) with the outputs of the 5 nodes being WSS time series data. We consider data length of 100 samples for each node and apply both the reconstruction approaches described above. The $1^{st}$ procedure detects a false link between $1-4, 1-5$ and does not detect the $1-3$ link. The $2^{nd}$ procedure with $T=3$ does not provide any false link and is able to reconstruct the exact kin topology of the network. The $1^{st}$ procedure is able to reconstruct the exact kin topology when 400 observations are used. Thus, treating scalar WSS processes as vector stationary processes results in robust reconstruction of network topology when limited data is available.

## 8.8 Summary

In this chapter we demonstrate that non causal Wiener filtering is capable of recovering the kin topology of a LDG of cyclostationary processes. This is based on the fact that a cyclostationary process with period $T$ has an equivalent $T$ dimesnsional vector stationary process representation. This approach is restricted to integer periodicity of the second order statistics of the cyclostationary processes. This approach can also be applied to poly-periodic processes with the effective period being the $LCM$ of all the periods present in the time series. It has been shown that Wiener filtering suggests "d-separation" of the sources and the loads by the inverters and this observation has also been justified from a power system dynamics viewpoint. It is important to note that Wiener filtering based reconstruction of WSS processes is not applicable to cyclostationary processes. However, the approach presented here can be applied to WSS processes because WSS processes are cyclostationary processes with period 1 and hence with any period $T$ with $T$ being any natural number. It is shown by a simulation that treating WSS processes as cyclostationary processes with period $T$ and then applying the reconstruction procedure presented in this chapter results in robust reconstruction as compared to reconstruction based on direct Wiener filtering of WSS processes when limited data is available for reconstruction.

## 8.9 Wiener Filtering Derivation

Let $\mathcal{E}$ be a set containing discrete time jointly vector stationary processes such that for any $E_i, E_j \in \mathcal{E}$, the power spectral density matrix $\Phi_{E_iE_j}(z)$ exists ($z$ transform of the cross correlation matrix) with each element of $\Phi_{E_iE_j}(z)$ being real rational with no poles on the unit circle and given by

$$[\Phi_{E_iE_j}(z)](m,n) = \frac{A(z)}{B(z)},$$

where $[\Phi_{E_iE_j}(z)](m,n)$ is the $(m,n)^{th}$ element of $\Phi_{E_iE_j}(z)$, $A(z)$ and $B(z)$ are polynomials with real coefficients such that $B(z) \neq 0$ on the unit circle. Then, $\mathcal{E}$ is a set of rationally related random processes.

The set $\mathcal{F}$ is defined as the set of transfer matrices $\mathcal{H}$ comprised of real-rational single-input single-output (SISO) transfer functions that are analytic on the unit circle $\{z \in \mathbb{C} |\ |z| = 1\}$. The set $\mathcal{FE}$ is defined as

$$\mathcal{FE} := \left\{ x = \sum_{k=1}^{m} \mathcal{H}_k(z)\mathsf{E}_k(z) \mid E_k \in \mathcal{E}, \mathcal{H}_k(z) \in \mathcal{F} \right\}.$$

For a finite number of elements $\mathsf{X}_1(z), ..., \mathsf{X}_m(z) \in \mathcal{FE}$, tf-span is defined as

$$\textit{tf-span}\{\mathsf{X}_1(z), ..., \mathsf{X}_m(z)\} := \left\{ x = \sum_{i=1}^{m} \boldsymbol{A}_i(z)\mathsf{X}_i(z) \mid \boldsymbol{A}_i(z) \in \mathcal{F} \right\}.$$

**Lemma 8.9.1.** *The $tf-span$ operator defines a subspace of $\mathcal{FE}$.*

*Proof.* The proof is left to the reader. □

**Definition 33** (Inner Product)**.** *Given two vector stationary processes, $X_1(k)$ and $X_2(k)$, we define the inner product as $\langle X_1, X_2 \rangle := \mathbb{E}[X_1' X_2] = \mathbb{E}[tr[X_1X_2']] = tr[\mathbb{E}[X_1X_2']] = tr[R_{X_1X_2}(0)] = tr[\int_{-\pi}^{\pi} \Phi_{X_1X_2}(e^{\iota\omega})]$, where $tr$ is the trace operator.*

Now we present a lemma which lists down the conditions for unique representation of any element in *tf-span*$\{\mathsf{X}_i(z)\}_{i=1,...,m}$.

**Lemma 8.9.2.** *Let $q(k)$ and $X_1(k), ..., X_m(k)$ be vector stationary processes such that $\mathsf{q}(z), \mathsf{X}_1(z), ..., \mathsf{X}_m(z)$ are in the space $\mathcal{FE}$. Define $X(k) = [X_1'(k) \; ... \; X_m'(k)]'$. Suppose that $\mathsf{q}(z) \in$ tf-span$\{\mathsf{X}_i(z)\}_{i=1,...,m}$ and that $\Phi_X(e^{\iota\omega}) \succ 0$ almost for any $\omega \in \; [-\pi, \pi]$. Then there exists a unique transfer matrix $\Lambda(z) \in \mathcal{F}^{T \times mT}$ such that $q = \Lambda(z)X$.*

*Proof.* Suppose $\mathsf{q}(z) = \Lambda_1(z)\mathsf{X}(z) = \Lambda_2(z)\mathsf{X}(z)$, with $\Lambda_1(z) \neq \Lambda_2(z)$. Then, $r = [\Lambda_2(e^{\iota\omega}) - \Lambda_1(e^{\iota\omega})]\mathsf{X}(e^{\iota\omega}) = \mathbf{0}$. Thus, $\Phi_r = \mathbf{0}$, implying,

$$[\Lambda_2(e^{\iota\omega}) - \Lambda_1(e^{\iota\omega})]\Phi_X(e^{\iota\omega})[\Lambda_2(e^{\iota\omega}) - \Lambda_1(e^{\iota\omega})]^* = \mathbf{0}.$$

Since $\Phi_X(e^{\iota\omega}) \succ 0$ for any $\omega \in [-\pi, \pi]$, it follows that $\Lambda_2(e^{\iota\omega}) - \Lambda_1(e^{\iota\omega}) = \mathbf{0}$ almost everywhere. Thus, $\Lambda_2(z) - \Lambda_1(z)$ equals the zero matrix, implying that $\Lambda_1(z) = \Lambda_2(z)$. □

Now we present the non causal Wiener Filter for vector stationary processes.

**Theorem 8.9.1** (Wiener Filter)**.** *Let $\mathsf{V}(z)$ and $\mathsf{X}_1(z), ..., \mathsf{X}_m(z)$ be the $z$ transform of the $T \times 1$ vector stationary processes $V(k)$ and $X_1(k), ..., X_m(k)$ respectively. Define $\mathcal{X} := tf\!-\!span[\mathsf{X}_1(z), ...., \mathsf{X}_m(z)], X(k) := [X_1'(k) \; ... \; X_m'(k)]'$ and $\mathsf{X}(z)$ be the $z$ transform of $X(k)$. Consider the problem of determining the closest approximation $\hat{\mathsf{V}}(z)$ of $\mathsf{V}(z)$ with elements from the space $\mathcal{X}$, that is,*

$$\inf_{\mathsf{q}(z) \in \mathcal{X}} \|\mathsf{V}(z) - \mathsf{q}(z)\|_2^2. \tag{8.13}$$

*If $\Phi_X(z) \succ 0$, for $\omega \in [-\pi, \pi]$, then the solution $\hat{V} \in \mathcal{X}$ exists, is unique and is given by*

$$\hat{\mathsf{V}}(z) = \boldsymbol{W}(z)\mathsf{X}(\mathsf{z}), \boldsymbol{W}(z) = \Phi_{VX}(z)\Phi_X(z)^{-1}.$$

*Moreover, $\hat{\mathsf{V}}(z)$ is the only element in $\mathcal{X}$ such that, for any $\mathsf{q}(z) \in \mathcal{X}$,*

$$\langle \mathsf{V}(z) - \hat{\mathsf{V}}(z), q(z) \rangle = 0. \tag{8.14}$$

*Proof.* Since $\mathsf{q}(z) \in \mathcal{X}$, $\mathsf{q}(z)$ can be written as $\boldsymbol{W}(z)\mathsf{X}(z)$ and the cost function is written as

$$\begin{aligned}
&\|\mathsf{V}(e^{\iota\omega}) - \boldsymbol{W}(e^{\iota\omega})\mathsf{X}(e^{\iota\omega})\|^2 \\
&= tr[\int_{-\pi}^{\pi} \Phi_V(e^{\iota\omega}) - \Phi_{VX}(e^{\iota\omega})\boldsymbol{W}^*(e^{\iota\omega}) \\
&- \boldsymbol{W}(e^{\iota\omega})\Phi_{XV}(e^{\iota\omega}) + \boldsymbol{W}(e^{\iota\omega})\Phi_X(e^{\iota\omega})\boldsymbol{W}^*(e^{\iota\omega})d\omega] \\
&= \int_{-\pi}^{\pi} tr[\Phi_V(e^{\iota\omega}) - \Phi_{VX}(e^{\iota\omega})\boldsymbol{W}^*(e^{\iota\omega}) \\
&- \boldsymbol{W}(e^{\iota\omega})\Phi_{XV}(e^{\iota\omega}) + \boldsymbol{W}(e^{\iota\omega})\Phi_X(e^{\iota\omega})\boldsymbol{W}^*(e^{\iota\omega})d\omega]
\end{aligned}$$

Minimizing the integrand for all $\omega \in [-\pi, \pi]$ with respect to $\boldsymbol{W}(e^{\iota\omega})$ by differentiating the integrand with respect to $\boldsymbol{W}(e^{\iota\omega})$ and setting it equal to $\mathbf{0}$ leads to,

$$2\boldsymbol{W}(e^{\iota\omega})\Phi_X(e^{\iota\omega}) - \Phi_{VX}(e^{\iota\omega}) - \Phi_{XV}^*(e^{\iota\omega}) = \mathbf{0}.$$

Since, $\Phi_X(e^{\iota\omega}) \succ 0$ and $\Phi_{VX}(e^{\iota\omega}) = \Phi_{XV}^*(e^{\iota\omega})$, it follows that

$$\boldsymbol{W}(e^{\iota\omega}) = \Phi_{VX}(e^{\iota\omega})\Phi_X(e^{\iota\omega})^{-1}. \tag{8.15}$$

The filter $\boldsymbol{W}(z) := \Phi_{VX}(z)\Phi_X(z)^{-1}$ is the non causal Wiener filter for estimation of $V$ from $X$ that has the specified frequency response given by (8.15). Thus $\hat{V} = \boldsymbol{W}(z)X \in \mathcal{X}$ minimizes the cost (8.13). If $\Phi_X(z) \succ 0$, the uniqueness of $\boldsymbol{W}(z)$ follows from Lemma 8.9.2. The Hilbert Space projection theorem (for pre-Hilbert spaces) then guarantees the orthogonality of the error $V - \hat{V}$ with the space $\mathcal{X}$.

□

# Chapter 9

# Conclusion

In the first part of this dissertation, fundamental limits on energetics of erasing a bit of information is discussed. We used time multiplexing of a laser in an optical tweezer setup to demonstrate bit erasure close to the Landauer's limit. Experimental characterization of optical traps is used to develop a Monte Carlo simulation framework, which is in agreement with the experimental observations and is a computational engine to study thermodynamic aspects of bit level computations. Next, a mixture of Gaussian distribution approach was adopted to analyze information erasures rigorously. We concluded that success proportion, size of the memory bit and asymmetry could lower the minimum energy consumption for bit erasures below the Landauer's bound. Furthermore, a trade-off between reliability of bit erasures and energy consumption is indicated due to reducing the size of the memory bit.

In the second part, the focus was on inference of structure of a network representation of a complex system from time series measurements of the system. An algorithm using a synergy of Wiener filtering and graphical separation for linear bi-directed dynamical systems with radial topology is discussed, with applications to power distribution networks. Next, we looked at linear dynamical systems with loops in the network structure. An algorithm based on magnitude and phase response of multivariate Wiener filter is presented, which is guaranteed to infer the exact network structure. The efficacy of the method is demonstrated on power networks, building thermal dynamics and wireless network of clients. A highlighting feature of the algorithms is that only time series measurements from the system are needed and no knowledge of any system parameter or exogenous inputs is required. Moreover, these algorithms function even in the presence of colored exogenous inputs unlike white noise inputs in prior work. The discussion so far assumes all nodes in the network to be observable. For radial bi-directed linear dynamical systems if unobserved nodes are four or more hops away, the network structure can be inferred exactly along with the location of the unobserved nodes using the algorithm presented. Furthermore, the notion of Wiener filtering to infer the moral graph of the underlying network of wide sense stationary time series is extended to a class of non stationary processes, namely cyclostationary processes. This extension enables all the algorithms presented in Chapters 5, 6 and 7 to be applicable even in the case of cyclostationary processes.

# Chapter 10

# Future Work

The simulation and experimental framework could be further expanded to study other basic computations like OR and NOT. Moreover, the framework could also be used to design mechanisms to achieve computations using measurement and feedback. Such developments could shed light on thermodynamic consequences of measurement and feedback control. One of the recent developments is in designing optimal erasure mechanisms and establishing connections with the theory of optimal mass transport [146]. The analytical framework for analysis of information erasure using a Gaussian mixture approach is based entirely on exponentially decaying tails of Gaussian distributions. The framework could be generalized to a much more general class of probability measures like a mixture of log concave distributions. Moreover, the entropy inequalities have connections with channel capacity in information theory as discussed in [147].

The network structure learning algorithms discussed need to be expanded to account for system nonlinearities. Kernel based techniques could possibly be used to improve the performance of these methods in the nonlinear regime. Analysis of the regularization aspect needs to be performed and appropriate guidelines for the choice of regularization parameter needs to be established. Application of the structure learning algorithms for network monitoring, fault detection and others could be explored as well. A promising extension is also in learning network parameters, for example, resistances in a RC network or line impedance in a power network once the network structure is inferred. Structure learning with parameter estimation will significantly broaden the scope of the directions pursued in this dissertation and expand the scope of network system identification.

# Bibliography

[1] Jonathan Koomey, Stephen Berard, Marla Sanchez, and Henry Wong. Implications of historical trends in the electrical efficiency of computing. *IEEE Annals of the History of Computing*, 33(3):46–54, 2011.

[2] D. Deka, S. Backhaus, and M. Chertkov. Estimating distribution grid topologies: A graphical learning based approach. In *Power Systems Computation Conference (PSCC)*, 2016.

[3] Donatello Materassi and Murti V Salapaka. On the problem of reconstructing an unknown topology via locality properties of the wiener filter. *IEEE Transactions on Automatic Control*, 57(7):1765–1777, 2012.

[4] T Athay, R Podmore, and S Virmani. A practical method for the direct analysis of transient stability. *IEEE Transactions on Power Apparatus and Systems*, (2):573–584, 1979.

[5] Xi Fang, Satyajayant Misra, Guoliang Xue, and Dejun Yang. Smart gridâĂŤthe new and improved power grid: A survey. *IEEE communications surveys & tutorials*, 14(4):944–980, 2012.

[6] Chad Goerzen, Zhaodan Kong, and Bernard Mettler. A survey of motion planning algorithms from the perspective of autonomous uav guidance. *Journal of Intelligent and Robotic Systems*, 57(1-4):65, 2010.

[7] Deborah Snoonian. Smart buildings. *IEEE spectrum*, 40(8):18–23, 2003.

[8] Subhas Chandra Mukhopadhyay, Krishanthi P Jayasundera, and Anton Fuchs. *Advancement in sensing technology: New developments and practical applications*, volume 1. Springer Science & Business Media, 2012.

[9] Alan Gatherer. Ten communications technology trends for 2018.

[10] Patrick Moorhead. Datacenter storage matters more than ever in 2018. *Forbes website: https://www.forbes.com/sites/patrickmoorhead/2018/01/28/datacenter-storage-matters-more-than-ever-in-2018/#3daba62e468e.*

[11] Ibrahim Abaker Targio Hashem, Ibrar Yaqoob, Nor Badrul Anuar, Salimah Mokhtar, Abdullah Gani, and Samee Ullah Khan. The rise of âĂIJbig dataâĂİ on cloud computing: Review and open research issues. *Information systems*, 47:98–115, 2015.

[12] Pedro Garcia Lopez, Alberto Montresor, Dick Epema, Anwitaman Datta, Teruo Higashino, Adriana Iamnitchi, Marinho Barcellos, Pascal Felber, and Etienne Riviere. Edge-centric computing: Vision and challenges. *ACM SIGCOMM Computer Communication Review*, 45(5):37–42, 2015.

[13] Somayya Madakam, R Ramaswamy, and Siddharth Tripathi. Internet of things (iot): A literature review. *Journal of Computer and Communications*, 3(05):164, 2015.

[14] Pervez Hameed Shaikh, Nursyarizal Bin Mohd Nor, Perumal Nallagownden, Irraivan Elamvazuthi, and Taib Ibrahim. A review on optimized control systems for building energy and comfort management of smart sustainable buildings. *Renewable and Sustainable Energy Reviews*, 34:409–429, 2014.

[15] DeepMind. Deepmind ai reduces google data centre cooling bill by 40%. *DeepMind website https://deepmind.com/blog/deepmind-ai-reduces-google-data-centre-cooling-bill-40/.*

[16] Joao Marques Lima. Data centres of the world will consume 1/5 of earthâĂŹs power by 2025. *Data Economy website: https://data-economy.com/data-centres-world-will-consume-1-5-earths-power-2025/.*

[17] Hassan Farhangi. The path of the smart grid. *IEEE power and energy magazine*, 8(1), 2010.

[18] Sue Sharples, Vic Callaghan, and Graham Clarke. A multi-agent architecture for intelligent building sensing and control. *Sensor Review*, 19(2):135–140, 1999.

[19] Ed Bullmore and Olaf Sporns. Complex brain networks: graph theoretical analysis of structural and functional systems. *Nature Reviews Neuroscience*, 10(3):186, 2009.

[20] Jonathan F Donges, Yong Zou, Norbert Marwan, and Jürgen Kurths. Complex networks in climate dynamics. *The European Physical Journal Special Topics*, 174(1):157–179, 2009.

[21] S. Boccaletti, V. Latora, Y. Moreno, M. Chavez, and D. U. Hwang. Complex networks: Structure and dynamics. *Physics Reports*, 424(4-5):175–308, February 2006.

[22] G Moore. Cramming more components onto integrated circuits', electronics, vol. 38, no. 8, 1965.

[23] Gordon E Moore et al. Progress in digital integrated electronics. In *Electron Devices Meeting*, volume 21, pages 11–13, 1975.

[24] Richard P Feynman. *The pleasure of finding things out: The best short works of Richard P. Feynman.* Helix Books, 2005.

[25] John von Neumann and Arthur W Burks. *Theory of self-reproducing automata.* University of Illinois Press, 1966.

[26] Charles H Bennett. The thermodynamics of computation : A review. *International Journal of Theoretical Physics*, 21(12):905–940, 1982.

[27] Rolf Landauer. Irreversibility and heat generation in the computing process. *IBM Journal of Research and Development*, 5(3):183–191, 1961.

[28] Deepjyoti Deka, Michael Chertkov, and Scott Backhaus. Structure learning in power distribution networks. *IEEE Transactions on Control of Network Systems*, 2017.

[29] John Scott. *Social network analysis.* Sage, 2017.

[30] Franklin Allen and Ana Babus. Networks in finance. *The network challenge: strategy, profit, and risk in an interlinked world*, 367, 2009.

[31] Ian F Akyildiz, Weilian Su, Yogesh Sankarasubramaniam, and Erdal Cayirci. Wireless sensor networks: a survey. *Computer networks*, 38(4):393–422, 2002.

[32] Marzieh Nabi-Abdolyousefi. Network identification via node knockout. In *Controllability, Identification, and Randomness in Distributed Systems*, pages 17–29. Springer, 2014.

[33] Donatello Materassi and Murti V Salapaka. Identification of network components in presence of unobserved nodes. In *Decision and Control (CDC), 2015 IEEE 54th Annual Conference on*, pages 1563–1568. IEEE, 2015.

[34] J. Pearl. *Probabilistic reasoning in intelligent systems: networks of plausible inference.* Morgan Kaufmann, 1988.

[35] Judea Pearl. *Causality.* Cambridge university press, 2009.

[36] Nicolai Meinshausen, Peter Bühlmann, et al. High-dimensional graphs and variable selection with the lasso. *The annals of statistics*, 34(3):1436–1462, 2006.

[37] Jerome Friedman, Trevor Hastie, and Robert Tibshirani. Sparse inverse covariance estimation with the graphical lasso. *Biostatistics*, 9(3):432–441, 2008.

[38] Rainer Dahlhaus. Graphical interaction models for multivariate time series1. *Metrika*, 51(2):157–172, 2000.

[39] Jorge Gonçalves and Sean Warnick. Necessary and sufficient conditions for dynamical structure reconstruction of lti networks. *IEEE Transactions on Automatic Control*, 53(7):1670–1674, 2008.

[40] Reynaldo F Nuqui and Arun G Phadke. Phasor measurement unit placement techniques for complete and incomplete observability. *IEEE Transactions on Power Delivery*, 20(4):2381–2388, 2005.

[41] Avi Caspi, Rony Granek, and Michael Elbaum. Enhanced diffusion in active intracellular transport. *Physical Review Letters*, 85(26):5655, 2000.

[42] Orla M Wilson, Xiaoyuan Hu, David G Cahill, and Paul V Braun. Colloidal metal particles as probes of nanoscale thermal transport in fluids. *Physical Review B*, 66(22):224301, 2002.

[43] Koen Visscher and Steven M Block. Versatile optical traps with feedback control. *Methods in Enzymology*, 298:460–489, 1998.

[44] Keir C Neuman and Attila Nagy. Single-molecule force spectroscopy: optical tweezers, magnetic tweezers and atomic force microscopy. *Nature methods*, 5(6):491, 2008.

[45] Arthur Ashkin, JM Dziedzic, JE Bjorkholm, and Steven Chu. Observation of a single-beam gradient force optical trap for dielectric particles. *Optics letters*, 11(5):288–290, 1986.

[46] Subhrajit Roychowdhury, Shreyas Bhaban, Srinivasa Salapaka, and Murti Salapaka. Design of a constant force clamp and estimation of molecular motor motion using modern control approach. In *American Control Conference (ACC), 2013*, pages 1525–1530. IEEE, 2013.

[47] Subhrajit Roychowdhury, Tanuj Aggarwal, Srinivasa Salapaka, and Murti V Salapaka. High bandwidth optical force clamp for investigation of molecular motor motion. *Applied Physics Letters*, 103(15):153703, 2013.

[48] Crispin W Gardiner et al. *Handbook of stochastic methods*, volume 4. Springer Berlin, 1985.

[49] Ken Sekimoto. *Stochastic energetics*, volume 799. Springer, 2010.

[50] Frederick Reif. *Fundamentals of statistical and thermal physics*. Waveland Press, 2009.

[51] ML Huber, RA Perkins, A Laesecke, DG Friend, JV Sengers, MJ Assael, IN Metaxa, E Vogel, R Mareš, and K Miyagawa. New international formulation for the viscosity of $h_2o$. *Journal of Physical and Chemical Reference Data*, 38(2):101–125, 2009.

[52] Don S Lemons and Paul Langevin. *An introduction to stochastic processes in physics*. JHU Press, 2002.

[53] Lowell I McCann, Mark Dykman, and Brage Golding. Thermally activated transitions in a bistable three-dimensional optical trap. *Nature*, 402(6763):785–787, 1999.

[54] Juan MR Parrondo, Jordan M Horowitz, and Takahiro Sagawa. Thermodynamics of information. *Nature Physics*, 11(2):131–139, 2015.

[55] Kousuke Shizume. Heat generation required by information erasure. *Physical Review E*, 52(4):3495, 1995.

[56] Raoul Dillenschneider and Eric Lutz. Memory erasure in small systems. *Physical Review Letters*, 102(21):210601, 2009.

[57] Brian Lambson, David Carlton, and Jeffrey Bokor. Exploring the thermodynamic limits of computation in integrated systems: Magnetic memory, nanomagnetic logic, and the landauer limit. *Physical Review Letters*, 107(1):010604, 2011.

[58] Barbara Piechocinska. Information erasure. *Physical Review A*, 61(6):062314, 2000.

[59] Takahiro Sagawa and Masahito Ueda. Minimal energy cost for thermodynamic information processing: measurement and information erasure. *Physical Review Letters*, 102(25):250602, 2009.

[60] Antoine Bérut, Artak Arakelyan, Artyom Petrosyan, Sergio Ciliberto, Raoul Dillenschneider, and Eric Lutz. Experimental verification of landauer's principle linking information and thermodynamics. *Nature*, 483(7388):187–189, 2012.

[61] Yonggun Jun, Momčilo Gavrilov, and John Bechhoefer. High-precision test of landauer's principle in a feedback trap. *Physical review letters*, 113(19):190601, 2014.

[62] Momčilo Gavrilov and John Bechhoefer. Erasure without work in an asymmetric double-well potential. *Physical Review Letters*, 117(20):200601, 2016.

[63] Jeongmin Hong, Brian Lambson, Scott Dhuey, and Jeffrey Bokor. Experimental test of landauer's principle in single-bit operations on nanomagnetic memory bits. *Science Advances*, 2(3):e1501492, 2016.

[64] Ken Sekimoto. Kinetic characterization of heat bath and the energetics of thermal ratchet models. *Journal of the Physical Society of Japan*, 66(5):1234–1237, 1997.

[65] Ken Sekimoto and Shinichi Sasa. Complementarity relation for irreversible process derived from stochastic energetics. *Journal of the Physical Society of Japan*, 66(11):3326–3328, 1997.

[66] Ken Sekimoto. Langevin equation and thermodynamics. *Progress of Theoretical Physics Supplement*, 130:17–27, 1998.

[67] Keir C Neuman and Steven M Block. Optical trapping. *Review of scientific instruments*, 75(9):2787–2809, 2004.

[68] Shreyas Bhaban, Saurav Talukdar, and Murti Salapaka. Noise induced transport at microscale enabled by optical fields. In *2016 American Control Conference (ACC)*, pages 5823–5829. IEEE, 2016.

[69] Tanuj Aggarwal and Murti Salapaka. Real-time nonlinear correction of back-focal-plane detection in optical tweezers. *Review of Scientific Instruments*, 81(12):123105, 2010.

[70] HS Lef and AF Rex. Maxwell demon 2: Entropy, classical and quantum information. *Computing (Institute of Physics Publishing, Bristol and Philadelphia, 2003)*, 2003.

[71] Saurav Talukdar, Shreyas Bhaban, and Murti V Salapaka. Memory erasure using time-multiplexed potentials. *Physical Review E*, 95(6):062121, 2017.

[72] I Neri, M Lopez-Suarez, D Chiuchiú, and L Gammaitoni. Reset and switch protocols at landauer limit in a graphene buckled ribbon. *EPL (Europhysics Letters)*, 111(1):10004, 2015.

[73] Miquel Lopez-Suarez, Igor Neri, and Luca Gammaitoni. Sub-kbt microelectromechanical irreversible logic gate. *Nature communications*, 7, 2016.

[74] Luca Gammaitoni. Beating the landauer's limit by trading energy with uncertainty. *arXiv preprint arXiv:1111.2937*, 2011.

[75] OJE Maroney. Generalizing landauer's principle. *Physical Review E*, 79(3):031105, 2009.

[76] D Chiuchiú, MC Diamantini, and L Gammaitoni. Conditional entropy and landauer principle. *EPL (Europhysics Letters)*, 111(4):40004, 2015.

[77] JMR Parrondo and B Jiménez de Cisneros. Energetics of brownian motors: a review. *Applied Physics A*, 75(2):179–191, 2002.

[78] J. Melbourne, S. Talukdar, S. Bhaban, and M. V. Salapaka. Error bounds on a mixed entropy inequality. In *Proc. IEEE Intl. Symp. Inform. Theory*, Vail, Colorado, June 2018.

[79] Armin Alaghi and John P Hayes. Survey of stochastic computing. *ACM Transactions on Embedded computing systems (TECS)*, 12(2s):92, 2013.

[80] Giacomo Indiveri, Bernabé Linares-Barranco, Robert Legenstein, George Deligeorgis, and Themistoklis Prodromakis. Integration of nanoscale memristor synapses in neuromorphic computing architectures. *Nanotechnology*, 24(38):384010, 2013.

[81] Antoine Bérut, Artyom Petrosyan, and Sergio Ciliberto. Information and thermodynamics: experimental verification of landauer's erasure principle. *Journal of Statistical Mechanics: Theory and Experiment*, 2015(6):P06015, 2015.

[82] Hajo Holzmann and Sebastian Vollmer. A likelihood ratio test for bimodality in two-component mixtures with application to regional income distribution in the eu. *AStA Advances in Statistical Analysis*, 92(1):57–69, 2008.

[83] Lalit Gupta and Thotsapon Sortrakul. A gaussian-mixture-based image segmentation algorithm. *Pattern Recognition*, 31(3):315–325, 1998.

[84] Saurav Talukdar, Shreyas Bhaban, and Murti Salapaka. Beating landauerâĂŹs bound by memory erasure using time multiplexed potentials. *IFAC-PapersOnLine*, 50(1):7645–7650, 2017.

[85] Thomas M Cover and Joy A Thomas. *Elements of information theory*. John Wiley & Sons, 2012.

[86] Crispin Gardiner. *Stochastic methods*, volume 4. springer Berlin, 2009.

[87] Karin Knorr Cetina and Alex Preda. *The sociology of financial markets*. Oxford University Press, 2004.

[88] Jean-François Rual, Kavitha Venkatesan, Tong Hao, Tomoko Hirozane-Kishikawa, Amélie Dricot, Ning Li, Gabriel F Berriz, Francis D Gibbons, Matija Dreze, Nono Ayivi-Guedehoussou, et al. Towards a proteome-scale map of the human protein–protein interaction network. *Nature*, 437(7062):1173–1178, 2005.

[89] Prabha Kundur, Neal J Balu, and Mark G Lauby. *Power system stability and control*, volume 7. McGraw-hill New York, 1994.

[90] Francesco Bullo, Jorge Cortes, and Sonia Martinez. *Distributed control of robotic networks: a mathematical approach to motion coordination algorithms*. Princeton University Press, 2009.

[91] Patrik DâĂŹhaeseleer, Shoudan Liang, and Roland Somogyi. Genetic network inference: from co-expression clustering to reverse engineering. *Bioinformatics*, 16(8):707–726, 2000.

[92] Jianshu Chen and Ali H Sayed. Diffusion adaptation strategies for distributed optimization and learning over networks. *IEEE Transactions on Signal Processing*, 60(8):4289–4305, 2012.

[93] Judea Pearl. *Probabilistic reasoning in intelligent systems: networks of plausible inference*. Morgan Kaufmann, 2014.

[94] Michael Irwin Jordan. *Learning in graphical models*, volume 89. Springer Science & Business Media, 1998.

[95] Steffen L Lauritzen. *Graphical models*, volume 17. Clarendon Press, 1996.

[96] Venkat Chandrasekaran, Pablo A. Parrilo, and Alan S. Willsky. Latent variable graphical model selection via convex optimization. *Ann. Statist.*, 40(4):1935–1967, 08 2012.

[97] Saurav Talukdar, Mangal Prakash, Donatello Materassi, and Murti V Salapaka. Reconstruction of networks of cyclostationary processes. In *IEEE 54th Annual Conference on Decision and Control (CDC), 2015*, pages 783–788. IEEE, 2015.

[98] Jalal Etesami and Negar Kiyavash. Directed information graphs: A generalization of linear dynamical graphs. In *2014 American Control Conference*, pages 2563–2568. IEEE, 2014.

[99] Roy Hoffman. Practical state estimation for electric distribution networks. In *IEEE PES Power Systems Conference and Exposition*, pages 510–517. IEEE, 2006.

[100] Deepjyoti Deka, Scott Backhaus, and Michael Chertkov. Structure learning and statistical estimation in distribution networks - part i. *arXiv preprint arXiv:1501.04131*, 2015.

[101] AG Phadke. Synchronized phasor measurements in power systems. *IEEE Computer Applications in Power*, 6(2):10–15, 1993.

[102] A von Meier, David Culler, Andrew McEachern, and R Arghandeh. Micro-synchrophasors for distribution systems. pages 1–5, 2014.

[103] Saverio Bolognani, Nicoletta Bof, Davide Michelotti, Riccardo Muraro, and Luca Schenato. Identification of power distribution network topology via voltage correlation analysis. In *IEEE Decision and Control (CDC)*, pages 1659–1664. IEEE, 2013.

[104] D. Deka, S. Backhaus, and M. Chertkov. Learning topology of the power distribution grid with and without missing data. In *European Control Conference (ECC)*, 2016.

[105] D. Deka, S. Backhaus, and M. Chertkov. Learning topology of distribution grids using only terminal node measurements. In *IEEE Smartgridcomm*, 2016.

[106] Raffi Sevlian and Ram Rajagopal. Feeder topology identification. *arXiv preprint arXiv:1503.07224*, 2015.

[107] R. Diestel. *Graph Theory.* Springer-Verlag, Berlin, Germany, 2006.

[108] Jan TA Koster. On the validity of the markov interpretation of path diagrams of gaussian structural equations systems with correlated errors. *Scandinavian Journal of Statistics*, 26(3):413–431, 1999.

[109] Enrique Castillo, Jose M Gutierrez, and Ali S Hadi. *Expert systems and probabilistic network models.* Springer Science & Business Media, 2012.

[110] Judea Pearl and Rina Dechter. Identifying independencies in causal graphs with feedback. In *Proceedings of the Twelfth international conference on Uncertainty in artificial intelligence*, pages 420–426. Morgan Kaufmann Publishers Inc., 1996.

[111] Ali Abur and Antonio Gomez Exposito. *Power system state estimation: theory and implementation.* CRC press, 2004.

[112] Anantha Pai. *Energy function analysis for power system stability.* Springer Science & Business Media, 2012.

[113] Christopher J Quinn, Negar Kiyavash, and Todd P Coleman. Directed information graphs. *IEEE Transactions on information theory*, 61(12):6887–6909, 2015.

[114] Shahin Shahrampour and Victor M Preciado. Topology identification of directed dynamical networks via power spectral analysis. *IEEE Transactions on Automatic Control*, 60(8):2260–2265, 2015.

[115] Alain Y Kibangou and Christian Commault. Decentralized laplacian eigenvalues estimation and collaborative network topology identification. *IFAC Proceedings Volumes*, 45(26):7–12, 2012.

[116] Fabio Morbidi and Alain Y Kibangou. A distributed solution to the network reconstruction problem. *Systems & Control Letters*, 70:85–91, 2014.

[117] Saurav Talukdar, Deepjyoti Deka, Donatello Materassi, and Murti V Salapaka. Exact topology reconstruction of radial dynamical systems with applications to distribution system of the power grid. *American Control Conference*, 2017.

[118] Sunetra Chowdhury and Peter Crossley. *Microgrids and active distribution networks*. The Institution of Engineering and Technology, 2009.

[119] Glenn Reynders, Jan Diriken, and Dirk Saelens. Quality of grey-box models and identified parameters as function of the accuracy of input and observation signals. *Energy and Buildings*, 82:263–274, 2014.

[120] Saurav Talukdar, Deepjyoti Deka, Blake Lundstrom, Michael Chertkov, and Murti V Salapaka. Learning exact topology of a loopy power grid from ambient dynamics. In *Proceedings of the Eighth International Conference on Future Energy Systems*, pages 222–227. ACM, 2017.

[121] Donatello Materassi and Murti V Salapaka. Reconstruction of directed acyclic networks of dynamical systems. In *American Control Conference (ACC), 2013*, pages 4687–4692. IEEE, 2013.

[122] José Pereira, Morteza Ibrahimi, and Andrea Montanari. Learning networks of stochastic differential equations. In *Advances in Neural Information Processing Systems*, pages 172–180, 2010.

[123] Francis R Bach. Consistency of the group lasso and multiple kernel learning. *Journal of Machine Learning Research*, 9(Jun):1179–1225, 2008.

[124] Harish Doddi, Saurav Talukdar, Deepjyoti Deka, and Murti Salapaka. Data-driven identification of a thermal network in multi-zone building (under review). In *IEEE 57st Annual Conference on Decision and Control (CDC)*. IEEE, 2018.

[125] Saurav Talukdar, Deepjyoti Deka, Sandeep Attree, Donatello Materassi, and Murti V Salapaka. Learning the exact topology of undirected consensus networks. *arXiv preprint arXiv:1710.00032*, 2017.

[126] John A Gubner. *Probability and random processes for electrical and computer engineers*. Cambridge University Press, 2006.

[127] M. Siami, S. Bolouki, B. Bamieh, and N. Motee. Centrality measures in linear consensus networks with structured network uncertainties. *IEEE Transactions on Control of Network Systems*, pages 1–1, 2017.

[128] Deepjyoti Deka, Saurav Talukdar, Michael Chertkov, and Murti V Salapaka. Topology estimation in bulk power grids: Guarantees on exact recovery. In *Bulk Power Systems Dynamics and Control Symposium (X) IREP Symposium*, 2017.

[129] Yiteng Huang, Jacob Benesty, and Jingdong Chen. *Acoustic MIMO signal processing*. Springer Science & Business Media, 2006.

[130] Eben Upton and Gareth Halfacree. *Raspberry Pi user guide*. John Wiley & Sons, 2014.

[131] Mangal Prakash, Saurav Talukdar, Sandeep Attree, Vikas Yadav, and Murti Salapaka. Max-min algorithm for distributed finite time termination of consensus in presence of delays. *arXiv preprint arXiv:1701.00021*, 2016.

[132] Peter G Ellis, Paul A Torcellini, and Drury B Crawley. Energy design plugin: An energyplus plugin for sketchup; preprint. Technical report, National Renewable Energy Lab.(NREL), Golden, CO (United States), 2008.

[133] Drury B Crawley, Curtis O Pedersen, Linda K Lawrie, and Frederick C Winkelmann. Energyplus: energy simulation program. *ASHRAE journal*, 42(4):49, 2000.

[134] Jerome Friedman, Trevor Hastie, and Robert Tibshirani. *The elements of statistical learning*, volume 1. Springer series in statistics New York, 2001.

[135] US DoE. Energyplus engineering reference. *The reference to energyplus calculations*, 2010.

[136] Harm HM Weerts, Arne G Dankers, and Paul MJ Van den Hof. Identifiability in dynamic network identification. *IFAC-PapersOnLine*, 48(28):1409–1414, 2015.

[137] Firoozeh Sepehr and Donatello Materassi. Inferring the structure of polytree networks of dynamic systems with hidden nodes. In *Decision and Control (CDC), 2016 IEEE 55th Conference on*, pages 4618–4623. IEEE, 2016.

[138] Mattia Zorzi and Rodolphe Sepulchre. Ar identification of latent-variable graphical models. *IEEE Transactions on Automatic Control*, 61(9):2327–2340, 2016.

[139] Roger A Horn and Charles R Johnson. *Matrix analysis.* Cambridge university press, 2012.

[140] Antonio Napolitano. *Generalizations of cyclostationary signal processing: spectral analysis and applications*, volume 95. John Wiley & Sons, 2012.

[141] Fakher Chaari, Jacek Leskow, Antonio Napolitano, and Andrea Sanchez-Ramirez. *Cyclostationarity: Theory and Methods.* Springer, 2014.

[142] William A Gardner. An introduction to cyclostationary signals. *Cyclostationarity in communications and signal processing*, pages 1–90, 1994.

[143] Ryan F Schkoda, Robert B Lund, and John R Wagner. Clustering of cyclostationary signals with applications to climate station sitings, eliminations, and merges.

[144] Harry L Hurd and Abolghassem Miamee. *Periodically correlated random sequences: spectral theory and practice*, volume 355. John Wiley & Sons, 2007.

[145] Donatello Materassi and Murti V Salapaka. On the problem of reconstructing an unknown topology via locality properties of the wiener filter. *Automatic Control, IEEE Transactions on*, 57(7):1765–1777, 2012.

[146] James Melbourne, Saurav Talukdar, and Murti Salapaka. Realizing information erasure in finite time. *arXiv preprint arXiv:1809.09216*, 2018.

[147] James Melbourne, Saurav Talukdar, Shreyas Bhaban, and Murti V Salapaka. The deficit in an entropic inequality. *arXiv preprint arXiv:1805.11257*, 2018.